Alma Mater Studiorum · University of Bologna

School of Science

Department of Physics and Astronomy (DIFA)

Master Degree in Physics

# Tissue-equivalent organic semiconductors for sustainable radiation detectors

**Supervisor:**

Laura Basiricò

**Submitted by:**

Diego Matteini

**Co-supervisor:**

Giulia Napolitano

Academic Year 2024/2025

# *Abstract*

The interest in wearable radiation detection devices for medical, aerospace and industrial purposes has reached an all-time peak: the choice of flexible substrates and tissue equivalent materials, such as organic compounds, shows great potential for such applications, but the fabrication of the devices is undermined by the use of toxic solvents in the production process, which makes it less environmental–friendly and harder to handle for producers. In this thesis the performances of X-ray detectors, fabricated using anisole as a greener solvent alterative for the organic semiconductive layer, are investigated. In parallel, a step towards the full tissue equivalence of the samples was taken by using the organic conductive polymer PEDOT: PSS for the electrodes' fabrication. Together, these studies proved the possible realization of working, wearable X-ray detectors, using green, tissue equivalent materials. This transition did not compromise the detector's response capabilities (with device sensitivities up to $S = (41 \pm 3) \cdot 10^3\ \mu C \cdot Gy \cdot cm^{-2}$) and without showing signs of heavy performance degradation over long periods of time. Overall, this research opens new possibilities for future developments of organic dosimeters that are fully tissue equivalent, while also shedding some light on how state-of-the-art performances can be achieved without the need for the currently in use toxic materials.

# *Contents*

# *Introduction*

The detection of ionizing radiation is fundamental for several different fields, with applications in medicine[1–4], industry[5], research, environmental studies[6] and aerospace[7]. Historically, the most widely used detectors relied on inorganic semiconductors as active component and the research in this field has achieved impressive results[8]. These devices, however, are not exempt from having limitations, and for some applications the emerging field of organic electronics represents a promising step forward. Indeed, the implementation of organic small molecules or polymers as active material grants unique features to this kind of detectors: they are chosen for their mechanical stability[3,9], making them capable of working on flexible substrates, their tissue-equivalent nature[2], rendering them ideal for medical purposes as wearable dosimeters, and their low environmental toxicity. The deposition processes for organic detectors are also an advantage point when compared to inorganic ones, with the former comprising solution-based techniques[10] with lower costs, lower temperature requirements and easier large-area device production. For all these reasons, together with the promising increase in X-ray sensitivities values recorded over the past years[10], organic detectors have reached an all-time peak of interest. The research, nevertheless, still has some limitations to address, such as the fabrication of these devices requiring the use of toxic solvents when dealing with the organic semiconductor deposition[11], and the widespread use of metallic electrodes which hinders the full tissue equivalence of the devices[12]. To face these issues, novel solutions are being explored: the scope of this work is to study the use of both green solvents and tissue-equivalent materials in the development of X-ray detectors, by evaluating their response variation when compared to the devices realized with gold electrodes and toluene-based processing.

The first chapter spans over the theory of X-ray sources and detection devices: after a general introduction, chapter 1.3. contains an in-depth look at semiconductor detectors and the role that photoconductive gain[12] plays in their performance. The chapter closes with a detailed picture of X-

ray detectors, spanning over the main types developed so far, their specific characteristics and their main figures of merit.

Chapter 2 tackles directly the core issue of the study: sections 2.1 and 2.3. address the aforementioned challenges of green production and tissue-equivalent characteristics respectively, giving insight into the scope of the issue addressed in this thesis. In chapter 2.2 the topic of green solvents used for the deposition of the active semiconductive component of the devices is studied, with particular interest on the latest advances[11] in green solutions for organic detectors. The complementary issue of tissue-equivalence is discussed in section 2.4. instead, where the organic conductive polymer PEDOT:PSS[13] is analysed as a possible alternative to gold as the device's electrodes material.

The third chapter opens with an overview of the main materials of interest used during the study, with particular emphasis on the green solvent anisole and the tissue-equivalent polymer PEDOT:PSS. Sections 3.2. and 3.3. outline the whole detector fabrication process: the former contains a detailed description of both the photolithography and the evaporation process for the fabrication of gold electrodes, and for the fabrication of the PEDOT:PSS electrodes, achieved though spin coating technique. The latter chapter focuses on the comparison of anisole and toluene based solutions and describes the deposition process of the semiconductor layer. Chapter 3.4 describes methods for the characterization of the devices through morphological and electrical studies, as well as their response to X-ray and UV radiation. The last section goes over how the data acquired was analysed and the main tools used to extract the results discussed in the following chapter.

Chapter 4 opens with an overview of the various batches of devices under study, their architecture and key characteristics. This is followed by a description of the results obtained from their morphological (4.1.1.) and electrical (4.1.2 and 4.1.3.) studies. Section 4.2. looks at the comparison between the results obtained from the X-ray analysis performed on samples fabricated using either

toluene or anisole as solvent. Similarly, section 4.3. focuses on a similar comparison drawn between devices with either gold or PEDOT:PSS electrode fingers, fabricated with a toluene based solution. Subchapter 4.3.3. presents an additional comparative study of the UV responsivity of analogous samples, this time produced using anisole as a solvent for the active component.

The conclusion of the thesis goes over the main results obtained, summarising them and giving insight into possible future developments.

# *Chapter 1:*
# *Radiation Detection*

Ionizing radiation refers to the part of the electromagnetic spectrum which has enough energy to ionize atoms and molecules (γ-rays, X-rays, and extreme-UV photons, although a clear threshold is difficult to define because different elements have different ionization energies); out of these, X-rays, defined as the electromagnetic waves whose wavelengths are between 0.1Å and 10 Å, are of significant interest because they are employed in different fields. In research, X-rays are widely used as powerful probes to investigate the material properties, for instance through diffraction, scattering, and spectroscopic techniques. In medicine, they are fundamental for key applications such as diagnostic imaging and therapy treatments. Moreover, X-rays are present in space environments, where they contribute to the radiation background experienced by spacecraft and instrumentation. For these reasons, the accurate detection and monitoring of X-ray radiation is essential across scientific, medical, aerospace, and industrial contexts[1,4,5,7].

### 1.1. X-ray Sources

X-rays are naturally produced by the decay process involving heavy radioactive elements, where nuclear transitions may emit high-energy photons. Although radioactive sources are characterized by well-defined half-lives, the radiation produced from such processes has evident limitation when considered for most applications: the X-ray beam can be hardly controlled, and the intensity usually requires finer tuning. To address such issues, working with engineered X-ray sources, such as X-ray tubes or synchrotron radiation facilities, is generally preferred. The former represents the most used source of X-ray radiation for routine and less demanding applications thanks to their compact size and affordability, while still providing adequate radiation quality for many uses. Fig. 1 below contains a schematic representation of the internal composition of an X-ray tube.

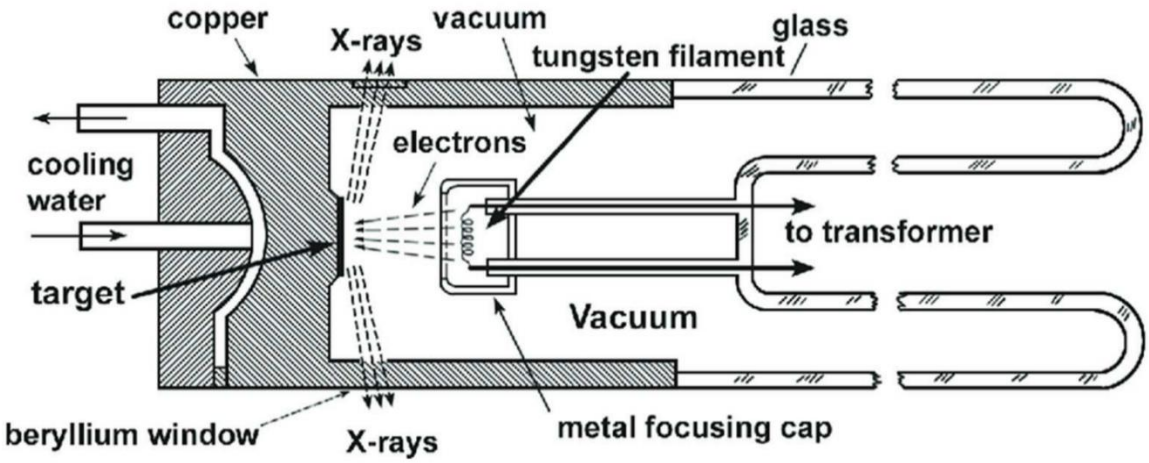


Fig. 1: Schematic representation of an X-ray tube internal structure.

As can be seen, a filament is heated through Joule effect, prompting an emission of thermionic generated electrons. Once ejected, a strong potential bias Vd (in the order of kV) accelerates them towards a target made of a high-Z material (such as Molybdenum or Tungsten). This process generates characteristic X-ray lines based on the material being hit: the incoming high energy electrons can eject core ones from the inner atomic shells, leaving a hole in their place. Subsequently, electrons occupying the upper shell levels undergo a cascade relaxation process,

ultimately falling into the position of the ejected one, by emitting X-ray photons at fixed energies. At the same time a parallel process takes place, when the Coulomb interaction with the target nuclei causes a deceleration of the electrons, leading to a subsequent loss of energy by emission of radiation. This process generates a continuous spectrum (called Bremsstrahlung radiation) whose maximum energy depends on the magnitude of the voltage Vd, with higher energetic values corresponding to higher accelerating potentials. Nevertheless, most of the energy generated by the deceleration of the electrons is not converted into ionizing radiation, but becomes kinetic energy and heats up the material; a cooling system (such as the water-cooling one depicted in Fig. 1) is thus necessary to operate the device over a longer period, avoiding overheating. In Fig. 2 the radiation output from a Tungsten-target X-ray tube is displayed, where both effects are clearly visible as described above.

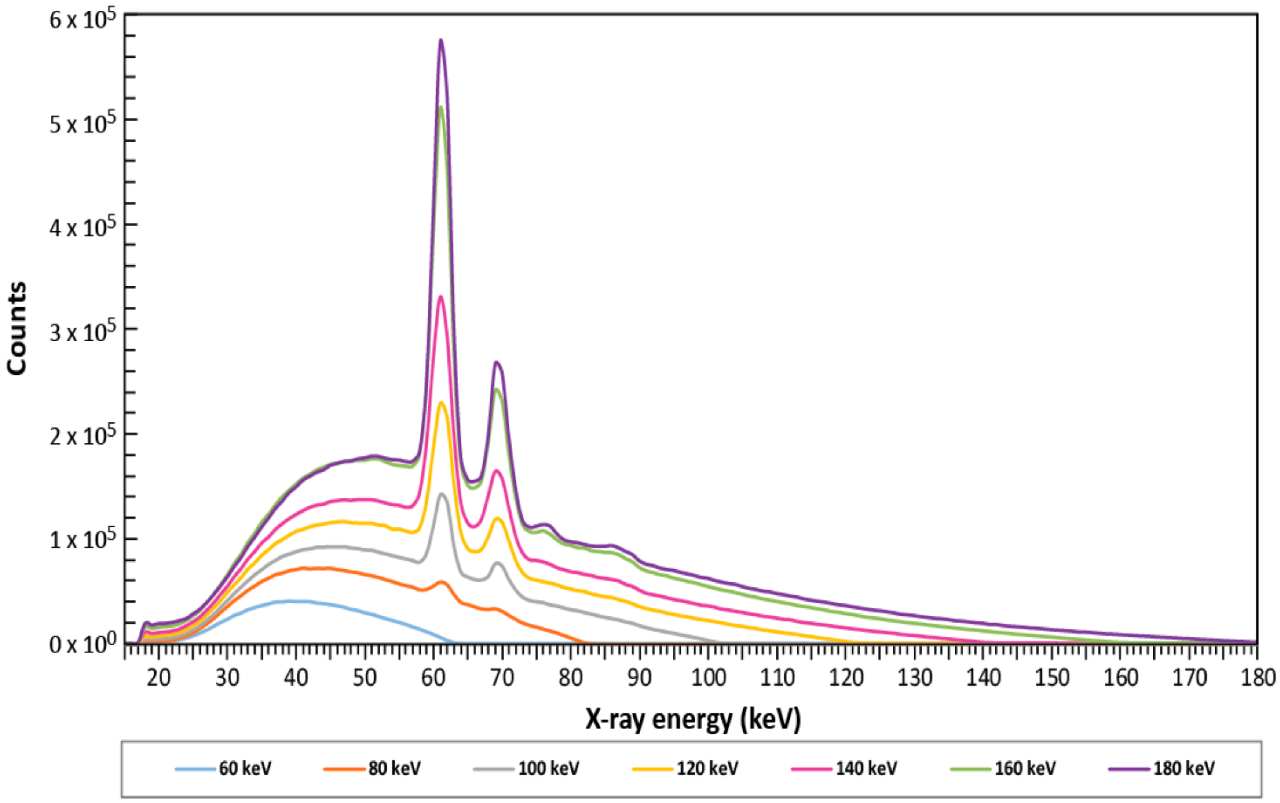


Fig. 2: Example of output radiation from a Tungsten X-ray tube, where both the absorption peaks (with wavelengths of 60 nm and 70 nm) and the bremsstrahlung radiation are clearly visible. Different lines represent different accelerating voltages as indexed below the curves.

In conclusion X-ray tubes are the perfect tool for most common uses thanks to their low-cost, easy availability and simple functioning, with some limitations when it comes to the quality of the radiation generated due to the spectral characteristic lines being fixed at certain wavelengths and the presence of the wideband bremsstrahlung effect. To work with higher intensities of radiation, a large particle accelerator called “synchrotron” is needed. In this, a system of magnets (from simple bending magnets to wigglers and undulators) is used to accelerate charged particles (usually electrons) to relativistic speeds radially, along the cyclic path, prompting emissions at specific energies depending on the particle’s speed and the magnitude of the magnetic field (Fig. 3). Compared to X-ray tube, this method of radiation production is obviously much more demanding both in terms of cost and technical requirements; nevertheless, the radiation produced is finely tuned, with the possibility of shifting the peak intensity in between a wide range of energies (up to high X-ray) and concentrating it into a narrow beam with exceptionally high brightness (defined as the number of generated photons passing across unit area over unit time).

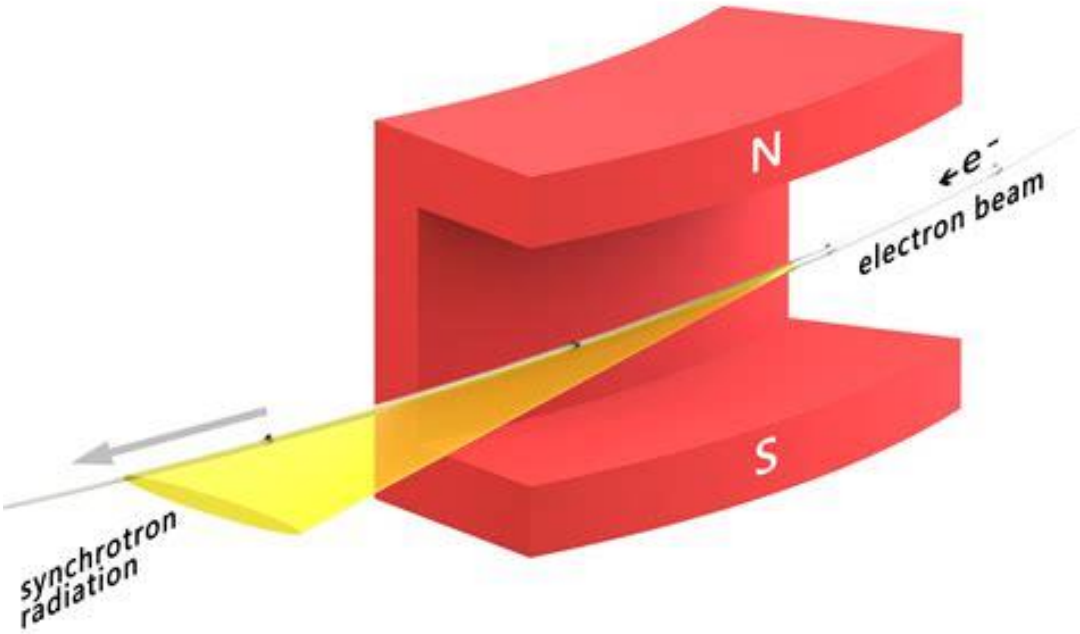


Fig. 3: Graphical representation of synchrotron radiation generation.

### 1.2. Radiation detectors

A radiation detector is a device collecting photons and converting them into an electric signal. The structure and functioning of a radiation detector highly depend on the type of interaction the radiation itself has with the detector.

#### 1.2.1. Principles of X-ray detection

X-ray devices can operate in two distinct modes: the first one, called “pulse mode”, detects every single interaction, although a certain dead time must elapse between one count and the next, making counting of each instance reliable, but also limiting its use when multiple interaction events happen during the intermission time. Alternatively, the “current” operation mode is a better choice for continuous detection: individual interactions are not distinguished but get averaged, generating an electrical signal proportional to the radiation energy.

The detection mechanism, as mentioned above, depends ultimately on the interaction between radiation and detecting material. With regards to X-rays three main categories, defined by the medium in which absorption occurs, are widely used: gas-based detectors (ionization chambers, proportional and GM counters) that collect charge from electron-ion pairs generated in the gas, indirect scintillating detectors, which use a scintillator to convert the radiation into visible light, then detected through a photodetector, and direct semiconductors detectors[14]. We’ll focus on these last ones for the rest of the thesis. The working principle of semiconductor detectors is based on the ability of such materials to generate electron-hole pairs when irradiated: when an incident X-ray photon is absorbed in the semiconductor, it interacts predominantly via the photoelectric effect and, at higher energies, Compton scattering[15], producing energetic secondary electrons. These carriers lose their energy through repeated ionization events, creating multiple electron–hole pairs. Under an applied electric field, the generated charges are then drifted toward the electrodes and collected as a measurable current.

Historically inorganic semiconductors have been the most employed materials for X-ray due to their high degree of crystal order and the easily controlled impurities and defects concentrations inside of them, which result in exceptional transport capabilities. High stopping power and fast response time are also ideal characteristics of these materials. Silicon and germanium have been and still are considered as excellent semiconductors for radiation and particle detection due to their high availability and versatility. When it comes to X-ray detectors, however, their performances have been surpassed by more recent compounds, such as Cadmium Zinc Telluride (CZT)[16], which has set a new benchmark for detector performances.

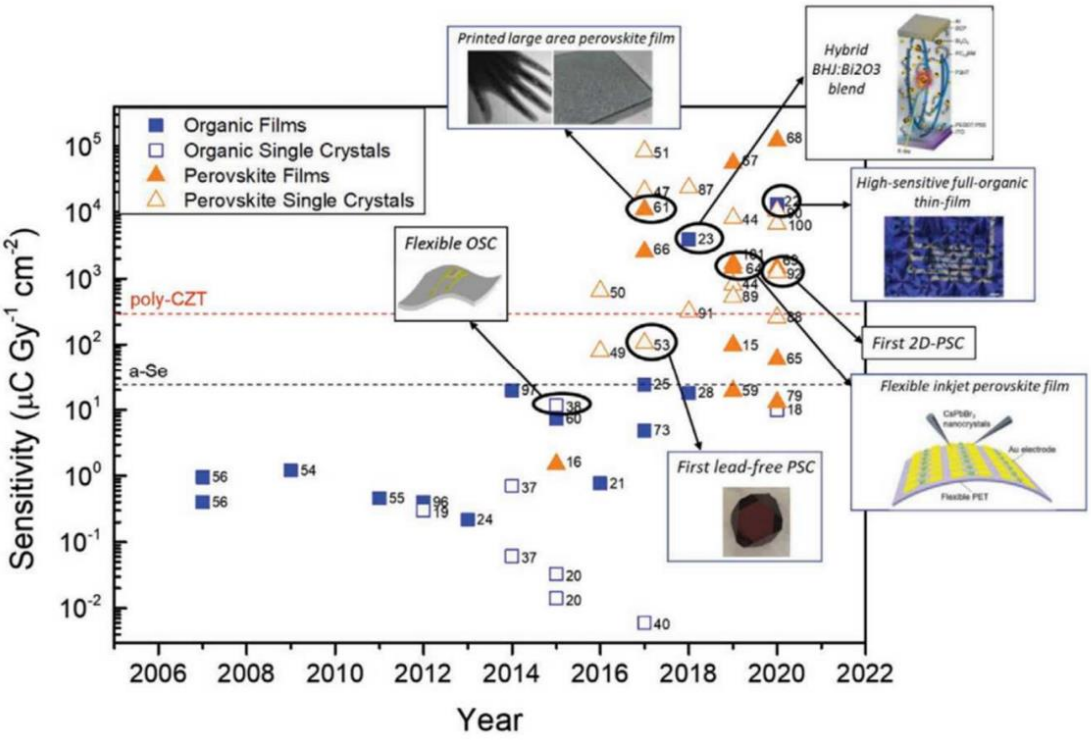


Fig. 4: Evolution of detector sensitivity over the years. As seen in the legend, thin films and single crystals of organic and perovskite active materials are indicated through different symbols.

Despite these achievements, inorganic devices have intrinsic limitations, such as lack of flexibility, processing constraints, high toxicity and low tissue equivalence. A possible alternative capable of solving such problems is represented by organic semiconductor devices. Fig. 4 displays a graph detailing the increase in device sensitivities over the years. As can be seen, in just a few years

organic detectors have tremendously improved in sensitivity, with state-of-the-art organic devices rivalling with their inorganic counterpart.

### 1.3. Organic semiconductors devices for radiation detection

Organic electronics research field has seen a tremendous increase in interest over the past decades, with applications ranging from organic LEDs[17] to flexible photovoltaics[9] and sensors[18]. As mentioned above, the development of organic semiconductors for X-ray detectors is particularly promising due to the many applications they might have in the industrial and medical fields. In fact, contrary to inorganic materials, organic semiconductor devices can count on low costs and easy fabrication over large areas. This is because they are easily deposited through solution-based techniques (spin-coating, blade coating, printing, drop casting and more), even at low temperatures[19]. The operational cost is also advantageous, due to the low bias they require to be operated[20].

From a structural point of view, organic semiconductors consist of π-conjugated molecules or polymer chains that assemble in the solid state through relatively weak intermolecular interactions - primarily van der Waals forces and π–π stacking (and, in some cases, hydrogen bonding). Being composed of mostly hydrogen and carbon atoms, these materials have low atomic numbers Z, which also affect the detector's properties, limiting the absorption of high energy photons. Although this might lower the performance of the device, at the same time it improves significantly the tissue equivalence of the detector, as the resulting attenuation is closer to that of biological tissue. This characteristic will be expanded upon in chapter 2.

### 1.3.1. State-of-the-art organic semiconductor detectors

The organic semiconductors for ionizing radiation detectors are classified into two main types based on their structure: single crystals and polycrystalline thin films.

Single crystals display long range crystalline order and lack of grain boundaries, resulting in high electrical mobility (in the order of 10 $cm^2/Vs$) and effective charge collection at the electrodes. Another characteristic of single crystals is their low dark current, which is crucial for precision measurements by reducing noise and improving the signal-to-noise ratio, especially at low signal levels[21]. As detailed by Ciavatti et al.[22], the best detection capabilities have been obtained at high voltages using thick crystals, thus hindering the flexibility of the devices. However, in recent years, the development of higher sensitivity, low-voltage bendable detectors using organic single crystals has opened new possibilities for X-ray detectors production (micrometre-sized flexible single crystals are being investigated, but they are still underperforming when compared to thin-film devices)[22].

In contrast, polycrystalline thin films are particularly attractive for their mechanical bendability, which make them well suited to flexible substrates. They also exhibit excellent compatibility with solution-based deposition techniques, such as inkjet printing and bar coating, ideal for the fabrication of low-cost large area detectors. As cited above, a possible strategy to achieve better thin film detector performances is doping the organic semiconductor with high-Z nanoparticles[23,24]. However, these additional nanoparticles, requiring a high atomic number, are usually composed of inorganic elements not suitable for nontoxic, tissue equivalent devices. To overcome the limitations of these approaches, the photoconductive gain effect, based on the photocurrent amplification during X-ray irradiation caused by charge trapping, has been widely investigated. The next section outlines the physical mechanism underlying photoconductive gain.

### 1.3.2. Photoconductive gain

The photoconductive gain effect consists of an internal amplification of the photocurrent generated in response to the absorption of high energy photons by a semiconductor material with active trap states. In fact, the theoretical charge collection current $I_{CC}$ generated by the absorption of the high energy photons is usually an underestimation of the value measured experimentally (it can be two orders of magnitude smaller[20]). The theoretical current can be expressed through:

$$I_{CC} = \Phi nq, \qquad (1)$$

where $\Phi$ is the photon absorption rate, n the number of electron-hole pairs generated per absorbed photon and q the elementary charge. The actual value $I_{PG}$ can be written as the product of $I_{CC}$, measuring the semiconductor's ability to absorb radiation and collect the generated charges, and G, a dimensionless gain factor taking account of the photocurrent amplification. This phenomenon is theorized to be causing the peculiar saw-tooth shape, observed for the photocurrent response under an on/off switching X-ray beam in organic semiconductor detectors (An example of such behaviour is shown in Fig. 5a), as detailed in the kinetic model proposed in 2016 by Basiricò et al.[20].

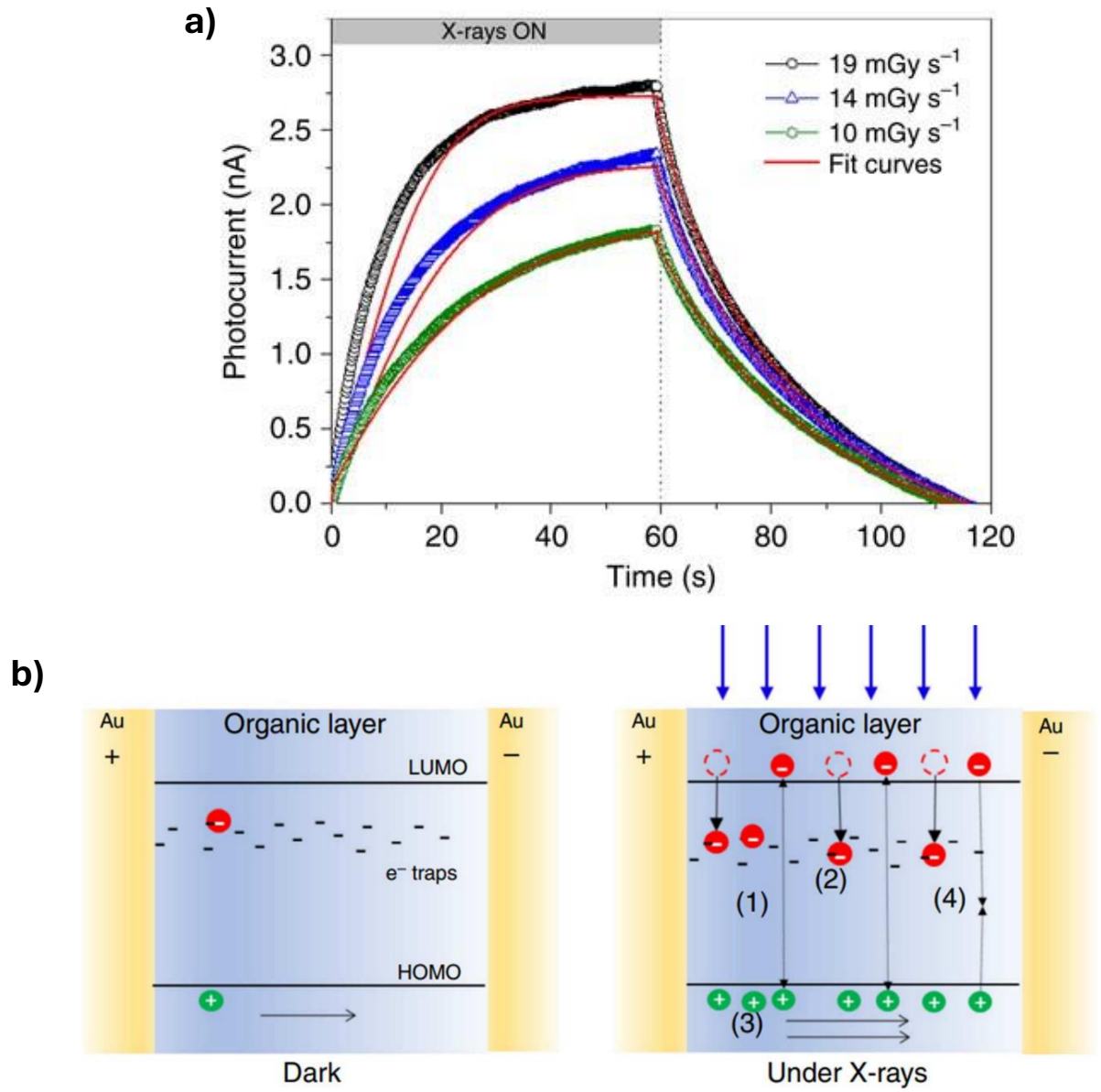


Fig. 5: **a)** Photocurrent on/off curves (60 seconds interval) at different dose rates: as can be seen the typical saw tooth response is clearly obtained; moreover, a lower dose rate, and thus a lower absorption rate, corresponds to a decrease in photocurrent. The red lines represent the calculated fit curves of the theoretical model. **b)** Organic semiconductor detection mechanism: when irradiated, to the so called "dark current" (always present and given by the intrinsic carriers), an additional photocurrent given by the collection of the photogenerated electron-hole pairs must be added.

In organic semiconductors the majority carriers (usually holes) and the minority carriers (usually electrons) exhibit different transport behaviour: while the former tends to have higher mobility, the

latter tend to be trapped more easily (electron traps, for example, occur when employing a polar substrate such as PET[25] in the device architecture or when oxygen is present[26]). Deep minority carriers trap states can prevent charge recombination by trapping the photogenerated minority carriers for a trapping time $\tau_r$. To maintain the charge neutrality equilibrium, electron trapping is counterbalanced by hole injection at the opposite electrode. This leads to the generation of more than a single free charge carrier for every electron-hole pair created by high energy photons, thus amplifying the current response.

A schematic representation of this process is shown above in Fig 5b.

When working under uniform field approximation, by defining the transit time $\tau_t$ as the time needed for the majority carriers to cross the detector's active layer

$$\tau_t = \frac{L^2}{\mu V} \tag{2}$$

with L the layer's length, V the external bias and μ the majority carrier's mobility, then the gain factor G can be expressed as the ratio of the characteristic times

$$G = \frac{\tau_r}{\tau_t}. \tag{3}$$

Moreover, the minority carriers lifetime $\tau_r$ is dependent on the photogenerated carrier concentration $\rho_x$ and can be approximated through the phenomenological equation (4):

$$\tau_r(\rho_x) = \frac{\alpha}{\gamma} \left[\alpha \ln\left(\frac{\rho_0}{\rho_x}\right)\right]^{\frac{1-\gamma}{\gamma}} \tag{4}$$

where $\alpha$, $\gamma$ and $\rho_0$ are constants depending on the semiconductor material, used to describe the characteristic time scale, the dispersion of trap states and a reference carrier density respectively. By looking at eq. 4 it can be observed how the theorized stretched exponential behaviour matches the experimental photocurrent curve.

Due to the fundamental role played by the photoconductive gain in increasing the photocurrent response of the detector, it is of high importance to carefully tune the presence of traps inside the material.

### 1.3.3. Trap sites and photocurrent behaviour

Building upon the previous chapter, this section takes a closer look at the mechanisms responsible for the formation of deep trap states within the bandgap of organic semiconductors. As described in the literature[27,28], the primary origin of trap states is structural disorder. Most intrinsic trap states can be associated with structural defects and chemical impurities, which are introduced during or after crystal or film formation and can be mitigated through careful control of the growth process. Trap states may also have an external origin and can be intentionally or unintentionally introduced through exposure to moisture, electromagnetic radiation, temperature gradients, or bias stress, as well as through the presence of dopants or through interfacing with other materials, such as metals, dielectrics, or other organic semiconductors. While often detrimental to charge transport, trap states can also be exploited to improve device performance by careful tuning to increment the photoconductive gain; for instance, as reported by Fratelli et al.[12], by varying the semiconductor solution deposition parameters (the technique used was pneumatic nozzle printing, particularly adapt to be finely tuned), it was possible to modify the morphology and crystallization of the thin film. Through this, both the minority carriers lifetime and transit time were tuned to achieve optimal sensitivity values. Similar conclusions were reached when working with bar-assisted meniscus shearing (BAMS) as deposition technique[29]: by tuning this process to reduce grain size while increasing the amount of grain boundaries, the density of minority charge carrier traps was increased. This led to slower recombination times and a subsequent increase in the photoconductive gain effect. At the same time, trap-induced photoconductive gain has been reported in organic phototransistors based on single-component donor–acceptor conjugated polymer nanowires, leading

to an enhanced near-infrared photoresponse[30] (in this particular case the traps were postulated to be the product of a high surface to volume ratio, causing an increase in trap sites from absorbed water and oxygen molecules).

Because of this, the current state-of-the-art suggests that controlling trap states is key to optimizing the performance and sensitivity of organic semiconductor X-ray detectors.

## 1.4. Radiation detector characterization

In this section the main parameters used to analyse and characterize the performances of the organic semiconductor detectors presented in this thesis will be discussed.

### 1.4.1. Figures of merit

#### Sheet resistance

Sheet resistance $R_s$ is introduced to describe the in-plane electrical resistance of a thin conductive layer. This quantity, used when working with devices where one dimension (in this case, the thickness) is negligible, represents the electrical resistance of the device independent of its lateral dimensions, thus enabling comparison between detectors of different sizes. For an interdigitated architecture, it is defined as lateral resistance per square area of film and is calculated as:

$$R_s = \frac{R\, N_{chan}\, W}{L} \tag{4}$$

where R is the resistance and $N_{chan}$, L and W are respectively the device's number of channels, channel length and width. Its unit of measure is ohms per square (Ω/sq).

**Dark current**

The dark current $I_{dark}$ corresponds to the current measured by the device when no ionizing radiation is impinging on the detector's active component. Since its fluctuations are a source of noise, dark current must be kept as low as possible to ensure a higher signal-to-noise ratio. Dark current is mainly the result of three aspects: thermal generated carriers inside the semiconductor, carriers' injection through the electrodes and the presence of defective states. Thus, lower dark currents can be achieved by lowering the amount of defects (high-purity single crystals or treated polycrystalline thin-films are favoured) while also working with higher band-gap materials (due to decreased thermal carriers' generation).

**Responsivity**

The responsivity R is defined as the ratio of the photocurrent $I_{phot.}$ of a photodetector to the optical power intensity P incident to the device

$$R = \frac{I_{phot.}}{P \cdot A_d} \tag{7}$$

where $A_d$ is the active area of the photodetector. $I_{phot.}$ is calculated as the difference between the detector's output when illuminated and its dark current[32]. The physical interpretation of resistivity is similar to that of sensitivity, as a quantity measuring the detector's conversion efficiency into current, but differs in its normalization to optical power density rather than dose rate.

**Sensitivity**

The sensitivity is the quantity defined as the charge Q collected by the detector per unit of radiation exposure X and unit area A. A practical interpretation would be to consider the sensitivity as the normalized efficiency of the detector in converting a certain amount of radiation into current. As

detailed by Mescher et al.[31], assuming monoenergetic X-rays, the sensitivity of a detector could be expressed as:

$$S = S_0 \, \nu_x \, \nu_m \, \nu_{cc} \tag{6}$$

where $S_0$, $\nu_x$, $\nu_m$ and $\nu_{cc}$ are respectively a normalization constant depending on the X-ray energy, the X-ray absorption efficiency, the material efficiency at converting radiation into electron-hole pairs, and the charge collection efficiency. It follows that a large number of factors influences the sensitivity of the detector; notably, the absorption efficiency $\nu_x$ highly depends on both the thickness of the active layer and its elements atomic number (as mentioned in previous chapters), while the charge collection efficiency may vary based on the architecture of the device, the applied bias and the mobility of the semiconductor. To improve the sensitivity to the fullest the device must be structured and fabricated keeping in mind all these contributions. If the detector is operating in current mode, the sensitivity is usually derived as the slope of linear fit of the photocurrent over dose rate plot. However, a more detailed discussion of how sensitivity was extracted from the experimental data in this work, will be presented in chapter 3, together with its physical interpretation.

**Radiation hardness**

The prolonged interaction with ionizing radiation can damage the semiconductive material by generating defects, in some cases permanently hindering the response capabilities of the interested device. The decreased response can be caused by an unwanted variation in the applied electric field due to carriers trapped in defects states, thus lowering the charge collection at the electrodes. The presence of trapped charges capable of recombining with photogenerated ones before collection can also affect the device, lowering the photoconductive response. Radiation hardness is defined as the ability of a material to resist such damage following irradiation.

## 1.5. Elements of radiation dosimetry

Radiation dosimetry is the branch of science that measures the amount of energy deposited by radiation in matter and biological tissues. The fundamental dosimetric quantities are introduced and discussed in this section.

### Absorbed dose

A quantity corresponding to the mean energy deposited by ionizing radiation per unit of mass, expressed in gray (Gy), corresponding to Joule per kilogram ($J \cdot kg^{-1}$). To be more precise, given a point P in the material, we can write the absorbed dose at point P as:

$$D_{abs}(P) = \frac{d\varepsilon}{dm} \tag{8}$$

where dε and dm represent respectively the expected amount of energy deposited in an infinitesimal volume dV at point P and the mass of dV[33]. In many applications it is also convenient to use another quantity, the dose rate, defined as the absorbed dose delivered per unit time and expressed in Gray per second.

### Equivalent dose

Each type of radiation, when interacting with different kinds of organic tissue, displays unique behaviours. To fully consider the various interactions, a new quantity, called Equivalent dose ($H_{T,R}$) in the tissue T for the radiation R, is introduced; this quantity can be expressed as the product of the absorbed dose averaged over the tissue or organ with a tabulated weighting factor $W_R$ based on the radiation type

$$H_{T,R} = D_{abs} \cdot W_R \tag{9}$$

If the absorbed dose is expressed in Gy, the equivalent dose is expressed in Sieverts (Sv).

Tissue equivalence is a parameter used to evaluate how closely a material interacts with radiation when compared to human tissue. Thus, tissue-equivalent dosimeters provide a response highly representative of the corresponding dose absorbed by organic tissues. Currently employed, state-of-the-art devices such as passive $Al_2O_3$:C[34] and active, semiconductor-based SiC[35] and diamond[36] dosimeters can achieve high detection accuracy but require heavy compensation to approximate tissue response; in particular, when dealing with non-tissue-equivalent devices, multi-element filters are necessary to compensate for energy-dependent under or over response, while algorithmic reconstructions of the absorbed dose based on expected energy spectra introduce uncertainty in the results.

To solve this issue, tissue-equivalent detectors are being investigated: Zeidel et al.[2] proposed a passive, high sensitivity radiation dosimeter based on OTFT architecture, capable of detecting the radiation dose as a shift in the device's threshold voltage. Passive detectors are also being investigated for medical applications, with Fratelli et al.[37] reporting an organic tissue equivalent dosimeter formed by an OPT coupled to a polysiloxane-based scintillator, also tested in clinical conditions. An organic, tissue equivalent thin-film device was also proposed by Basiricò et al.[3], based on a photoconductor architecture; this device displayed reliable performances when tested as dosimeter in a clinical environment, but its tissue equivalence was lowered by the presence of gold electrodes in the design. The research interest for high-sensitivity tissue equivalent dosimeters has reached an all-time high: this work expands on this demand, by introducing a fully tissue equivalent detectors based on organic thin film as active layer and PEDOT:PSS as electrodes.

# *Chapter 2:*
# *Sustainable processes for tissue equivalent devices*

Despite the development of highly efficient and flexible organic X-ray detectors, some challenges still need be addressed: this chapter tackles the problems of green production and tissue equivalence, focusing on state-of-the-art achievements and novel solutions to be developed.

On one hand the need for a sustainable development of devices, hindered by the use of toxic components during fabrication, will be analysed and green alternatives to the materials currently in use will be discussed.

Similarly, the importance and current limitations of tissue equivalent devices will be presented. In our class of devices, where gold electrodes represent the main challenge for tissue equivalence, novel possibilities are opened through the use of the organic conducting polymer PEDOT:PSS, described in detail in the following. Because of this, a direct comparison between the two materials will be drawn.

## 2.1. Motivations for sustainable manufacturing

The advancements in organic X-ray detector performances have sparked unprecedented interest for this class of devices due to their unique characteristics. Unfortunately, little has been done to address the use of hazardous halogenated and aromatic hydrocarbon solvents in their production[38]. Currently halogen and aromatic toxic solvents (some examples would be chloroform, chlorobenzene, toluene) are the most widely used due to their high versatility, optimal physical properties and impressive ability in dissolving a wide range of molecular and polymeric structures. At the same time their toxicity hinders mass production due to environmental and health concerns. Moreover, due to the global shift of both companies and governments towards green manufacturing, with ever increasing limitations of harmful chemicals in production chains, the push for sustainable alternatives is at an all-time high. Despite this, little research has been done in the field of green alternatives for organic semiconductors processing, with few notable studies published on the use of green solvents for the production of organic photovoltaics[39] and polymeric semiconductors[40]. To tackle this problem, green, non-toxic materials are currently being investigated; some of these alternatives will be discussed in the following section.

## 2.2. Green solvents for semiconductor deposition

The choice of solvent can impact deeply device performance, affecting the crystallization process and molecular aggregation of the organic semiconductor during deposition; this, in turn, influences charge transport properties[41]. The search for suitable solvents has some conditions to follow. First, they must be capable of solubilizing the semiconductor to the right concentration (with optimal values exceeding 1 mg $mL^{-1}$), with high wettability permitting the formation of uniform thin films of the desired thickness and size. Then, they should have appropriate viscosity and boiling point values, with some solvents unsuitable for use due to safety concerns or processing limitations related to their low boiling point. Lastly, and most notably, the solvent must facilitate good crystallization, with high film texture and long, continuous crystals to facilitate charge transport.

As reported by Ho et al.[42] several green solvents have shown promising result: this study, focusing on the realization of green organic photovoltaics and organic thin film transistors, has cross compared multiple results to assess the quality of each solvent studied. Five green solvents, namely iso-butyl acetate, iso-propyl acetate, dimethyl carbonate, anisole and t-amyl methyl ether, have shown promising results, with optimal values for their boiling point and viscosity, as well as electrical performances (hole mobility was analysed with respect to the same deposited semiconductors, 6,13-bis-(tri-isopropylsilyl-ethynyl)pentacene, also referred to as TIPS-PEN). Most notably, green processed devices showed better transport properties than their toxic counterparts, with the highest hole mobility for a green solvent at $\mu_h$ = 2.6 $cm^2 V^{-1} s^{-1}$ (isobutyl acetate) (anisole was a close second, with a mobility of $\mu_h$ = 1.9 $cm^2 V^{-1} s^{-1}$) compared to the highest mobility for a toxic solvent at $\mu_h$ = 1.5 $cm^2 V^{-1} s^{-1}$ (Chlorobenzene). A full review of the solvents analysed in the study of Campana et al. is reported in Fig. 6.

| Classification | Solvent | Overall Green Assess. | B.p. (°C) | Viscosity | TIPS-PEN FFa | TIPS-PEN $\mu_h$ | Default Rank | Ranking after discussion |
|---|---|---|---|---|---|---|---|---|
| Alcohol | Solketal | | 188-189 | | | | | |
| | HEPyr | | 140-142[b] | | | | | |
| | 1,3-propanediol | | 214 | | | | | |
| Ester | 2-ethylhexylacetate | | 199-200 | | | | | |
| | Diethyl succinate | | 216-218 | | | | | |
| | Dimethyl adipate | | 109-110 | | | | | |
| | Dimethyl succinate | | 200 | | | | | |
| | Esterol F | | > 300 | | | | | |
| | Ethyl-4-oxopentanoate | | 220 | | | | | |
| | Ethylene glycolediacetate | | 186-187 | | | | | |
| | Ethyl-L-lactate | | 154 | | | | | |
| | γ-valerolactone | | 207-208 | | | | | |
| | i-butylacetate | | 116-117 | | | | | |
| | i-propylacetate | | 88.8 | | | | | |
| | IRIS | | 215.6 | | | | | |
| | Isoamyl acetate | | 142 | | | | | |
| | Loxanol | | > 300 | | | | | |
| | Methyl formate | | 31-33 | | | | | |
| | Methyl laurate | | 261-262 | | | | | |
| | Methyl oleate | | > 300 | | | | | |
| | Methyl tetradecanoate | | 323 | | | | | |
| | n-amyl acetate | | 149 | | | | | |
| | Pentyl-oxopentanoate | n.a.[c] | > 300 | | | | | |
| | Purasolv EHL | | 246 | | | | | |
| | Rapeseed oil methyl ester | | > 300 | | | | | |
| | Sec-butyl-4-oxopentanoate | n.a.[c] | 225-226 | | | | | |
| | triacetin | | 258 | | | | | |
| Carbonate | 2-Methyl furfuryl carbonate | n.a.[c] | 174 | | | | | |
| | Diethyl carbonate | | 126-128 | | | | | |
| | Dimethyl carbonate | | 90 | | | | | |
| | EPyrMC | n.a.[c] | > 300 | | | | | |
| | MTHFC | n.a.[c] | 203 | | | | | |
| | Propylene carbonate | | 240-243 | | | | | |
| Ketone | Methyl ethyl ketone | | 80 | | | | | |
| | cyclohexanone | | 155 | | | | | |
| Aromatic | p-cymene | | 176-178 | | | | | |
| | *o*-xylene | | 144 | | | | | |
| | Toluene | | 110 | | | | | |
| Ether | 1,3-dioxolane | | 74-75 | | | | | |
| | 2-methyl THF | | 78-80 | | | | | |
| | Anisole | | 154 | | | | | |
| | Cyclopentyl methyl ether | | 106 | | | | | |
| | Dimethoxymethane | | 41-42 | | | | | |
| | Plurafac LF711 | | >300 | | | | | |
| | Plurafac LF221 | | >300 | | | | | |
| | Plurafac LF303 | | 245-255 | | | | | |
| | Plurafac LF120 | | >300 | | | | | |
| | Dehypon LS54 | | >300 | | | | | |
| | Synperonic LF30 | | >300 | | | | | |
| | t-amyl methyl ether | | 85-86 | | | | | |
| Dipolar aprotic | Polarclean | | 280 | | | | | |
| | Steposol | | 297-298 | | | | | |
| | Agnique AMD810 | | 274 | | | | | |
| Chlorinated | Chlorobenzene | | 132 | | | | | |
| | 1,2-Dichlorobenzene | | 180 | | | | | |
| | Chloroform | | 61 | | | | | |

Fig. 6: Review chart of all solvents studied by Ho et al.[42] using TIPS-PEN as active material. The green, yellow and red colours refer to preferred, problematic, and not recommended solvents, respectively. FFa is an abbreviation of Film Formation ability, a parameter depending on solubility and dewetting capabilities.

### 2.2.1. State of the art: green-processed organic devices

In recent years, not much research has been done on green-processed sensing devices, with most studies relying on the commonly used halogenated solvents for semiconductor processing. Nevertheless, some interesting results have been achieved; recent work by Du et al.[43] reports high-

performance wearable organic photodetectors processed from the green solvent 2-methyltetrahydrofuran (2-MeTHF). These devices, proposed as wearable detectors of heart rate and blood oxygen levels, exhibit specific responsivities of ~ 0.4 A/W across the 400 to 900 nm range. This result, corresponding to around 80% of the responsivity obtained using a toxic solvent (o-xylene)[44], indicates the efficient conversion of incident radiation into photocurrent despite the use of a green solvent.

Green solvents are being analysed for the development of OPV, with varying results in efficiency; notably[45], OPVs with an efficiency above 14% were fabricated by spin coating deposition of the active component in anisole solution using limonene as co-solvent. The produced devices represent the best performing OPVs processed from an highly green and eco-compatible solvent to date. A parallel study by Zhang et al.[46] reported 2-methylanisole being employed as nontoxic solvent in the production of organic-polymer photovoltaic devices with efficiencies up to 9.7%.

Casula et al.[47] recently developed fully organic transistor devices, operable at low voltages, deposited on commercial paper through inkjet printing. anisole was adopted as solvent for the deposition in both n-type and p-type transistors, produced using ActivInk N1400 and TIPS-Pentacene as organic semiconductor respectively. In addition to anisole, cyclohexanone and diethyl carbonate have also been studied as possible green solvents to produce OFET devices[48]. The parameters variation in the solution shearing process was studied for these solvents, optimizing the electrical performances of the resulting devices (with a maximal hole mobility of 5.1 $cm^2/Vs$, they displayed similar characteristics to devices processed with toxic solvents).

Nevertheless, despite the clear benefits of using green solvents in organic semiconductors detectors production, the number of studies regarding sustainably manufactured ionizing-radiation detectors remains limited. This work inserts itself in this emerging field as a preliminary analysis of the potential use of green solvents for such applications.

### 2.3. The role of the electrodes in device architecture

Electrodes play a major role in the internal operation of any photodetector device: they influence the collection of charge carriers, as well as electrical noise, having a great impact on the detector's response.

When dealing with dosimeters, most notably, the choice of electrodes affects the tissue equivalence of the whole device: commonly used metallic electrodes display radiation absorption that differs significantly from that of biological tissues, thus hindering detection accuracy. Using fully organic detectors can solve this issue, thanks to their composition based on low Z elements (as for human tissues)[3]. This problem will be addressed in the next sections, whereas here a review of the main characteristics of electrodes for organic photoconductors is proposed.

When working with any kind of electrodes, to maximize the efficiency of charge collection at the interface with the organic semiconductor, a common strategy is to choose a semiconductor and an electrode material that exhibit favourable energy level alignment, thus minimizing injection barriers and contact resistance[49,50]. Metallic electrodes materials such as gold and silver are commonly used due to their high conductivity and low contact resistance when working with most semiconductors. At the same time other materials, such as conductive polymers, are studied thanks to their improved mechanical flexibility and easy solution processing (they are however not exempt from drawbacks, with higher sheet resistance values when compared to metal ones). Material choice remains thus one of the most important aspects to consider when designing a device.

The architecture of the device is equally important: to maximize charge collection and reduce transit distances in the active layer, interdigitated electrodes are the most commonly adopted structure[51]. If this design is adopted, a careful consideration of the fingers' length and spacing is needed to optimise the response and decrease dark current.

At the same time, the deposition processes employed are also important: materials that can be deposited through solution-based techniques are preferred, due to this class of procedures being easily adapted to large scale manufacturing at lower cost.

### 2.3.1 PEDOT:PSS as gold substitute

As mentioned in the previous section, gold is one of the most used materials in detector's electrodes, due to its exceptional electrical transport properties and chemical stability. However, as is typical for metals, it is not an ideal choice for optoelectronics, bioelectronics or dosimetry, due to lack of transparency and low tissue equivalence.

A promising alternative is represented by the organic polymer PEDOT:PSS. This material has shown excellent properties[52], displaying easy solution processability (can be deposited through spin-coating, printing, blade coating), high chemical and thermal stability and excellent compatibility with biological systems. It is also characterized by exceptional mechanical properties, due to its low Young's modulus value compared to most metal materials, being particularly fitting for integration in bendable and stretchable devices. Its transparency makes this material optimal for applications in optoelectronic devices. Lastly, being composed of low-Z organic elements, PEDOT:PSS possesses excellent tissue-equivalence properties, making it an optimal material for medical radiation detection. On its own, PEDOT:PSS is not a good conductor, but its electrical properties can be highly enhanced when treated with additional agents. Various solution additives have been studied, capable of increasing the material's conductivity, with some examples being 3-oxetanylmethanol[53], polysorbate 80[54] and polyethylene glycol[55]. The conductivity-enhancing organic molecules employed in this study are discussed in greater detail in the following chapter.

### 2.3.2 Chemical structure and functional properties of PEDOT:PSS

Pristine PEDOT:PSS is a composite material, with poly(3,4-ethylenedioxythiophene) (PEDOT) being an optically transparent, electrically conductive polymer and Polystyrene sulfonate (PSS) working as an additional agent to improve the water solubility and processability of PEDOT. PEDOT:PSS films display a differentiated structure, with grains of around 30 nm to 40 nm, composed of a PEDOT-rich core and PSS-rich external shell (as seen in Fig. 7). Grain cohesion arises from the hydrogen bonds between the PSS molecules in the shells.

In terms of mechanical properties, PEDOT:PSS shows high stability and good stretchability, with important variations based on the environment of operation. In fact, as reported by Lang et al.[56], at higher relative humidity levels weaker hydrogen bonds reduce grain cohesion and in turn mechanical strength. Despite this minor limitation, PEDOT:PSS has been reported as one of the best stretchable conductors on the market, with electrical performances under stress surpassing those of state-of-the-art carbon nanotubes and silver nanowires[57]. Another interesting characteristic of PEDOT:PSS is its ability to self-heal from mechanical damage when submerged in water[58].

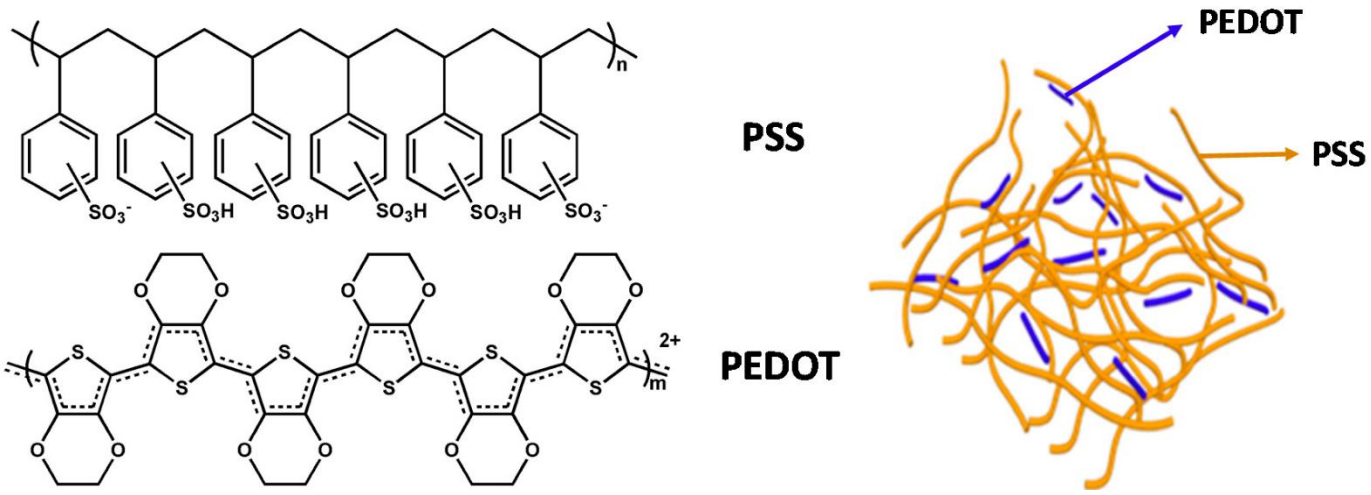


Fig. 7: Chemical structure of PEDOT and PSS (left) and schematic representation of the core and shell structure of PEDOT:PSS (right)[59].

Nevertheless, despite its good mechanical properties, pristine PEDOT:PSS films show limited electrical conductivity for most applications, mainly due to the presence of excess insulating PSS molecules and poor nanostructuring of the PEDOT ones. As mentioned before, these problems have however been extensively studied and mostly solved through additive treatments[13]. Here, in this brief review, only the additives employed in the thesis work are discussed. The additives of interest are mainly three, namely ethylene glycol (EG), Dodecylbenzenesulfonic Acid (DBSA) and Glycidyloxypropyltrimethoxysilane (GOPS). The first is a polar organic solvent with high boiling point, capable of increasing the PEDOT:PSS molecular chain's size, in turn generating larger nanocrystals after thin film deposition and augmenting the conductivity of the material[60]. EG has also demonstrated the ability to enhance the electrical and mechanical self-healing capabilities of PEDOT:PSS. The organic sulfuric acid DBSA is employed as an additional dopant for PEDOT, capable of improving film morphology and increasing elasticity and durability. Lastly, the methoxysilane-based molecule GOPS is used to prevent both dissolution and delamination of PEDOT:PSS films in aqueous solutions while also improving elasticity and substrate adhesion[61]. Tumova et al.[62] demonstrated that a cross-linking treatment using both DBSA and GOPS is particularly effective in further shielding PEDOT:PSS from delamination in biocompatible devices.

# *Chapter 3:*
# *Materials and Methods*

In the following, the materials and methods used during the thesis are described. First, an overview of the main materials employed in this study is presented, followed by a description of the device development process: photolithography and thermal evaporation are discussed, together with the process to pattern PEDOT:PSS electrodes, after which the deposition of the thin-film organic semiconductive component is described. To expand on this, in section 3.3.1. a comparison between toluene and anisole as solvents is drawn out. Section 3.4. details all the processes used to characterize the samples. This part closes with a brief description of the data analysis methods and tools used to extracts the results displayed in the next chapter.

### 3.1 Materials (PEDOT:PSS, TIPS-Pentacene, solvents)

The main materials employed in this study are briefly covered. The substrate used for all the devices prepared is Kapton®, a polymeric film of polyimide, chosen for its great mechanical flexibility (can be bent repeatedly, even up to a full fold of 180°), insulating properties and good thermal stability (with continuous operation certified for the range -269 °C to 240 °C)[63]. For the electrodes, either gold or PEDOT:PSS, as an organic, tissue-equivalent alternative, were employed. The PEDOT:PSS employed was prepared using four main components: Clevios™ PH1000, a water based dispersion of PEDOT and PSS, Ethylene Glycol (EG), adopted as conductivity booster due to its ability to promote PEDOT chain arrangement[64], GOPS, which enhances mechanical stability and makes the film insoluble in water[61], and DBSA, promoting thin film formation and improved conductivity. For a more detailed description of these components refer to chapter 2.3.1.

The active component for all devices was composed of a crystallized 6,13-bis(triisopropylsilylethynyl)pentacene (TIPS-Pentacene) layer, an organic semiconductor widely used in thin-film electronics (the molecular structure is displayed in Fig. 8a). Pentacene has a linear structure with five benzene rings, with chemical formula $C_{22}H_{14}$. It displays good crystal order, with a fishbone disposition for the single crystals with respect to each other. Unfortunately, poor π-stacking due to its edge-to-face herringbone molecular packing and low solubility in organic solvents limit its applications: to solve this problem, various molecular additions have been tested on the pentacene backbone. These functional groups can increase the solubility of the semiconductor, while also recombining the π-stacking, resulting in improved charge transport properties.

In particular, TIPS-Pentacene showed excellent solubility and improved electrical characteristics due to its brick wall molecular packing[65] (see Fig. 8b).

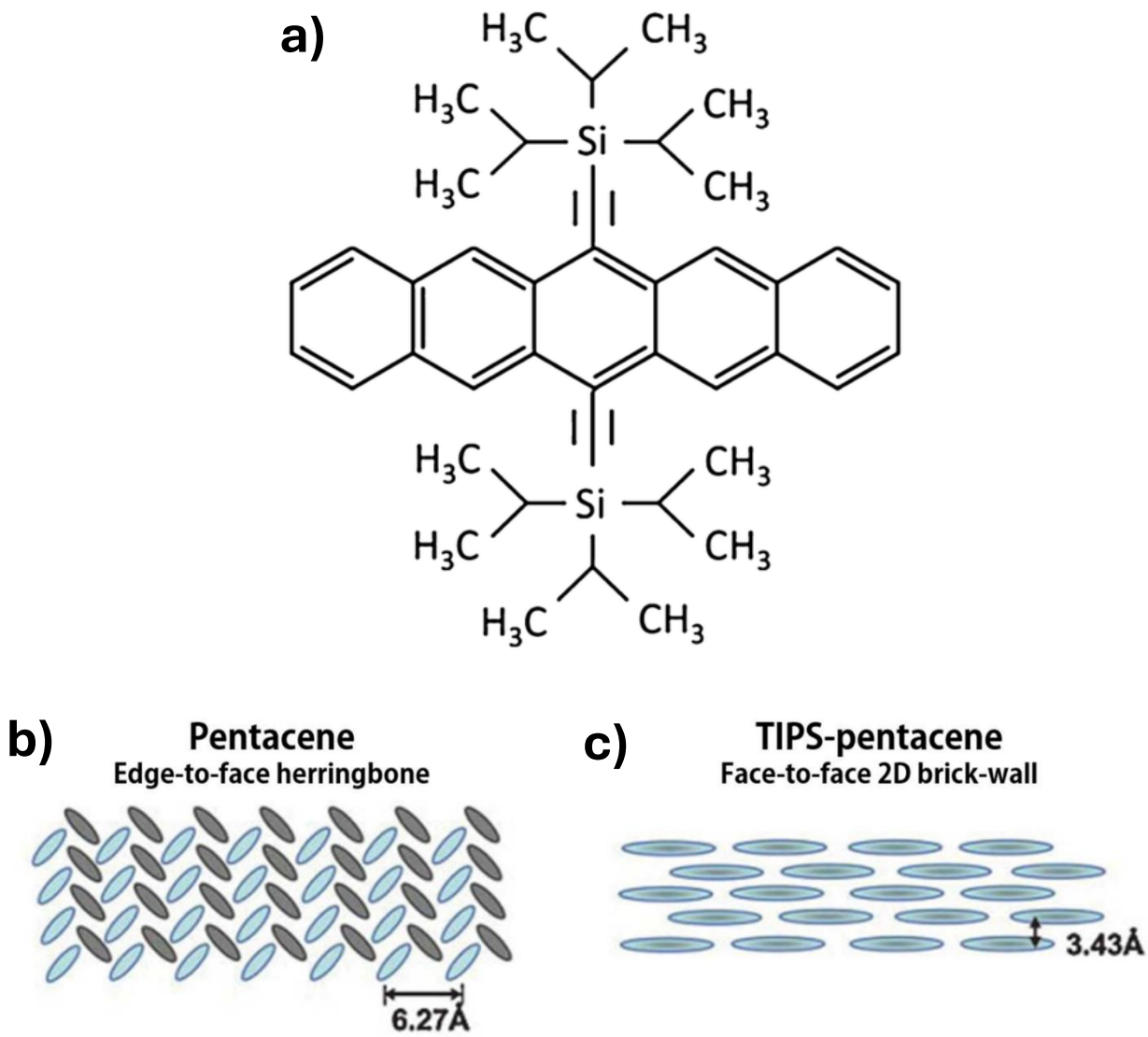


Fig. 8: a) Molecular structure of TIPS-Pentacene. Molecular packing of both the b) pentacene and c) TIPS-Pentacene molecules.[66]

To deposit the semiconductor on the electrodes area, a solution was prepared, using two different solvents based on the study performed. One was a commonly employed solvent for industrial and research purposes, toluene, known for its excellent solving ability as well as high toxicity. The other was anisole, a green solvent already singled out[11,67] for its promising features. A more in-depth study of the two solvents is presented in section 3.3.1.

### 3.2. Device fabrication

In the following a detailed description of the fabrication of the electrodes is presented as was performed in this work: starting from the preparation of the Kapton substrate, the electrodes' patterning process, performed through photolithography, is described. Two sections, namely 3.2.2. and 3.2.3., are dedicated to the preparation process of gold and PEDOT:PSS electrodes respectively; in fact, while the first one is performed through thermal evaporation, the other requires the use of spin coating deposition techniques to be achieved.

#### 3.2.1. Photolithography processes

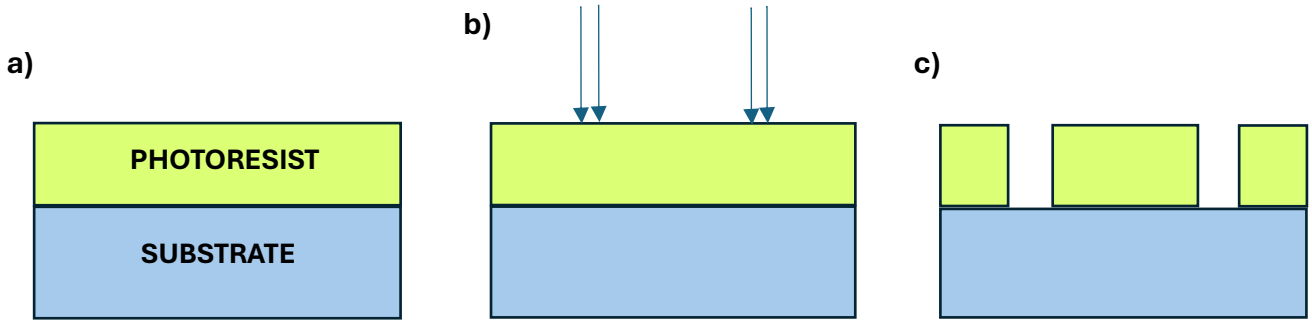


Fig. 9: Schematic representation of photolithography using a positive photoresist: a) the photoresist is deposited on the substrate. b) light is shone on the photoresist in a specific pattern. c) using a developer, the patterned section of the photoresist layer is removed.

Substrate preparation is the first fundamental step to fabricate a device. In this work, preceding the photolithography process, the substrates were prepared by cutting 5 x 5 $cm^2$ squares from a 75 µm Kapton foil and by cleaning such squares through ultrasonic bath (the cleaning cycle used Acetone, Isopropyl alcohol (IPA) and distilled water). The cleaning process was followed by a 1 minute long oxygen plasma treatment at 50 Watts, to clean the surface from external grains of dust and to increase surface energy, thereby improving wettability and film adhesion. Once the substrate is

ready, either a positive or negative photoresist is spin-coated on top. The MICROPOSIT™ S1818™ Positive Photoresist was chosen as photosensitive material in this study. 800 μL of S1818 were deposited on the substrate, placed on top of the spin coater's rotating platform. The chuck of the spin coater, by rotating at 4000 rpm for 1 minute, spreads the photoresist outward by centrifugal force, uniformly coating the substrate. The photoresist was then annealed for 1 minute on a 110 °C hot plate to completely evaporate the remaining solvent. Once the photoresist has been deposited, maskless photolithography, graphically described in Fig. 9, is used to pattern the desired architecture onto the material. This procedure doesn't require a physical mask of the desired pattern, but uses a mechanical, high precision machine capable of patterning directly the coated substrate by means of UV radiation or electron beam. When exposed to the adequate radiation, the photoresist undergoes a chemical crosslinking process, which renders the exposed regions soluble in a developer. In this work, an ML3 Pro Microwriter was used as patterning device (equipped with a 385 nm UV laser), due to its high precision (up to micrometric resolution) and the possibility to develop custom patterns through a software. For the development of the patterned photoresist, a Tetramethylammonium Hydroxide (TMAH) based developer is used (MF_319 microposit), after which a distilled water bath removes the remaining developer from the patterned substrate.

### 3.2.2. Thermal evaporation

Having patterned the electrode's architecture in the photoresist layer, thermal evaporation is the deposition technique of choice for the electrodes' material. In this process, the material to be evaporated is placed in crucibles, the temperature of which can be controlled through Joule effect, by making a current flow through them. The substrate is placed face down, directly above the crucibles. The materials placed in such crucibles are thus heated up, slowly reaching their melting temperature, at which they start evaporating in the environment, coating the surface of the substrate.

In this study, gold was evaporated as material of choice for some of the devices, with a thin layer of chromium used as adhesion enhancer between the gold and the substrate. The whole procedure is performed in a vacuum chamber equipped with both a rough (rotary) and high vacuum (turbomolecular) pumps, reaching up to $2 \cdot 10^6$ mbar. This is done to ensure that the evaporated material has high purity, without contamination of other agents from the environment. Moreover, a high vacuum ensures straight path movement of the evaporated particles, coating uniformly the interested area. To monitor the vacuum levels inside the chamber, both a thermal conductivity Pirani gauge and a cold cathode Penning gauge are used, for the rough and high vacuum levels respectively. A quartz microbalance inside the chamber is used to monitor the deposition process: in this work, a thickness of 7 nm for chromium and 40 nm for gold was optimally chosen. In Fig. 10 the evaporator's setup used is displayed. After evaporation, the excess of S1818 photoresist was removed by lift-off process: the samples were placed in acetone for 4 hours, undergoing short, low-power sonication processes every hour, followed by 30 seconds sonications in clean acetone, IPA and distilled water at the end of the process.

### 3.2.3 PEDOT:PSS electrodes fabrication

PEDOT:PSS was deposited on the patterned photoresist as an alternative to gold. This procedure is performed using spin coating as deposition technique. As mentioned in chapter 2.3.2. and 3.1., the PEDOT:PSS prepared comprised four main components: for a 5 mL solution, 4700 µL of PH1000, 250 µL of EG, 50 µL of GOPS and 12.5 µL of DBSA were prepared. Due to the tendency of GOPS to react quickly when mixed with PH1000, to achieve optimal film uniformity and electrical transport, the solution should be deposited as soon as possible after mixture. After the solution preparation, 10 minutes of sonication are used to ensure proper mixing.

Before spin coating, the solution is passed through a 1.2 µm cellulose acetate syringe filter to remove thicker grains. After spin coating the solution at 3000rpm for 10 seconds, the samples are

annealed on a hotplate for 1 hour at 100° C, after which the excess photoresist is removed by submerging them in IPA for 4 hours, with a brief, low power sonication performed after 2.

### 3.3. Organic semiconductor thin film deposition

The organic semiconductor chosen, TIPS-Pentacene, was deposited on top of the electrodes using drop casting technique. Since the semiconductor was stored in powdered form, to produce the best solution for deposition, the optimal concentration was studied for both solvents used. Before moving to the deposition process, a brief analysis of such solvents is presented.

#### 3.3.1. Toluene and anisole comparison

Both toluene and anisole are aromatic solvents, but they differ substantially in their physical and chemical properties. toluene is a low viscosity, low boiling point (around 110° C) liquid: thanks to these properties it is optimal for fast solvent evaporation during deposition, enabling quick crystallization. Unfortunately, toluene is also known for its significant toxicity and high volatility[68,69].

Anisole represents a greener alternative to toluene, with a lower toxicity and a more stable chemical profile. Moreover, this solvent displays both higher viscosity and a higher boiling point (around 155° C) than toluene, promoting a slower crystallization (extended evaporation times can lead to larger crystal domains, but it might also hinder crystallization if not performed in a controlled environment).

The molecular structure of both solvents is displayed in Fig. 11.

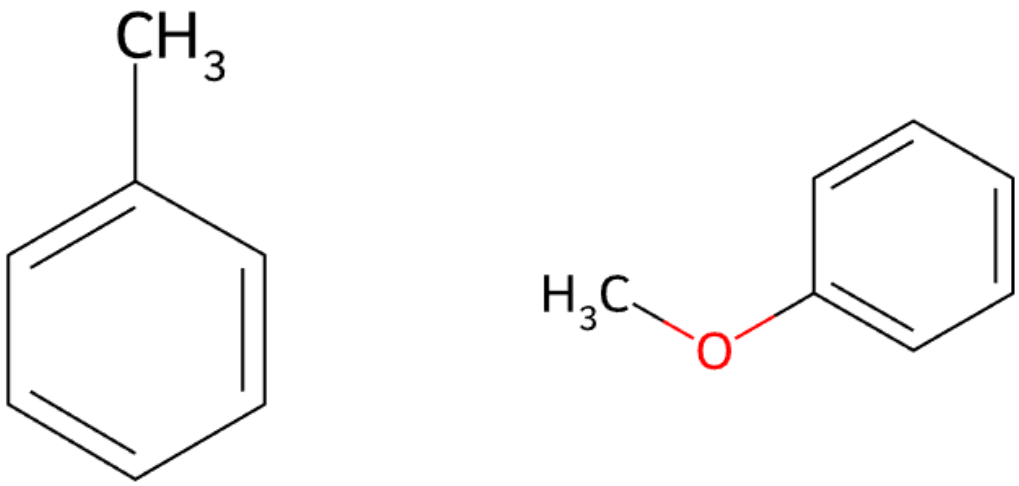


Fig. 11: Chemical structure of the toluene (left) and anisole (right) molecules.

In this work, the solutions were prepared by mixing these solvents with the semiconductive component in a small vial, stirring them for 30 minutes at 1000 rpm, over a 90° C heated hotplate. The optimal concentration for the toluene-based solution as reported in the literature is 4.3 mg/mL[20]. The optimal concentration for anisole was found to be of 6 mg/mL after being investigated as reported in appendix A.

### 3.3.2. Drop casting deposition

Drop casting is a simple deposition technique used for thin films and small single crystals. It consists in dropping the solution directly on the heated substrate: the solvent slowly evaporates, leading to spontaneous crystallization of the solute, as depicted in Fig. 12. The choice of substrate temperature and annealing time are fundamental to engineer optimal crystal features.

In this work, the semiconductor's solution was deposited immediately after preparation, exclusively on top of the electrode's fingers. Once 2 µL of solution were dropped using a micropipette on top of the devices, these were covered using a glass hemispherical dome to create a confined atmosphere above the sample, controlling the evaporation rate and facilitating uniform crystallization. This was

particularly important when working with anisole, due to its slower evaporation. The hotplate was kept at 90°C throughout both the deposition process and the whole 3 hours of the annealing process.

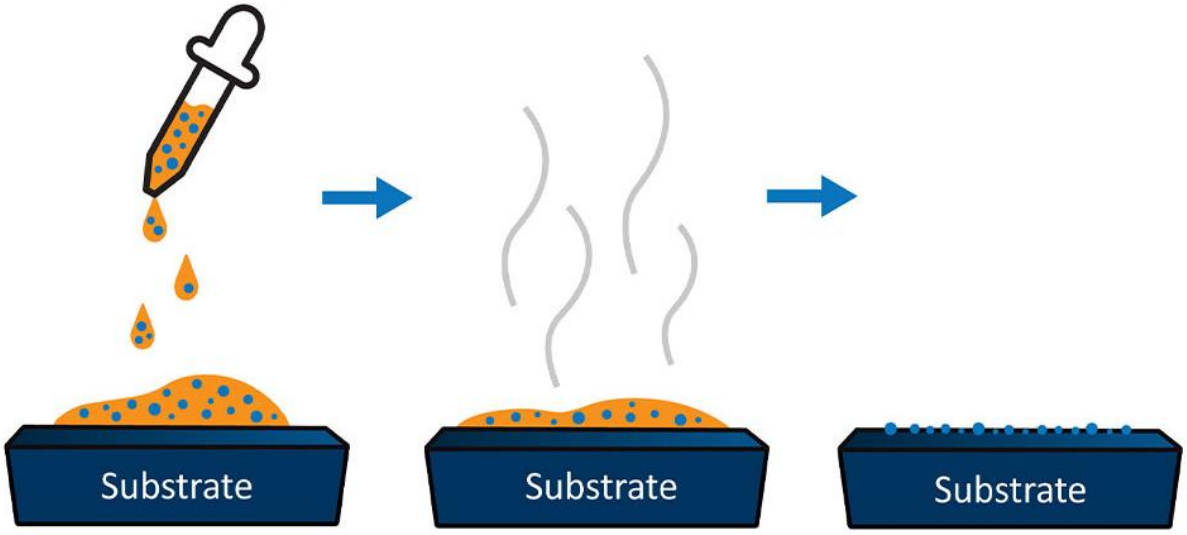


Fig. 12: Graphical depiction of the drop casting process: the deposited solution evaporates on the heated substrate, leaving behind only the crystallized solute.

### 3.4. Device characterization

The characterization of the devices has been divided into three main categories: morphological, comprising optical microscopy and light interferometry analysis, electrical, corresponding to IV measurements, and radiation related, with photocurrent measurements for both X-ray and UV radiation.

#### 3.4.1 Morphological characterization

A first morphological study of the devices was done using an Optika B-383MET optical microscope. Through this, the TIPS-Pentacene crystals quality and size was evaluated. For a more detailed characterization of the deposited layer the gbs smart white light interferometer (smartWLI) with a 20x lens amplification was employed, in order to extract information on the film's thickness and roughness with nanoscale precision. This characterization is based on the generation of interference patterns by combining light waves of different wavelengths. White light is split through a beam splitter into two paths, one used as reference and one containing the sample. Depending on the sample's characteristics, the optical path of the light waves interacting with it is varied from the one of the reference path. This difference creates sample-dependent interference patterns when the light waves from both paths recombine at the detector. By analysing these patterns, a detailed map of the sample's morphology can be reconstructed. This is done through multiple Fourier transformations algorithms, capable of converting the raw data into spatial frequency components associated to the surface morphology. The thickness of the active layer was measured as the height difference between substrate height and layer's height at around 1 mm distance from the coffee ring formed during deposition. The roughness measures, on the other hand, were evaluated on an area of around 100 $\mu m^2$ taken in the layer's inner parts.

### 3.4.2. Electrical characterization

The electrical studies performed consisted in current over voltage (IV) measurements taken for all samples under yellow light or in dark conditions. During IV characterization, the current variations are observed while a controlled voltage is applied to the device; by analysing the obtained current over voltage curve, the sheet resistance of the device can be determined. For all samples analysed in this work, the IV were taken from -5 to 5 Volts, with steps of 0.5 Volts every 500 milliseconds.

For the measurements taken under yellow light, a micro probe Nextron system was used to contact the electrodes, with the data acquired using a Keithley 2614b SourceMeter. The measures were taken in such conditions because TIPS-Pentacene is sensitive to white light, with reported high photooxidation when working with semiconductive thin-films[70].

For the measurements taken in dark conditions, before and after X-ray irradiation, the contacts were done using copper wires contacted with silver paste, with the data also acquired using a Keithley 2614b SourceMeter.

Further electrical measurements can be performed to assess the response of the detectors under UV and X-ray, as will be discussed in the following sections.

### 3.4.3. UV detection characterization

To study the effects that UV radiation has on the devices, a real time acquisition of the current response of the detector when irradiated was performed. By powering on and off the UV source, the dynamic current response gives information on the ability of each device to respond to this type of radiation and can be used to extract the detector's responsivity as detailed in section 3.5.

The UV light employed for irradiation was produced using a high intensity, 385 nm LED, mounted on top of an elevated base with a central opening kept at 4.8 cm above the samples. The calibration

of the LED, needed to find the irradiance to current relation of the device, was performed in this work using a ThorLab PM400 optical power meter. The calibration curve can be seen in Fig. 13 below, where the linear dependence between irradiance and driving current is clearly visible.

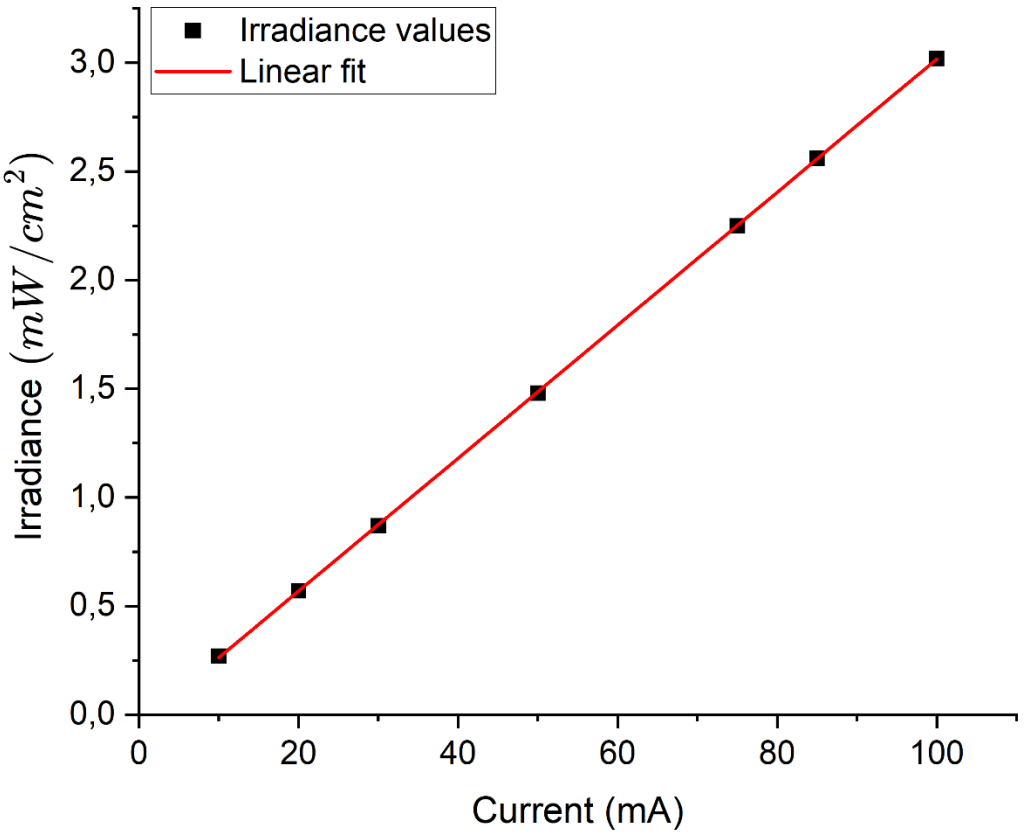


Fig. 13: LED calibration performed at currents of 10, 20, 30, 50, 75, 85 and 100 mA.

The strong linear correlation is evidenced by a coefficient of determination $R^2 \approx 0.99$.

All measurements were performed inside a probe station, an instrument used for electrical characterization, comprising tungsten, needle-like probes used to precisely contact the device electrodes. This station is enclosed in a metal box used to both as shield from electromagnetic noise coming from the outside and to prevent light interacting with the devices during measurement. The detection of the current was performed with a Keysight SMU device, used to also power the LED. Dynamic curves were taken for light intensities of 0.3, 1.5, 3.0 and 6.1 mW/cm$^2$, performing on/off switches of the UV source every 60 seconds while keeping each device at its own different bias, chosen to ensure comparable dark currents across all samples.

### 3.4.4. X-ray detection characterization

X-ray response characterization was performed using the detection apparatus reported in Fig. 15.

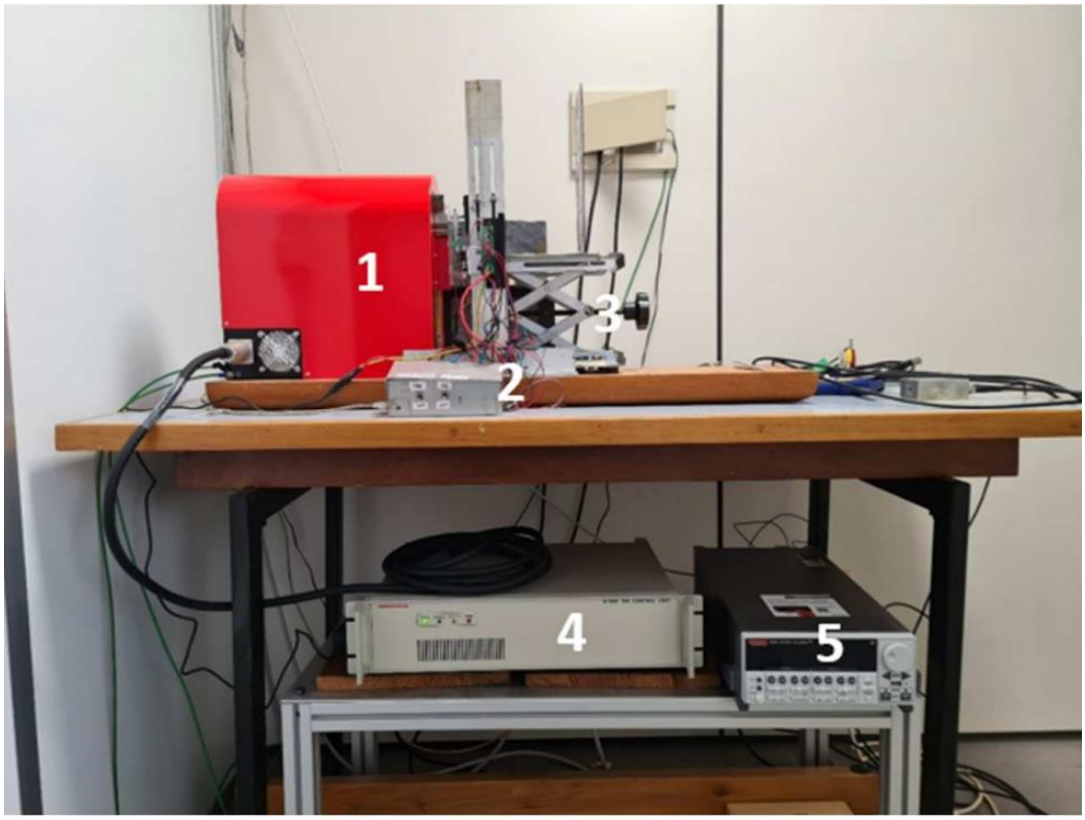


Fig. 15: Experimental apparatus for X-ray measurements: the X-ray tube (1) is connected to the voltage generator (4). The rotating lead shield is operated using an Arduino chip placed in a metal box (2), connected to an external PC. A metal base of varying height (3) was used to ensure proper alignment between the tube and the samples (if needed, a lead shield can be placed in between the tube and the base to protect unshielded elements of the devices). The Keithley 2614b SourceMeter (5) was used for the photocurrent measures.

A Tungsten X-ray tube, powered through an external high voltage generator, was employed as source of radiation. By modifying the tube's voltage and current, the energy and dose rate of the emitted radiation can be determined respectively. In Fig. 16 the tube calibration, done using a BARRACUDA X-ray Analyzer detector, is also displayed.

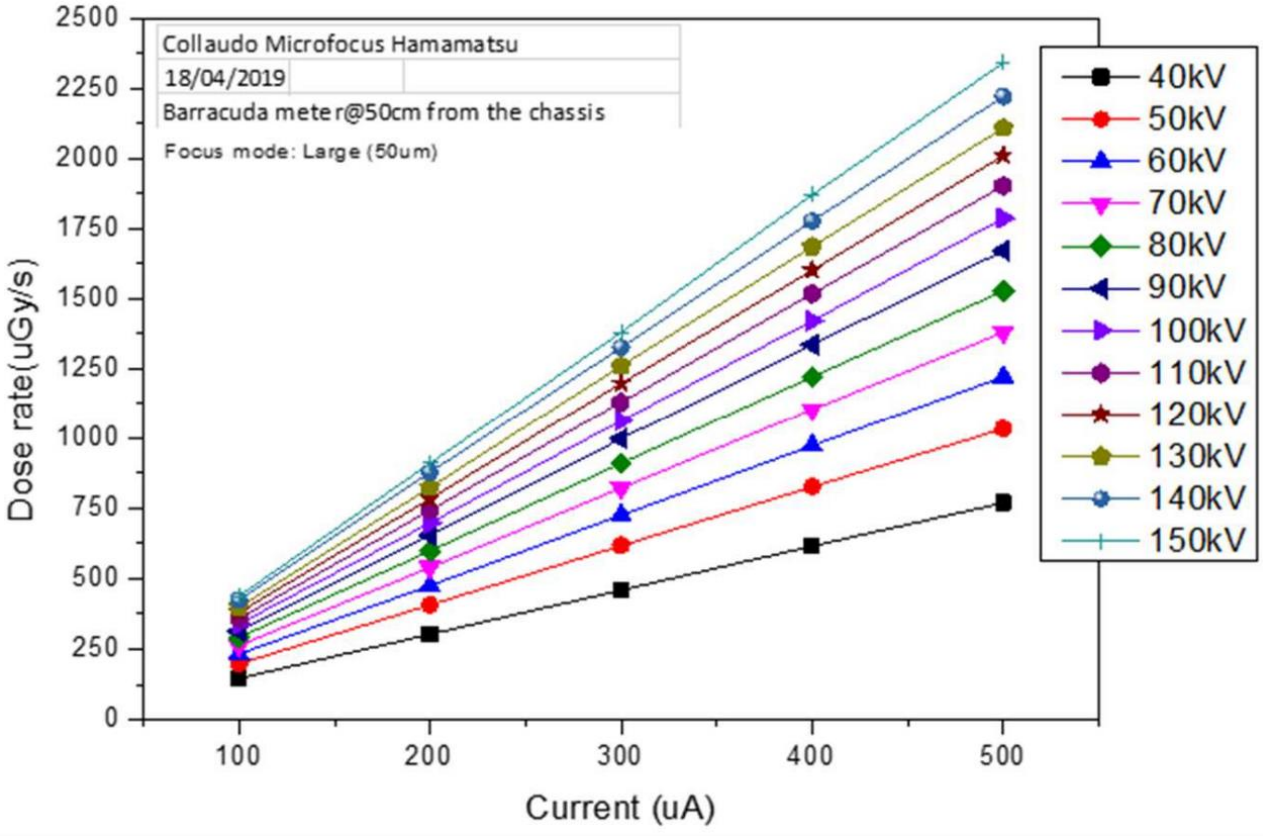


Fig. 16: X ray tube calibration. The calibration has been done placing the BARRACUDA X-Ray Analyzer at 50 cm from the X-ray tube.

In all the measurements performed the distance was 20 cm, from which the different dose rates considered during the irradiation sessions were extracted, with tube voltage fixed at 40kV and varying tube current (Tab. 1).

| Current (μA) | Dose Rate (μGy/s) |
|---|---|
| 100 | 760 ± 30 |
| 200 | 1600 ± 60 |
| 300 | 2430 ± 90 |
| 400 | 3290 ± 130 |
| 500 | 4340 ± 170 |

Tab. 1: Tube currents and correspondent dose rates for a 40 kV tube voltage at 20 cm.

A shutter mechanism, composed of a rotating lead shield, was controlled via custom LabView software to "switch" on and off the flow of X-rays reaching the samples. To extract the current data, the same SourceMeter device employed for the electrical measures was used. The devices, contacted through copper wire and silver paste, were kept inside small plastic boxes, placed behind a lead shield with a narrow hole (to screen the readout and the connection components from the ionizing radiation). Once the devices were placed inside the boxes, these were sealed to make sure no light could penetrate inside, limiting the photooxidation of the TIPS-Pentacene layer[70] as mentioned before. To ensure that the X-ray beam reached the active region of the devices inside the boxes, a test exposure was performed using a Gafchromic radiographic film placed at the device position and aligned the device accordingly.

The detection mechanism consists in the real time acquisition of the current crossing the device as a function of time. As described in chapter 1.2.1, when the X-ray radiation hits the thin-film semiconductor, the generated electron-hole pairs, separated by the applied electric field, give rise to a photocurrent, defined as the difference between the measured and the dark currents. By extrapolating the photocurrent through this measurement, the sensitivity of the device can be derived, as will be explained in the next section.

### 3.5. Data analysis

For the morphological studies, Mountains®9 was employed as post processing software to extract the thickness and roughness data. The analysis performed over the electrical acquired data was done either using personal MATLAB scripts or directly on the graphing program OriginLab. In particular, the sheet resistance was extrapolated, as will be discussed in the results, from the IV measurements data using the fitting tools of Origin. The device sensitivity was extracted through the following procedure: at first the saw-tooth shaped dynamic curves were cut, with only the uniform responses being considered. After this, to take into account the current drift, each curve was normalized by subtracting from it the parabolic fit of its on-off minima, as detailed in Fig. 17. After cleaning the signal in such a way, the mean of the maxima for each dose rate was calculated. Such means should be in a linear relation with the dose rates, and the sensitivity of the device can be extracted from the photocurrent over dose-rate plot as the slope of the linear fit.

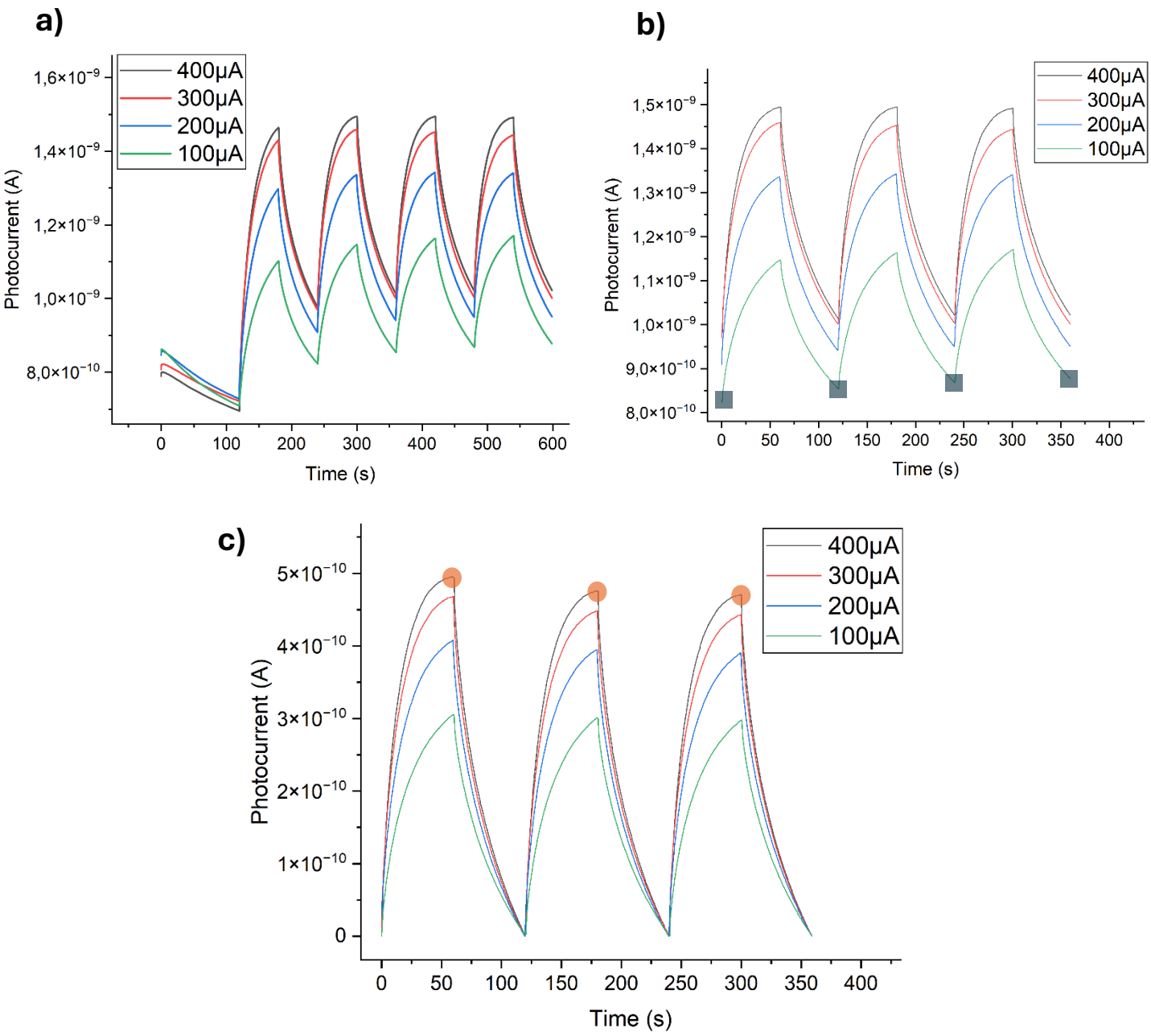


Fig. 17: Steps for the extraction of the photocurrent values. a) plot of the raw measurements data. b) plot of the cleaned-up data, with blue squares indicating the points to consider when calculating the parabolic fit used in the normalization process. c) Plot of the final dynamic curves, with orange dots indicating the peaks to consider when calculating the average of the photocurrent's maxima.

However, due to inner mechanisms related to the trapping states of the devices, the linearity is not always respected. In this case, as it was for the data reported in this work, the sensitivity was extracted as the maximum derivative of the photocurrent over dose rate plot, using the differentiate tool of Origin. In a similar way to sensitivity, the UV responsivity of the devices was extracted as the slope of the linear fit of the photocurrent over light intensity plot.

# *Chapter 4:*
# *Results and discussion*

In the following chapter, after a brief introduction of the batches of devices under study, the main results regarding their morphological, electrical, UV-Vis and X-ray characterizations will be presented.

## 4.1. Overview of fabricated devices

All the devices prepared in this work share the same substrate and photoconductor architecture, with an active layer of TIPS-Pentacene deposited on top of an interdigitated electrodes' structure (Fig. 18). For all samples the interdigitated structure has the same pixel area of 4 $mm^2$. All the parameters are reported in Tab. 2.

In this thesis two different studies are performed, with the aim to investigate the impact on the X-ray photoconversion process of:

- the employment of PEDOT:PSS electrodes as an organic alternative to conventional gold contacts.
- TIPS-pentacene semiconductor active layer processed with the use of a green solvent, i.e. anisole, in place of toluene.

A first batch of samples, fabricated using toluene as solvent for the active component, is analysed to probe the differences in detecting capabilities between samples with gold electrodes and PEDOT: PSS electrodes in interdigitated configuration. The role of anisole concentration in photodetection performance when used as solvent for TIPS-Pentacene is

investigated using five different solvent-to-solute ratios. Lastly, the response to UV-Vis light and X-rays of both gold and PEDOT: PSS electrodes samples produced using anisole as solvent for the active semiconductor material is analysed.

In Tab. 2 below the fingers' features are specified together with the pixel area of the interdigitated electrodes, while a graphical representation of such features is shown in Fig. 18.

| Channel length (L) | Finger length (F) | Channel width (W) | No. of channels | Pixel area |
|---|---|---|---|---|
| 60 µm | 50 µm | 2 mm | 20 | 4 $mm^2$ |

Tab. 2: Device features common to all batches.

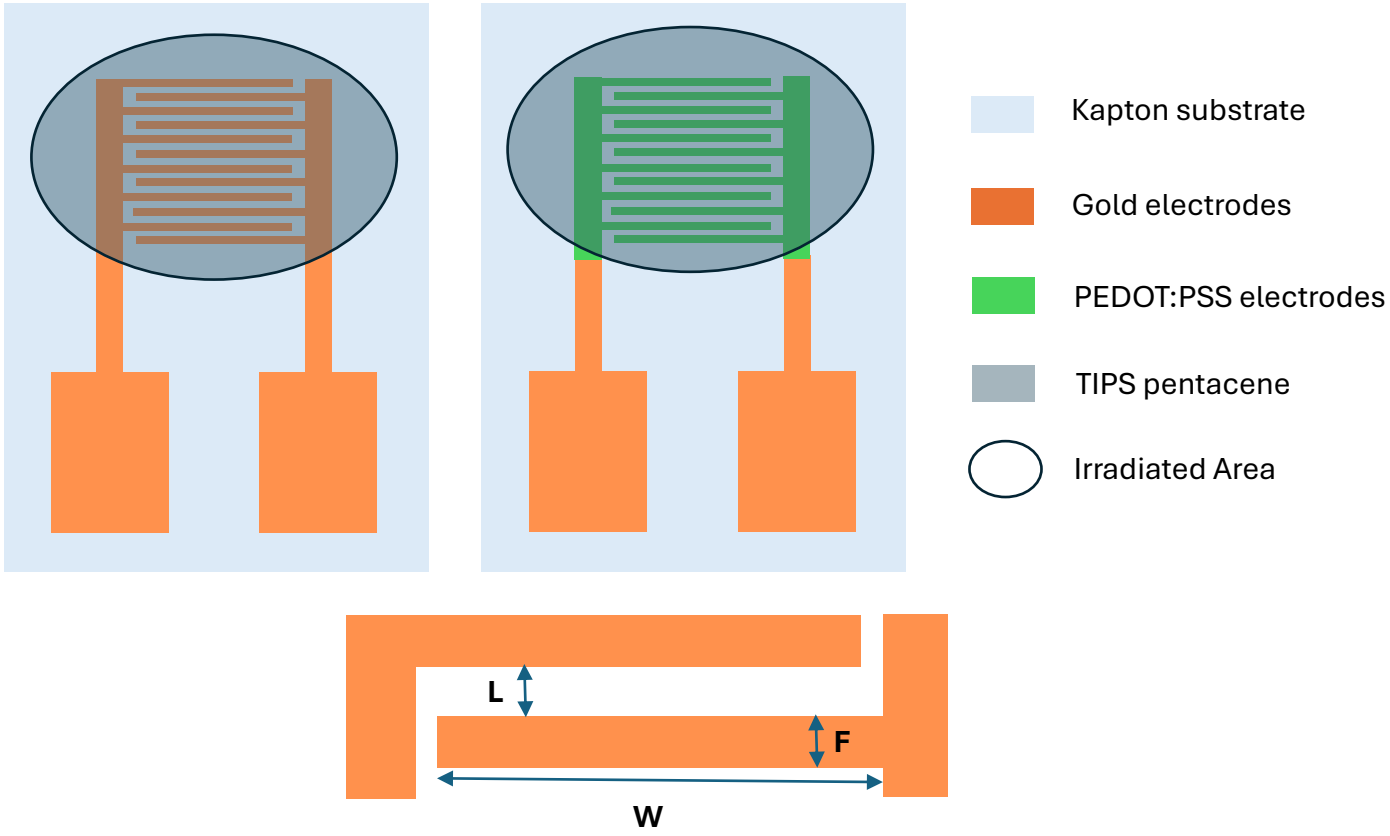


Fig. 18: Top-down view of the sample's architecture for Gold (left) and PEDOT:PSS (right) fingers (top). Section of the fingers' architecture with highlight of the features presented in Tab. 2 (bottom).

A resume table of the batches under study in this work is presented below (Tab. 3).

| Batch | Electrode material | Solvent | Number of samples | Characterization | Sections of discussion |
|---|---|---|---|---|---|
| OD01 | Gold | Anisole | 20 | Electrical, X-ray | 4.2.1, 4.2.2 |
| OD02 | Gold | Toluene | 20 | Electrical, X-Ray, UV | 4.2.1, 4.2.2, 4.3.3 |
| OD03 | PEDOT:PSS | Anisole | 10 | Electrical, X-ray, UV | 4.3.3 |
| OD04 | PEDOT:PSS | Toluene | 15 | Electrical, X-ray | 4.2.1, 4.2.2 |

Tab. 3: Information table on all working batches analysed in this thesis.

The first batch, namely OD01, consists of a total of 20 samples: these have TIPS-Pentacene in anisole solution deposited on top of gold electrodes. 15 of these samples have been fabricated at different concentrations (namely 1, 2, 4, 6 and 8 mg/mL, with three samples each) to find the optimal value for the anisole solution (this study's results are discussed in appendix A). Batch OD02 has the same size, comprising samples with gold electrodes, on top of which a TIPS-pentacene in toluene solution of concentration (4.33 ± 0.06) mg/mL has been drop cast. Batch OD03 is comprised of 10 samples, where a toluene solution of the same concentration as batch OD02 has been deposited on top of PEDOT:PSS electrodes. Lastly, a newly prepared anisole solution, with a concentration of (6.00 ± 0.16) mg/mL, has been drop cast on top of 10 samples with PEDOT: PSS fingers, comprising batch OD04.

### 4.1.1. Morphology

In the following the morphological study of the samples conducted via optical microscopy and white light interferometry is discussed.

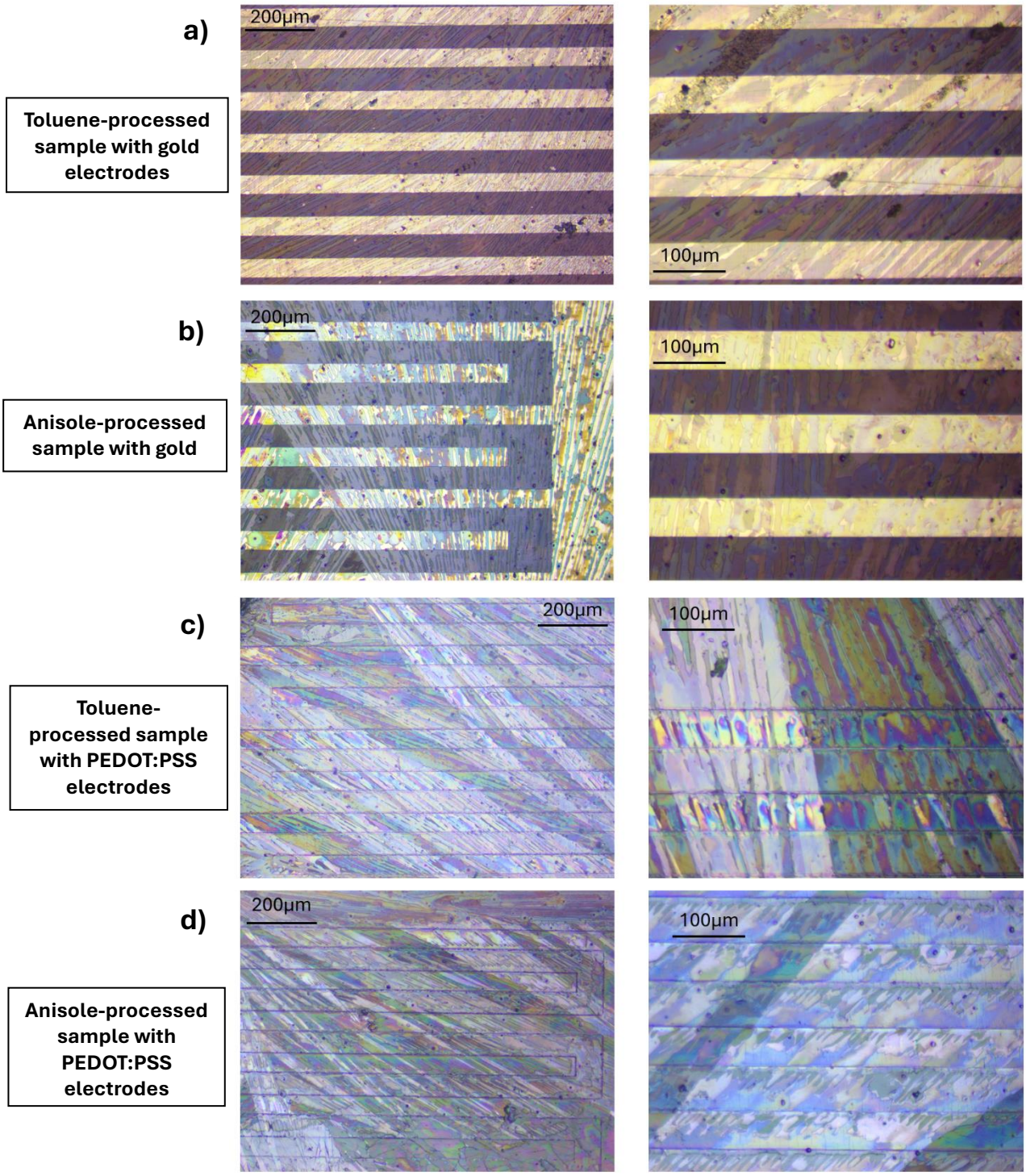


Fig. 19: Optical microscope images of the four main types of samples with a 10x magnification on the left and a 20x magnification on the right; a) toluene on Gold, b) anisole on Gold, c) toluene on PEDOT, d) anisole on PEDOT.

As can be seen in the optical microscope images (reported in Fig. 19), for all four main kinds of samples (toluene or anisole on either gold or PEDOT:PSS fingers) a good crystallisation is achieved without noticeable differences in crystal size, with widths of tens of micrometres, comparable to those observed by Akkerman et al.[71]. In particular, the process is not hindered using anisole, proving crystallisation to be efficiently achievable with a green solvent. Similarly, the presence of PEDOT: PSS doesn't alter crystallization quality. Additional morphological analysis, performed with an optical profilometer, is also important to assess the deposition quality of the drop cast solution: an active layer's thickness of a few hundred nanometres (with an average of (230 ± 40) nm across all samples), as achieved in the literature by both Basiricò et al.[10] and Akkerman et al.[71], is obtained as detailed in Tab. 4. In Fig. 20 the morphology of various samples is displayed.

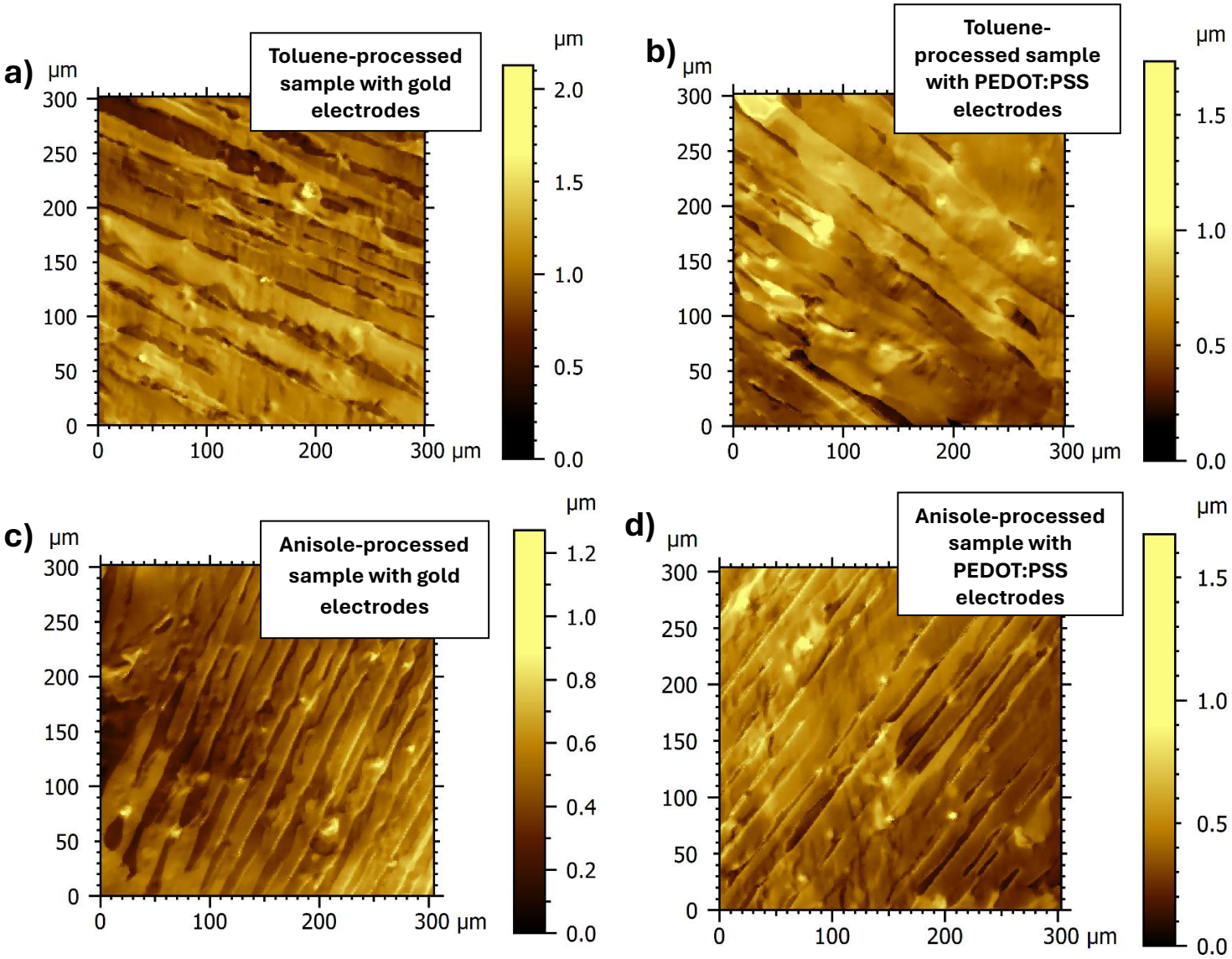


Fig. 20: Morphological profile of samples with gold electrodes processed with a) toluene or c) anisole and PEDOT:PSS electrodes processed with b) toluene or d) anisole.

The roughness results, displayed in Tab. 4, have low values when compared to the literature[72] (a 77 nm roughness was found for toluene processed TIPS-pentacene deposited through spin coating), an indication of a more uniform film morphology. A more homogeneous surface is typically associated with fewer structural defects and, therefore, a lower likelihood of trap formation that can degrade electrical performance.

| Device type | TIPS-pentacene Thickness (nm) | Roughness (nm) |
|---|---|---|
| Gold Fingers/ Toluene solution | 220 ± 20 | 41± 5 |
| PEDOT: PSS Fingers/ Toluene solution | 260 ± 40 | 43 ± 3 |
| Gold Fingers/ Anisole solution | 250 ± 50 | 37 ± 5 |
| PEDOT: PSS Fingers/ Anisole solution | 180 ± 30 | 35 ± 3 |

Tab. 4: Active semiconducting layer's thickness and roughness means measured for multiple samples of each device type.

### 4.1.2. Electrical Characteristics

We report here the electrical characterizations conducted on the different batches, consisting of current-voltage (IV) measurements taken both under yellow light and in dark conditions. The measurements are not performed under white light to prevent photooxidation of the TIPS-Pentacene[70]. A detailed look at the IVs of all working samples taken under yellow light is presented in Appendix B. A comparison of the sheet resistance $R_s$ for different types of samples, extracted from the IV measurements performed under yellow light right after fabrication, is presented (Fig. 21b). This parameter is used when working with planar geometries of uniform thickness and provides a good estimation of the electrical charges' ability to travel in the plane of the film[73].

To calculate $R_s$, equation 4 from section 1.4.1 is used: the resistance R is extracted from the linear fit of the IV curve of the sample while the device's number of channels, channel length and width are taken as listed above in tab. 1. Through this analysis we probe the impact of PEDOT:PSS and anisole on the conductivity of the devices.

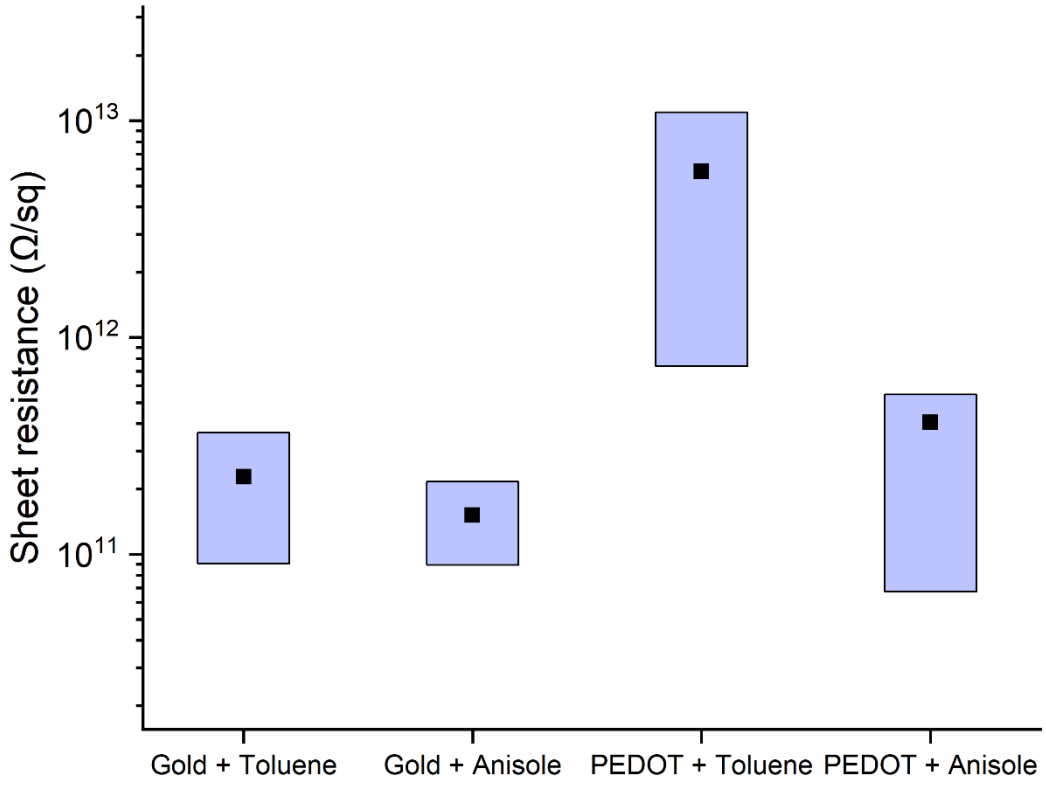


Fig. 21: Graph comparing the sheet resistance of all working samples for each type of device; the sheet resistances are calculated from the IVs performed under yellow light following the samples' fabrication.

From Fig.21 it is easy to see that, for both solvents considered, the sheet resistances of samples with PEDOT:PSS fingers are higher than the gold electrodes counterparts, implying a lower conductivity of the organic polymer. While the toluene processed samples display an increase of one order of magnitude (with averages of $R_{S.G.} = (2.3 \pm 1.2) \cdot 10^{11}$ Ω/sq and $R_{S.P.} = (6 \pm 3) \cdot 10^{12}$ Ω/sq, for the ones with gold and PEDOT:PSS electrodes respectively), the anisole ones show much more comparable values (with averages of $R_{S.G.} = (1.5 \pm 0.3) \cdot 10^{11}$ Ω/sq and $R_{S.P.} = (4.0 \pm 1.6) \cdot 10^{11}$ Ω/sq, for the ones with gold and PEDOT:PSS electrodes respectively).

In particular, it should be noted how the devices with gold electrodes display comparable sheet resistances independently of the solvent used for the semiconductor's deposition process, with the average value of anisole processed samples 35% lower than the one of toluene processed ones. Although this difference is minimal when dealing with gold electrode samples, it becomes much more evident when considering devices with PEDOT:PSS electrodes, with a difference of one order of magnitude for the average sheet resistance values between the two solvents. This might be due to a combination of the lower wettability of toluene based solutions and the lower conductivity of PEDOT:PSS when compared to gold. Further study is needed to improve the reproducibility and increase the results uniformity.

#### 4.1.3. Aging

Electrical measurements on all batches of samples (in particular, of the samples processed with toluene, 4 were analysed for both gold and PEDOT:PSS electrodes devices, while of the anisole processed ones, 6 had gold electrodes and 9 PEDOT:PSS ones) have been performed repeatedly over the span of 2 months to study the evolution of the electrical characteristics of the devices. As mentioned before, such measurements have been performed under yellow light to prevent the photooxidation of the organic semiconductor. The sheet resistances variations over time are displayed in Fig. 22. As can be seen their values increase monotonically. This behaviour is associated with the decrease in conductivity of the organic semiconductor due to aging[70]: even when the samples are protected from light exposure to prevent photooxidation, a much slower but still relevant oxidation process in dark conditions takes place. Due to oxygen permeation inside the material, an electron from the first excited singlet state of pentacene can transfer to the oxygen, causing the formation of endoperoxide and dimeric peroxide as a byproduct of subsequent reactions. These byproducts not only hinder the

TIPS-pentacene's π-stacking, but also introduce electronic traps and molecular disorder, affecting the material's conductivity[74].

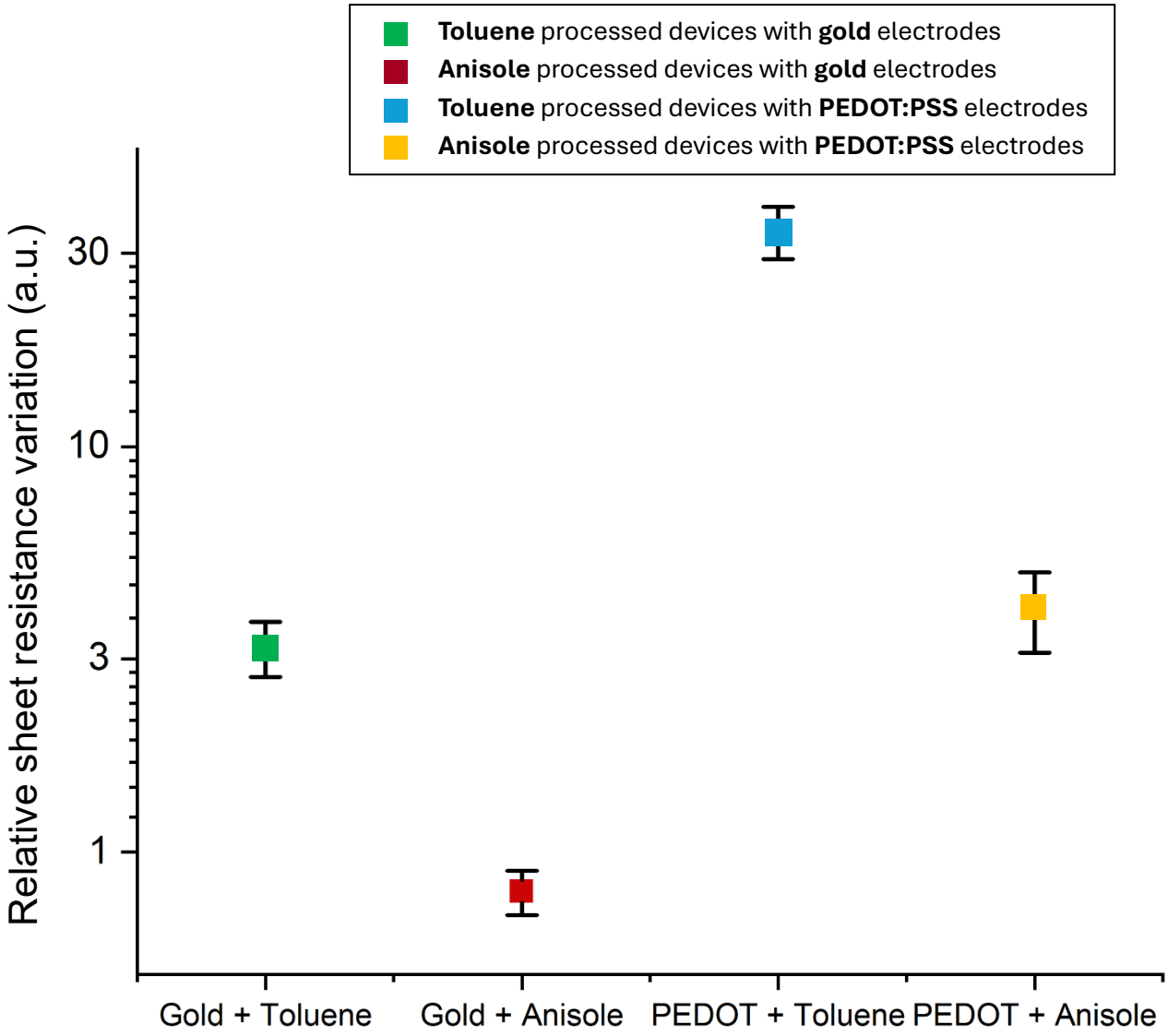


Fig. 22: Average sheet resistance relative variation over a time of 2 moths for all samples considered.

In particular, after 2 months, the samples processed with toluene display an increase in sheet resistance of a factor of (3.2 ± 0.5) for gold electrodes and of (34 ± 5) for PEDOT:PSS electrodes ones. The discrepancy between gold and PEDOT:PSS devices can be ascribed to the deterioration in conductivity of the conductive polymer, in line with the literature[75] data, predicting a decrease in conductivity up to two orders of magnitudes in the span of less than two months. When analysing the anisole devices, the increase in sheet resistance was of a

factor of (0.8 ± 0.1) for gold electrodes devices and of (4.0 ± 0.9) when using PEDOT:PSS, further proving the higher degradation over longer periods of time when working with the organic polymer. Notably, when comparing devices with the same electrode material, the sheet resistance relative variation of anisole processed ones is considerably lower, hinting at a better stability of the semiconductive component processed with this solvent (possibly due to better solution wettability and film formation quality). Further studies are needed to stabilize the PEDOT:PSS performances over longer periods of time. For a detailed look at the sheet resistance variation for samples from each type of device, refer to Appendix B.

## 4.2. Influence of the solvent on detector performance

This thesis' work has as a main objective the evaluation of possible green solvent substitutes to be used in the deposition process of the detector's active material. In this section the detecting capabilities of devices from batches OD01 and OD02, prepared with either toluene or anisole solvents, will be compared and discussed.

### 4.2.1. X-Ray response

In fig. 23 the dynamic X-Ray responses of devices at a fixed dose rate (the full characterization of the devices over all dose rates considered is presented in appendix C) and fixed operational bias of 1V are reported together with their corresponding photocurrent – dose rate plot; here the responses of gold electrodes samples, fabricated using toluene and anisole as solvents for the active layer, are compared. The typical saw tooth shape of the dynamic curves, caused by the semiconductor's deep electron trapping sites and the subsequent photoconductive

gain process caused by them (see chap. 1.3.2.), is clearly visible in fig. 23a for both solvents utilized.

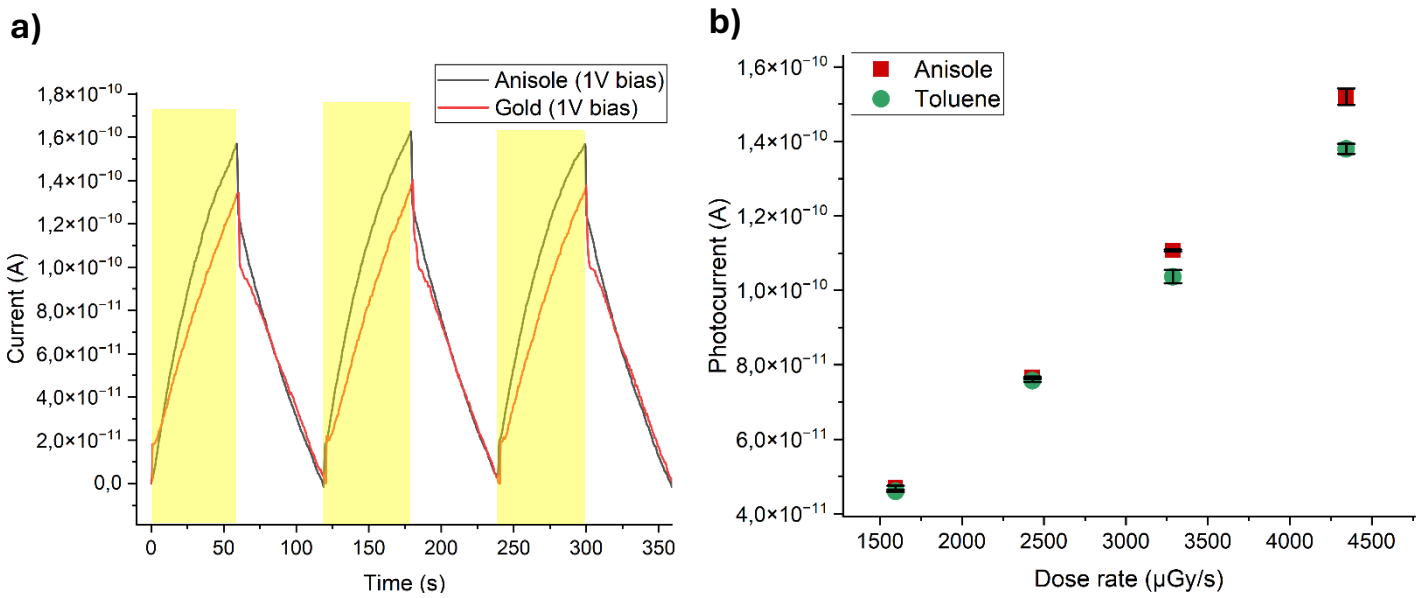


Fig. 23: a) Dynamic curves taken at a dose rates of (4.34 ± 0.17) mGy/s for gold electrodes samples fabricated using either a toluene or an anisole based solution. The regions highlighted in yellow indicate the irradiation intervals. b) Photocurrent over dose rate plot of both devices.

Fig. 23b shows that for both solvents the photocurrent increases proportionally to the dose rate. The sensitivity of the device was extracted as the maximum of the incremental ratios as previously detailed in chapter 3.5. Having extracted all sensitivities for the working samples of both types, these are compared as detailed in Fig. 24. It must be noted that while the devices processed with toluene were all operated with a bias of 1V, the driving voltage of the anisole processed samples was varied (from 1 to maximum of 4.4 Volts) to ensure comparable dark currents, as mentioned before.

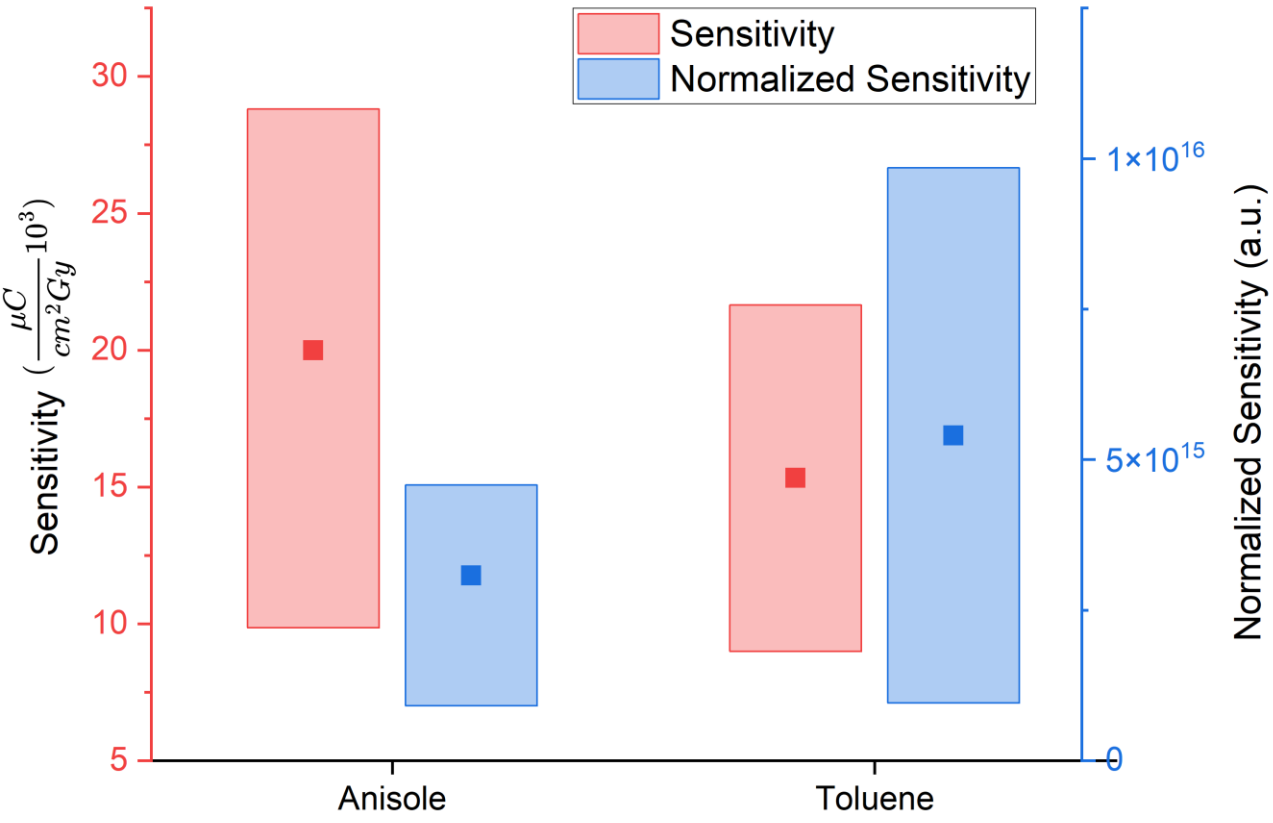


Fig. 24: Anisole and toluene Sensitivity comparison chart: both standard (red) and normalized for the sample's sheet resistance (blue) sensitivities are displayed. Averages are indicated by darker squares in each box.

To remove the dependence on charge-transport properties, a normalized sensitivity (calculated by multiplying each sample's sensitivity for the corresponding sheet resistance) is also compared. In both cases, it is possible to see that the results are comparable in magnitude, with an average of S = (20 ± 5) $10^3 \cdot \mu C \cdot Gy^{-1} \cdot cm^{-2}$ for anisole, compared to the toluene samples average sensitivity of S = (15 ± 5) $10^3 \cdot \mu C \cdot Gy^{-1} \cdot cm^{-2}$; this trend remains valid even after normalization, with similar values between solvents. The results obtained are in line with the literature, with sensitivities of comparable magnitude to the ones found by Basiricò et al.[20] when using toluene as a solvent (with a reported maximal sensitivity of S = 45 · $10^3$ $\mu C \cdot Gy^{-1} \cdot cm^{-2}$).

The following table details the results obtained for all working samples compared in this chapter:

| Batch | Solvent employed | Sheet Resistance (Ω/sq) | Sensitivity ($\frac{\mu C}{cm^2 Gy} 10^3$) | Normalized Sensitivity (a. u.) |
|---|---|---|---|---|
| OD02 | Toluene | (7.8 ± 0.2) $10^{10}$ | (12.0 ± 0.2) | (0.94 ± 0.04) $10^{15}$ |
| | Toluene | (12.8 ± 0.4) $10^{10}$ | (8.5 ± 0.3) | (1.09 ± 0.07) $10^{15}$ |
| | Toluene | (6.00 ± 0.07) $10^{11}$ | (31 ± 8) | (18.6 ± 0.7) $10^{15}$ |
| | Toluene | (10.4 ± 0.4) $10^{10}$ | (9.4 ± 0.2) | (0.98 ± 0.05) $10^{15}$ |
| OD01 | Anisole | (1.94 ± 0.08) $10^{11}$ | (12.0 ± 0.2) | (2.33 ± 0.14) $10^{15}$ |
| | Anisole | (2.50 ± 0.06) $10^{11}$ | (18.3 ± 0.4) | (4.6 ± 0.2) $10^{15}$ |
| | Anisole | (9.4 ± 0.2) $10^{10}$ | (9.70 ± 0.10) | (0.91 ± 0.03) $10^{15}$ |
| | Anisole | (6.82 ± 0.11) $10^{10}$ | (9.9 ± 0.3) | (0.68 ± 0.03) $10^{15}$ |
| | Anisole | (2.16 ± 0.06) $10^{11}$ | (29 ± 2) | (6.3 ± 0.6) $10^{15}$ |
| | Anisole | (9.0 ± 0.4) $10^{10}$ | (41 ± 3) | (3.7 ± 0.4) $10^{15}$ |

Tab. 5: Summary table of the main parameters for all working samples considered in the solvent analysis.

### 4.2.2. Radiation Hardness

Electrical characterization measurements have been performed in dark conditions before and after a full cycle of X-ray measures to test the deterioration of the detector due to radiation exposure. The amount of radiation received by every detector corresponds to (3.73 ± 0.14) Gy.

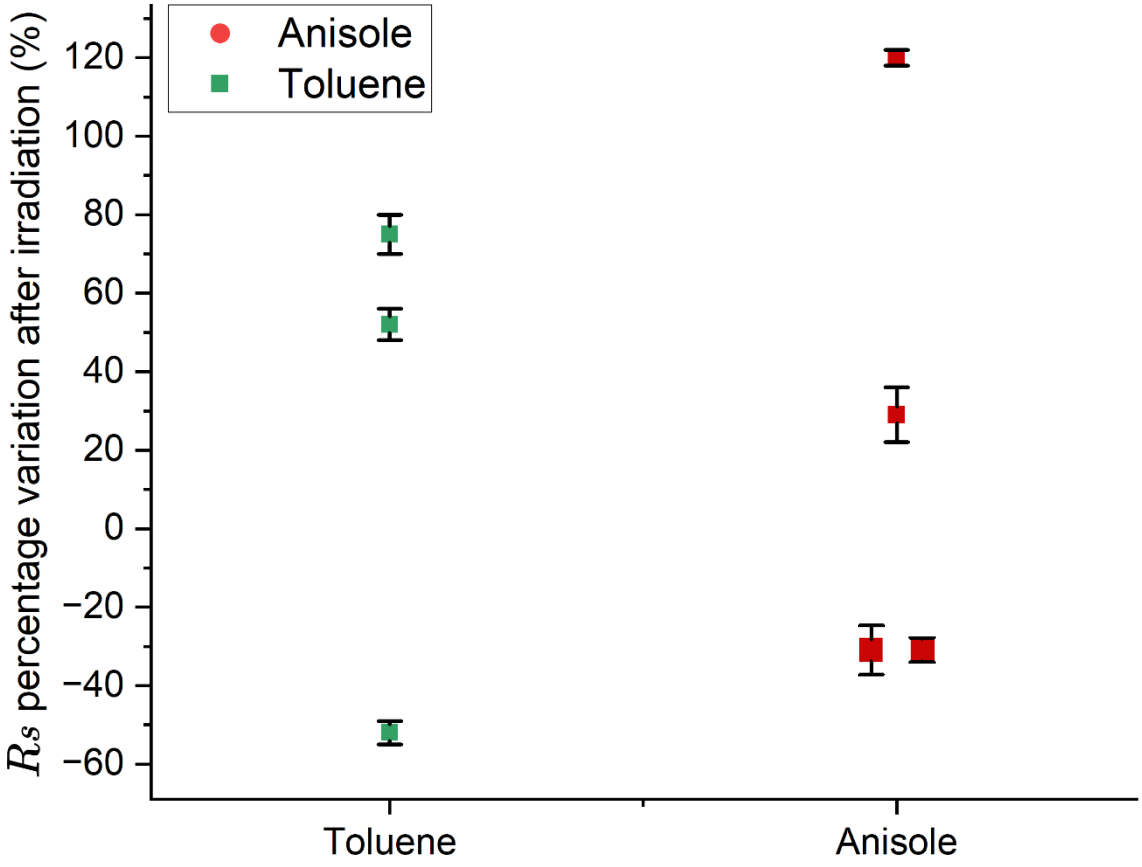


Fig. 25: Sheet resistance percentage variation of toluene and anisole processed samples after a cycle of irradiation under X-Ray of dose (3.73 ± 0.14) Gy.

As can be seen in Fig.25, the sheet resistance variation after irradiation for the samples presented doesn't display a clear variational trend. The anisole samples displayed a slightly higher variational range, spanning from -30% to 120% after irradiation, compared to the toluene values of -50% to 75%.

## 4.3 Influence of the Electrode Material on Detectors Performance

Of equal importance during this study has been the exploration of possible tissue equivalent alternatives for the sample's electrodes. The aim is to assess whether PEDOT electrodes could perform under irradiation as reliably as gold electrodes. Batches OD02 and OD04, will be discussed in the following, with particular attention towards the results obtained for samples with PEDOT: PSS electrode fingers.

### 4.3.1. X-Ray characterization of toluene-processed devices

In Fig. 26a below the dynamic curve at a fixed dose rose for a sample fabricated with PEDOT: PSS fingers (taken as example) is compared with the one of the gold electrodes devices discussed in the previous section, while both detectors were kept at a 1V bias. For these batches, toluene is the solvent used for the processing of TIPS-pentacene in the initial fabrication stage.

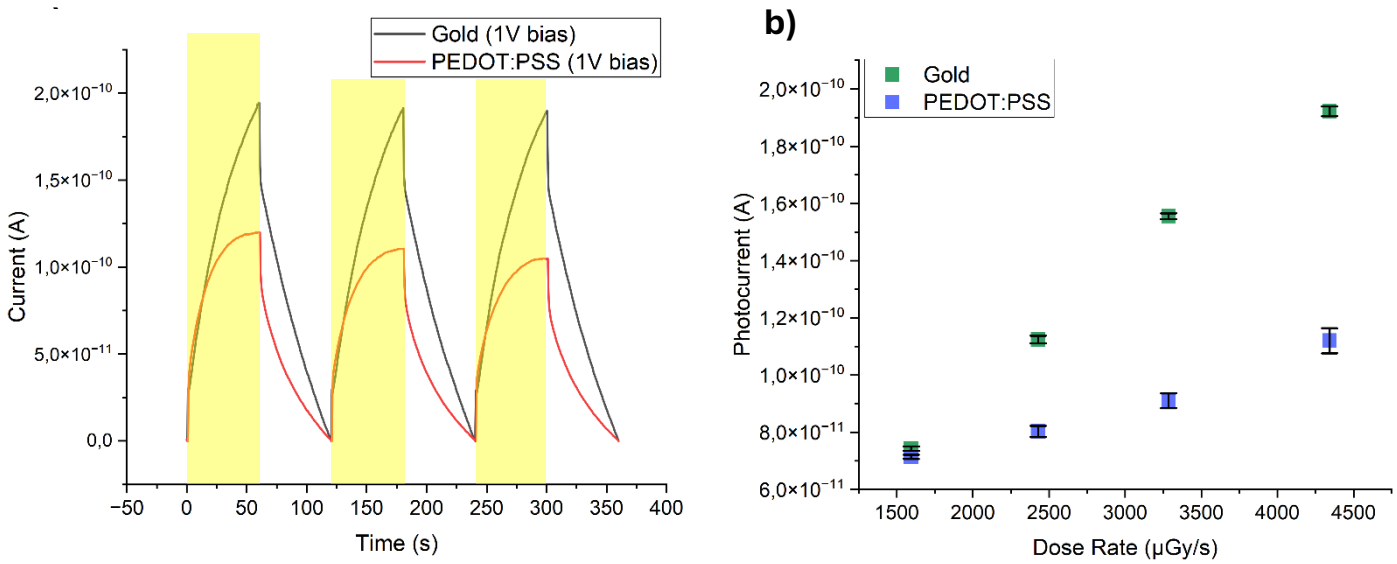


Fig. 26: a) Dynamic curves taken at a dose rates of (4.34 ± 0.17) mGy/s for gold electrodes and PEDOT:PSS electrodes samples fabricated using a toluene based solution. The areas marked in yellow correspond to the periods of irradiation. b) Photocurrent over dose rate plot of both devices.

Similarly to what has been said in the previous chapter, PEDOT:PSS devices also display the typical saw-tooth shape in the current, due to the photoconductive gain effect. The linear relation between photocurrent and dose rate for the PEDOT:PSS sample is displayed in Fig. 26b. Following what was done in section 4.2.1, sensitivity values of the analysed samples (all kept at a bias of 1V), both before and after normalization, are displayed in graph 27 through box charts. The darker squares, as mentioned earlier, correspond to the mean values.

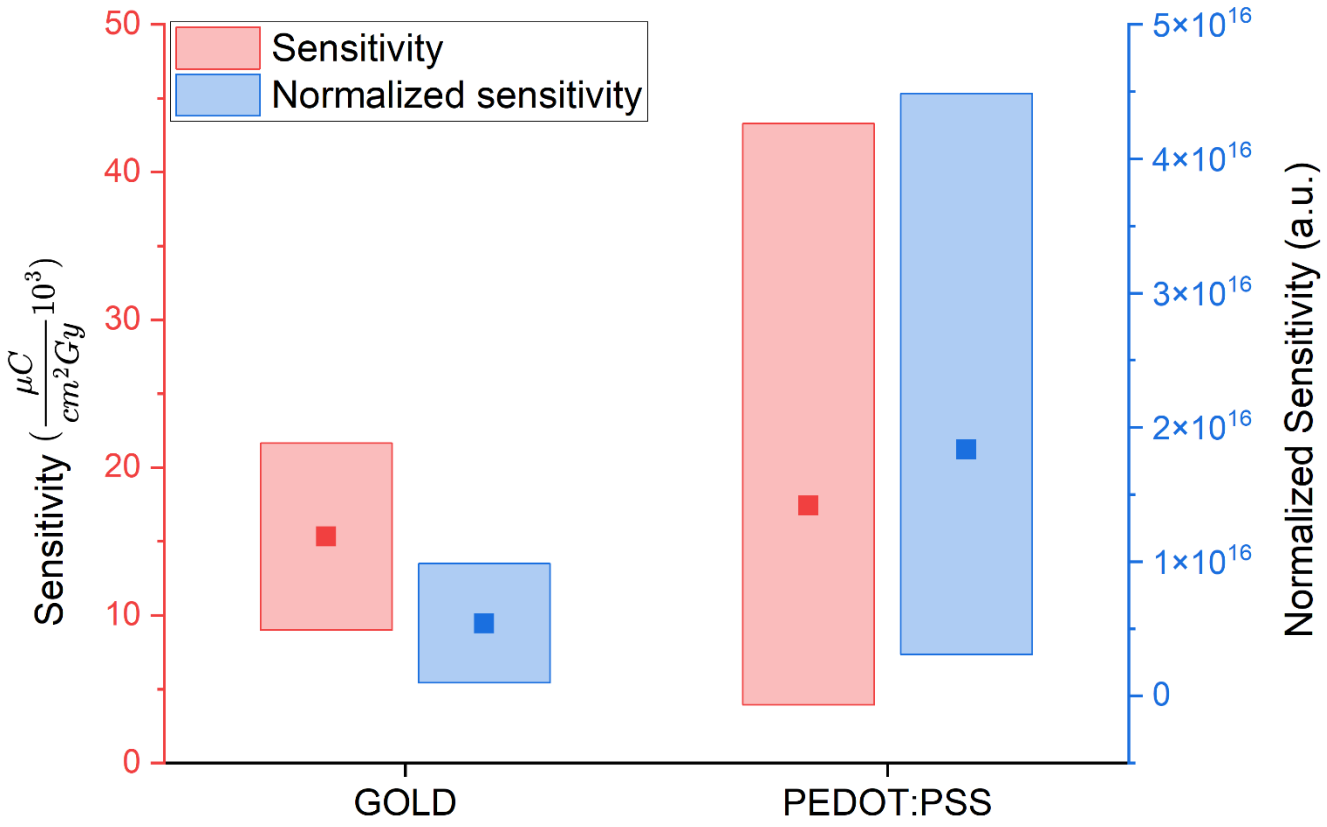


Fig. 27: Gold and PEDOT: PSS sensitivity comparison chart: both standard (red) and normalized for the sample's sheet resistance (blue) sensitivities are displayed. Averages are indicated by darker squares in each box.

The average sensitivity for PEDOT: PSS samples is comparable in magnitude ($S = (17 \pm 7)\ 10^3 \cdot \mu C \cdot Gy^{-1} \cdot cm^{-2}$) to the gold one ($S = (15 \pm 5)\ 10^3 \cdot \mu C \cdot Gy^{-1} \cdot cm^{-2}$). As can be seen, the spread of the PEDOT:PSS samples sensitivity values are much greater than the gold samples ones, resulting in a greater error of the mean. This is caused by one of the devices displaying a

sensitivity of (43 ± 19) $10^3 \cdot \mu C \cdot Gy^{-1} \cdot cm^{-2}$, almost 10 times greater than the other PEDOT:PSS values. Further study should thus be dedicated to improving uniformity of results for PEDOT:PSS samples.

Below a table detailing the main values obtained for the samples discussed in this chapter is displayed:

| Batch | Electrode material | Sheet Resistance (Ω/sq) | Sensitivity $(\frac{\mu C}{cm^2 Gy} 10^3)$ | Normalized Sensitivity (a. u.) |
|---|---|---|---|---|
| OD04 | PEDOT:PSS | (7.2 ± 0.2) $10^{10}$ | (43 ± 19) | (3.1 ± 1.5) $10^{15}$ |
| | PEDOT:PSS | (11.50 ± 0.08) $10^{12}$ | (3.90 ± 0.11) | (44.9 ± 1.6) $10^{15}$ |
| | PEDOT:PSS | (14.0 ± 0.2) $10^{11}$ | (5.0 ± 0.6) | (7.0 ± 0.9) $10^{15}$ |
| OD02 | Gold | (7.8 ± 0.2) $10^{10}$ | (12.0 ± 0.2) | (0.94 ± 0.04) $10^{15}$ |
| | Gold | (12.8 ± 0.4) $10^{10}$ | (8.5 ± 0.3) | (1.09 ± 0.07) $10^{15}$ |
| | Gold | (6.00 ± 0.07) $10^{11}$ | (31 ± 8) | (18.6 ± 0.7) $10^{15}$ |
| | Gold | (10.4 ± 0.4) $10^{10}$ | (9.4 ± 0.2) | (0.98 ± 0.05) $10^{15}$ |

Tab. 6: Summary table of the main parameters for all working samples considered in the electrodes analysis.

### 4.3.2. Radiation Hardness

Similarly to what was done in section 4.2.2., in the following the variation in electrical characteristics of the studied samples immediately after irradiation will be discussed: Fig. 28

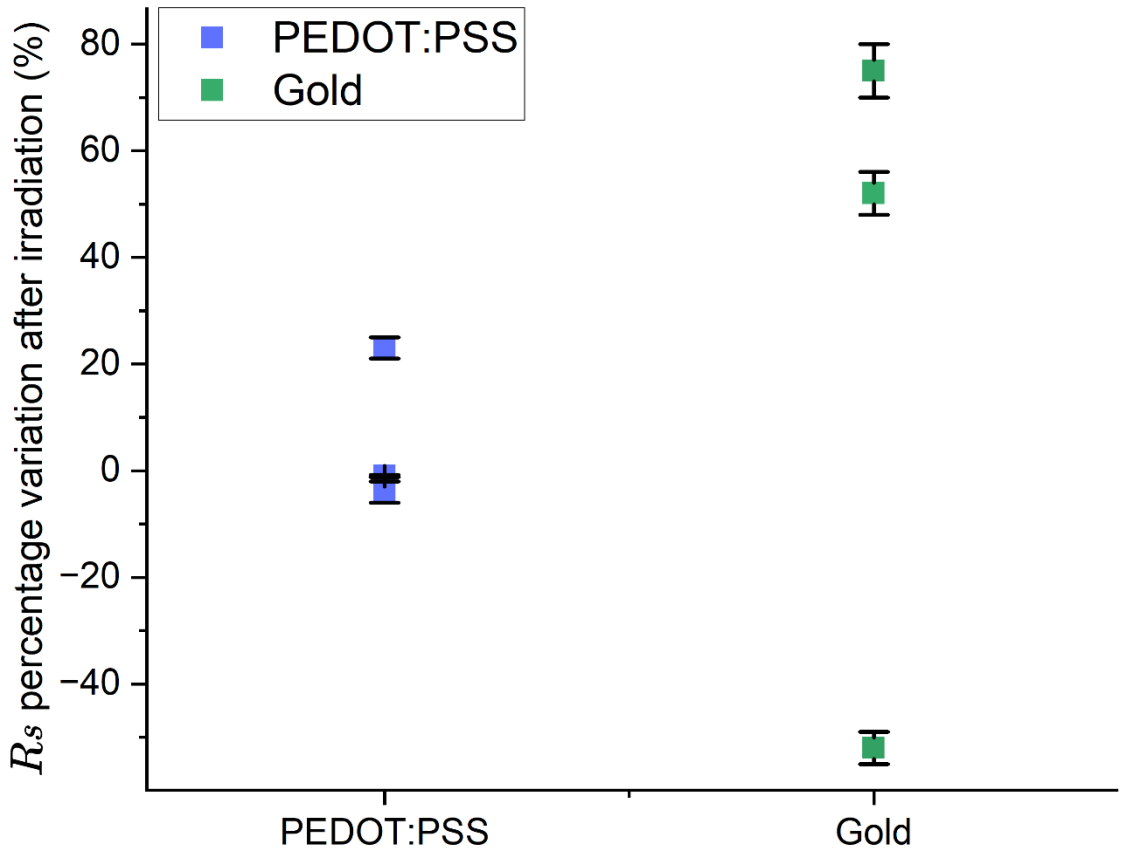


Fig. 28: Sheet resistance percentage variation of Gold and PEDOT:PSS samples after a cycle of irradiation under X-Ray amounting to to (3.73 ± 0.14) Gy.

details the sheet resistance percentage variation for all devices of each type. The amount of radiation received by every detector corresponded to (3.73 ± 0.14) Gy.

The variation in sheet resistance for all samples is lower than 100% and, as noted before, doesn't follow a particular trend. The highest variation measured for the PEDOT:PSS electrodes devices is 31%, indicating a particularly high resistance of these detectors to radiation, probably due to the low-Z nature (and thus lower X-ray absorption) of the polymer when compared to gold.

### 4.3.3. X-ray characterization of anisole-processed devices

Having achieved excellent results in the previous studies, batch OD03 has been fabricated to test the capabilities of green processed, fully organic devices: these samples combine the tissue equivalence of PEDOT:PSS electrodes devices to the more sustainable fabrication coming from anisole solution processing. When tested under X-ray, these devices display an inverted signal, as shown in Fig. 29. This might be the result of unwanted defective states which boost charge recombination under X-ray, thus quenching the expected response. Further study is needed to better understand the origin of this phenomenon.

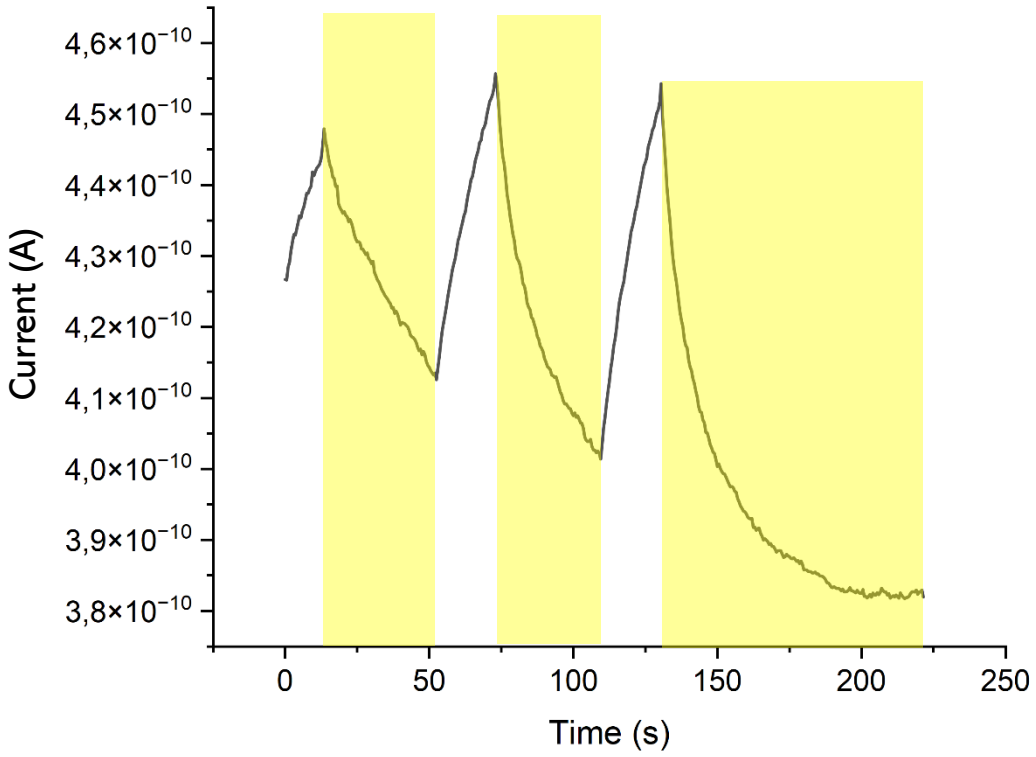


Fig. 29: Dynamic curve of a sample from batch OD03. The yellow areas correspond to periods of X-ray irradiation. As is clearly visible, the current response is not in line with the expected theoretical one, indicating internal effects that modify the behaviour.

### 4.3.4. UV characterization of anisole-processed devices

Due to the inverted response under X-ray irradiation, to assess its performance, batch OD03 has been tested under UV light. To have a proper comparison, the anisole-fabricated samples with gold electrodes (batch OD01) are also tested in the same way. The measurements are performed using a 385 nm high-intensity LED, kept at a (4.80 ± 0.10) cm distance from the samples.

In Fig. 30, as done for X-ray measurements, both the dynamic curves and the corresponding responsivity fits are shown.

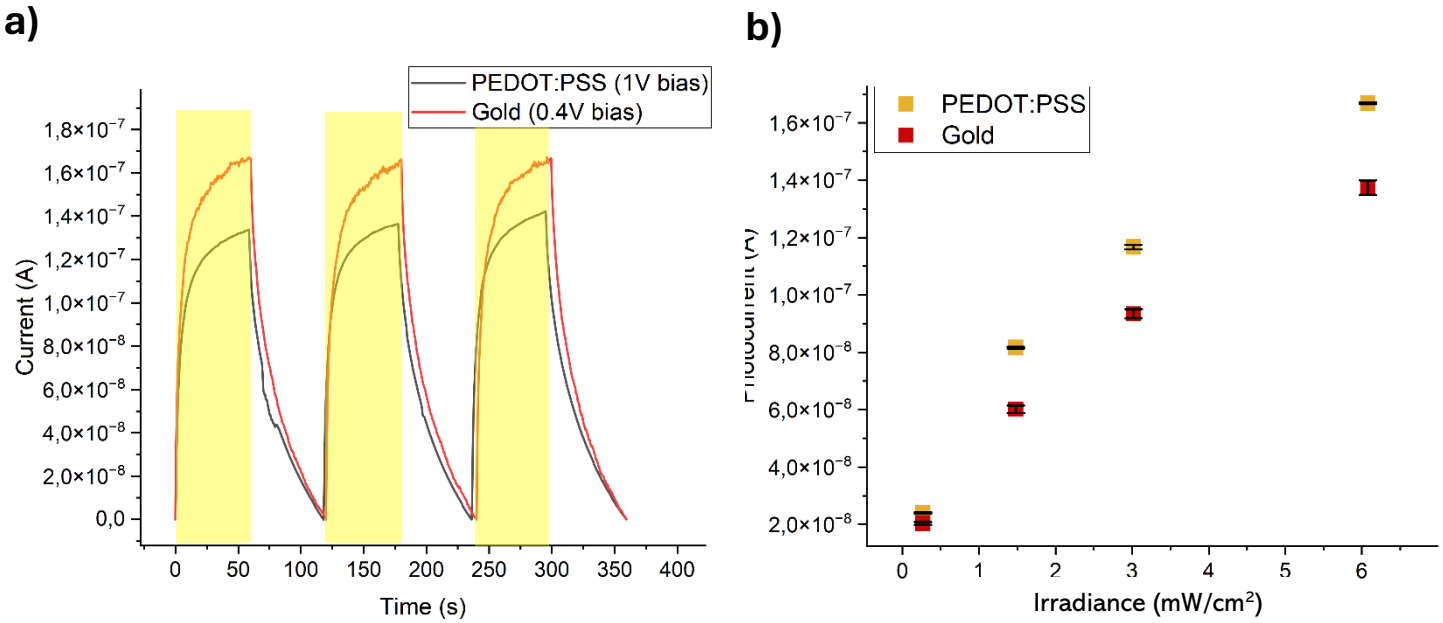


Fig. 30: a) Dynamic curves taken at a fixed irradiance of (6.1 ± 0.3) mW/cm$^2$ for gold electrodes and PEDOT:PSS electrodes samples fabricated using an anisole based solution. The areas marked in yellow correspond to the periods of irradiation. b) Photocurrent over dose rate plot of both devices.

The responsivities of four devices per batch are displayed below in Fig. 31, where, for both gold and PEDOT:PSS samples, the responsivity is plotted together with the corresponding normalized value, as previously done for the X-ray measurements. These devices were also kept at different biases to ensure comparable dark currents, with Voltage values ranging from 0.1 to 1 Volts.

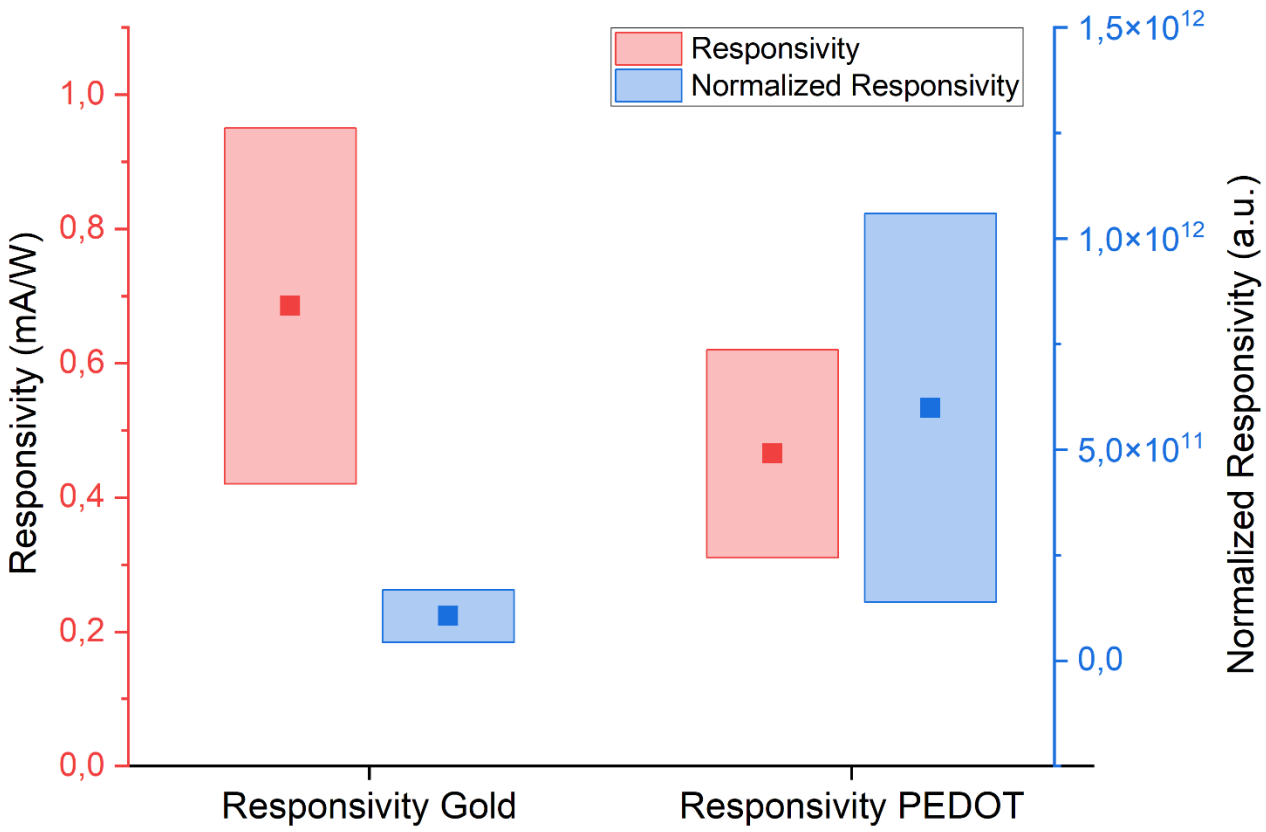


Fig. 31: Gold and PEDOT: PSS responsivity comparison chart: both standard (red) and normalized for the sample's sheet resistance (blue) responsivities are displayed. Averages are indicated by darker squares in each box.

Similarly to the comparison of the X-ray sensitivity of gold and PEDOT: PSS devices fabricated using toluene as solvent, the PEDOT: PSS electrodes slightly affect the responsivity under UV light as well, resulting in decreased responsivities values (we see a decrease of almost 30%, from $R_{gold}$ = (0.69 ± 0.02) mA/W for the gold average to $R_{PEDOT}$ = (0.47 ± 0.01) mA/W for the PEDOT: PSS one). However, once normalized to account for transport effects, the PEDOT:PSS devices exhibit a slightly higher responsivity, with values of $R_{gold}$ = (1.1 ± 0.4) $10^{11}$ for the gold average and $R_{PEDOT}$ = (6 ± 3) $10^{11}$ for the PEDOT: PSS one, indicating that the lower response was due to transport limitations. When comparing the obtained result with newly developed devices[75] (with reported responsivities of 0.4 mA/W), these samples display comparable results.

Table 6 below summarizes the sheet resistance and responsivity of all the samples analysed under UV:

| Batch | Electrode material | Sheet Resistance (Ω/sq) | Responsivity $(\frac{mA}{W})$ | Normalized Responsivity (a.u.) |
|---|---|---|---|---|
| OD01 | Gold | (19.4 ± 0.8) $10^{10}$ | (1.00 ± 0.10) | (1.94 ± 0.09) $10^{11}$ |
| | Gold | (2.46 ± 0.06) $10^{11}$ | (5.7 ± 0.8) $10^{-1}$ | (1.4 ± 0.2) $10^{11}$ |
| | Gold | (9.40 ± 0.10) $10^{10}$ | (2.7 ± 0.3) $10^{-1}$ | (2.4 ± 0.3) $10^{10}$ |
| | Gold | (6.8 ± 0.2) $10^{10}$ | (9.0 ± 1.0) $10^{-1}$ | (6.1 ± 0.9) $10^{10}$ |
| OD03 | PEDOT | (4.8 ± 0.2) $10^{11}$ | (4.8 ± 0.5) $10^{-1}$ | (2.3 ± 0.3) $10^{11}$ |
| | PEDOT | (14.2 ± 0.6) $10^{11}$ | (6.0 ± 1.0) $10^{-1}$ | (8.5 ± 1.8) $10^{11}$ |
| | PEDOT | (19.8 ± 0.6) $10^{11}$ | (6.4 ± 0.5) $10^{-1}$ | (12.67 ± 0.14) $10^{11}$ |
| | PEDOT | (3.2 ± 0.10) $10^{10}$ | (1.4 ± 0.3) $10^{-1}$ | (4.5 ± 1.1) $10^{10}$ |

Tab. 6: Summary table of the main parameters for all working samples considered in the UV response analysis.

Further testing of these samples' response under X-ray is needed, but the results obtained in this work already offer a first promising look at the possible development of high sensitivity, green processed fully organic detectors.

# *Conclusions*

In this work two parallel studies were conducted: one explored the use of anisole, an environmentally friendly, non-toxic solvent, for the processing of organic semiconductor solutions. The second focused on the use of the organic conductive polymer PEDOT:PSS as a tissue-equivalent alternative to gold in the fabrication of the detector's electrodes. the electrical and photodetection performances of green-processed, fully tissue equivalent detectors were investigated by combining in the same devices the previous two studies.

The use of a green alternative to the toxic solvent commonly employed in device fabrication did not alter the crystallization quality of the detectors, displaying good uniformity under morphological analysis and excellent charge transport properties through electrical characterizations. The subsequent sensitivity measurements further corroborated this positive result, with the sensitivity of anisole-processed devices ($S= (20 \pm 5)\ 10^3 \cdot \mu C \cdot Gy^{-1} \cdot cm^{-2}$), compatible with the toluene-processed one ($S= (15 \pm 5)\ 10^3 \cdot \mu C \cdot Gy^{-1} \cdot cm^{-2}$).

At the same time, the employment of PEDOT:PSS as a tissue equivalent alternative to gold as electrode material proved successful, with sensitivity values of PEDOT:PSS devices ($S = (17 \pm 7)\ 10^3 \cdot \mu C \cdot Gy^{-1} \cdot cm^{-2}$) comparable to the gold electrodes ones ($S = (15 \pm 5)\ 10^3 \cdot \mu C \cdot Gy^{-1} \cdot cm^{-2}$).

An aging study, performed over the span of two months, demonstrated the good stability of anisole processed devices. A higher degradation was observed in a parallel aging study performed on PEDOT:PSS samples, with sheet resistance values increasing of one order of magnitude. This result was in line with the expected value based on the literature.

Finally, PEDOT:PSS electrodes devices fabricated using anisole as solvent were tested to evaluate the performances of fully tissue equivalent green processed devices. A photoresponsivity comparison study between these samples ($R_{PEDOT}$ = (0.47 ± 0.01) mA/W) and anisole processed, gold electrodes devices ($R_{gold}$ = (0.69 ± 0.02) mA/W) demonstrated high comparability, with responsivities in line with the recent literature.

This study, introducing novel green processed, tissue equivalent devices for the detection of X-ray, lays the foundations for future developments in the field of radiation detection. Further research might tackle the issues encountered in this study, such as low reproducibility of PEDOT:PSS samples, while also aiming at higher detection performances.

# *Appendix A*

Donghil et al.[42] reported an optimal concentration of 8 mg/mL for an anisole based TIPS-Pentacene solution. This conclusion was achieved by electrically characterizing OTFT devices fabricated using various solvents at different concentrations. This measure only accounted for the electrical mobility of the devices, used to pinpoint the best concentration value. Thus, as an additional study on the topic, a batch of 15 devices was fabricated during this work, 3 devices for each of the 5 concentration values we wanted to assess. The concentrations were 1, 2, 4, 6 and 8 mg/mL. The samples were first analysed with an optical microscope: the samples of concentrations 1, 2 and 4 mg/mL showed limited crystallisation, with subsequent IV measurements displaying an open circuit behaviour. Better responses were obtained at higher concentrations: in Fig. 32 it is possible to see the reported the excellent crystallization at 6 and 8 mg/mL, with longer crystals and extended surface coating, while Tab. 7 contains an overview of the measured sheet resistances. The average sheet resistance of the 8 mg/mL samples ($R_S(8) = (3.7 \pm 0.5)\ 10^{11}$) was higher than the 6 mg/mL one ($R_S(8) = (1.6 \pm 0.4)\ 10^{11}$), indicating better conductivity at the lower concentration. The electrical and X-ray responses thus improved at the lower concentration, with two of the 6 mg/mL samples working as expected as reported in chapter 4. The 8 mg/mL samples, possibly due to an excessive charge trapping, didn't display the expected current behaviour under irradiation. Because of the better results achieved, a concentration of 6 mg/mL was adopted in the subsequent fabrication of anisole-based solutions.

**a)**

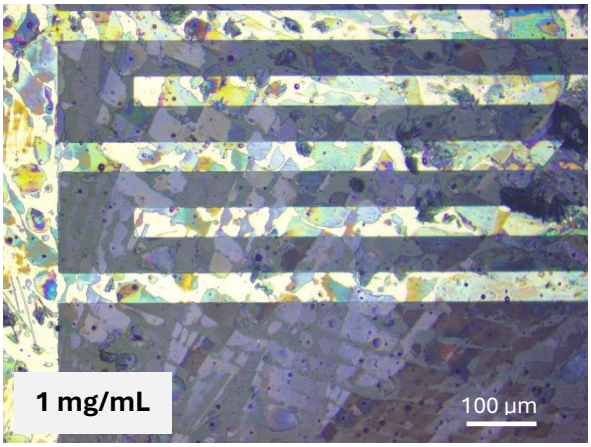


**b)**

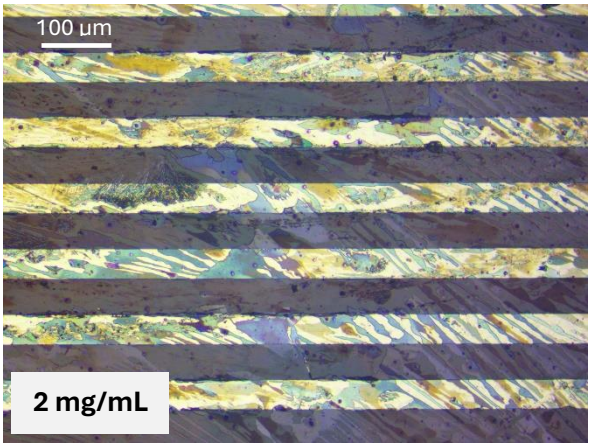

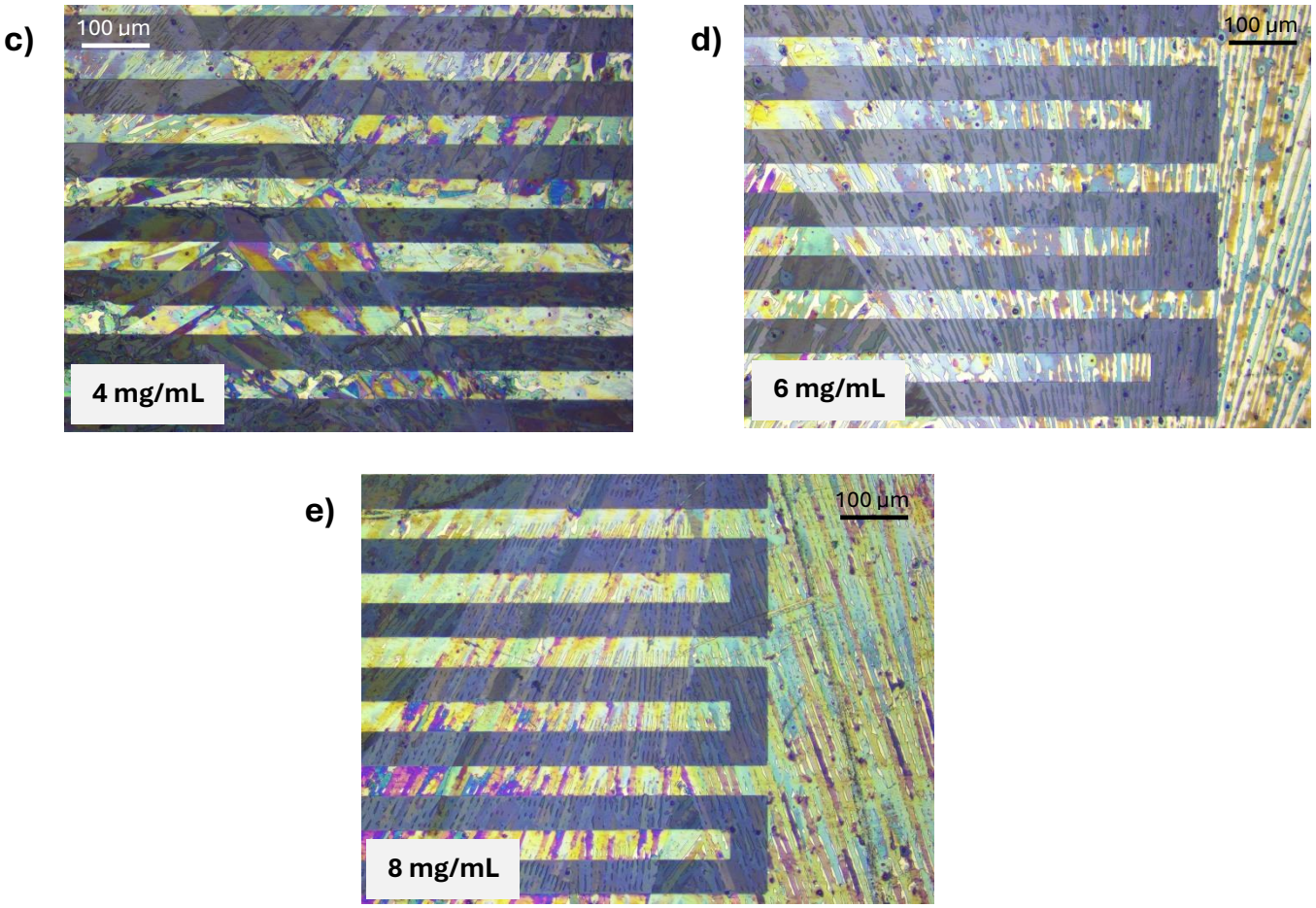


Fig. 32: Optical microscope images of TIPS-Pentacene crystals deposited at different concentrations of toluene-based solution: a) 1 mg/mL b) 2 mg/mL c) 4 mg/mL d) 6 mg/mL e) 8 mg/mL.

| Sample's concentration (mg/mL) | Sheet resistance (Ω/sq) |
|---|---|
| 6 | $(2.21 \pm 0.08)\ 10^{11}$ |
| 6 | $(9.0 \pm 0.4)\ 10^{10}$ |
| 6 | $(1.61 \pm 0.04)\ 10^{11}$ |
| 8 | $(2.90 \pm 0.08)\ 10^{11}$ |
| 8 | $(3.52 \pm 0.06)\ 10^{11}$ |
| 8 | $(4.59 \pm 0.07)\ 10^{11}$ |

Tab. 7: Sheet resistances of the 6 and 8 mg/mL samples.

# *Appendix B*

In the following, all additional detail regarding the electrical characterization of the devices under yellow light or in dark conditions is presented, starting from a series of plots containing all IVs of each type of working device under study in this work.

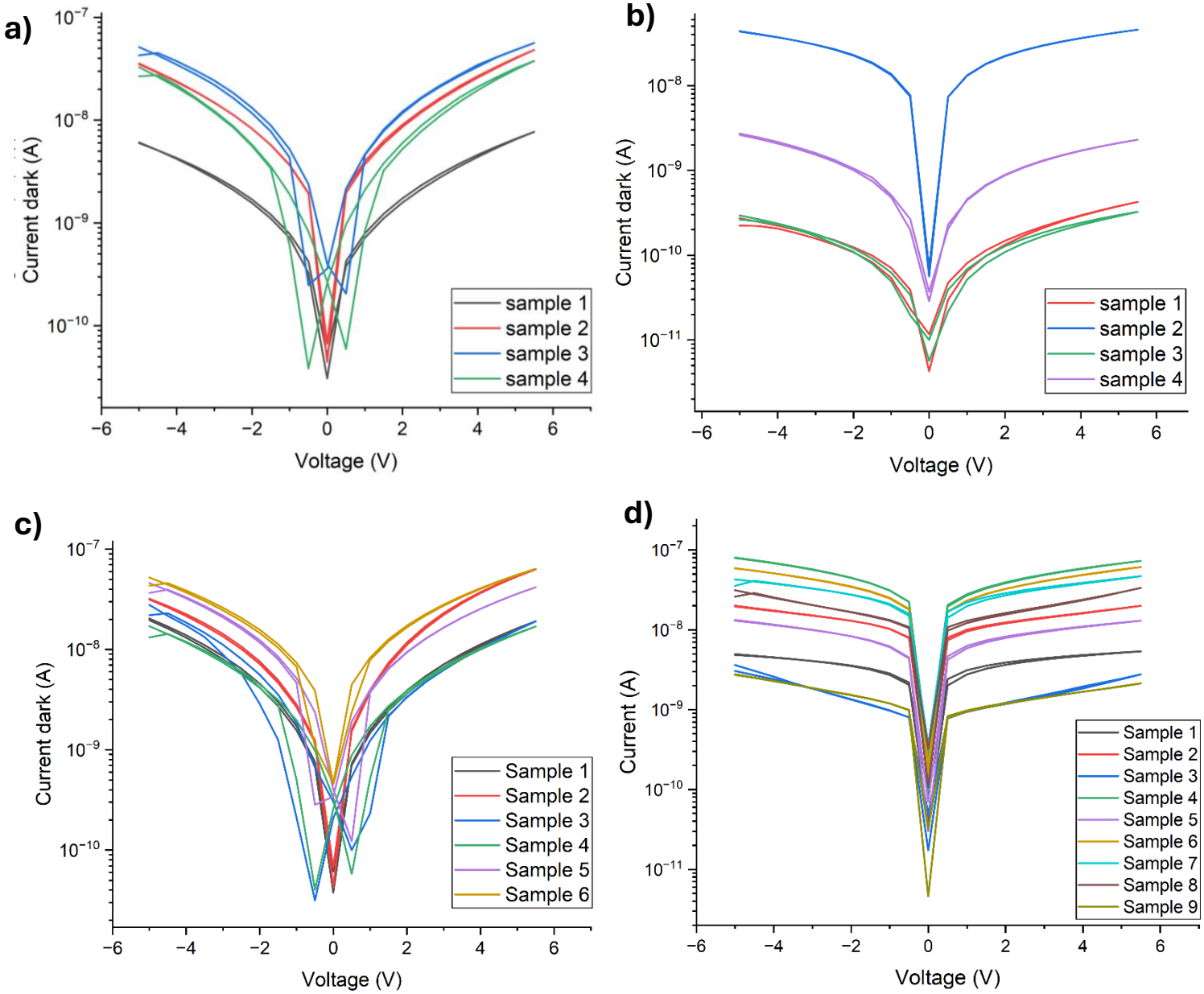


Fig. 34: IV curves taken between -5 and 5 V for each type of sample. Namely: a ) gold fingers and Toluene solution, b) PEDOT:PSS fingers and Toluene solution, c) gold fingers and Anisole solution, d) PEDOT:PSS fingers and Anisole solution.

The sheet resistance variation over 2 months of a sample from each type of device is presented in figure 34, with the corresponding IV measurements.

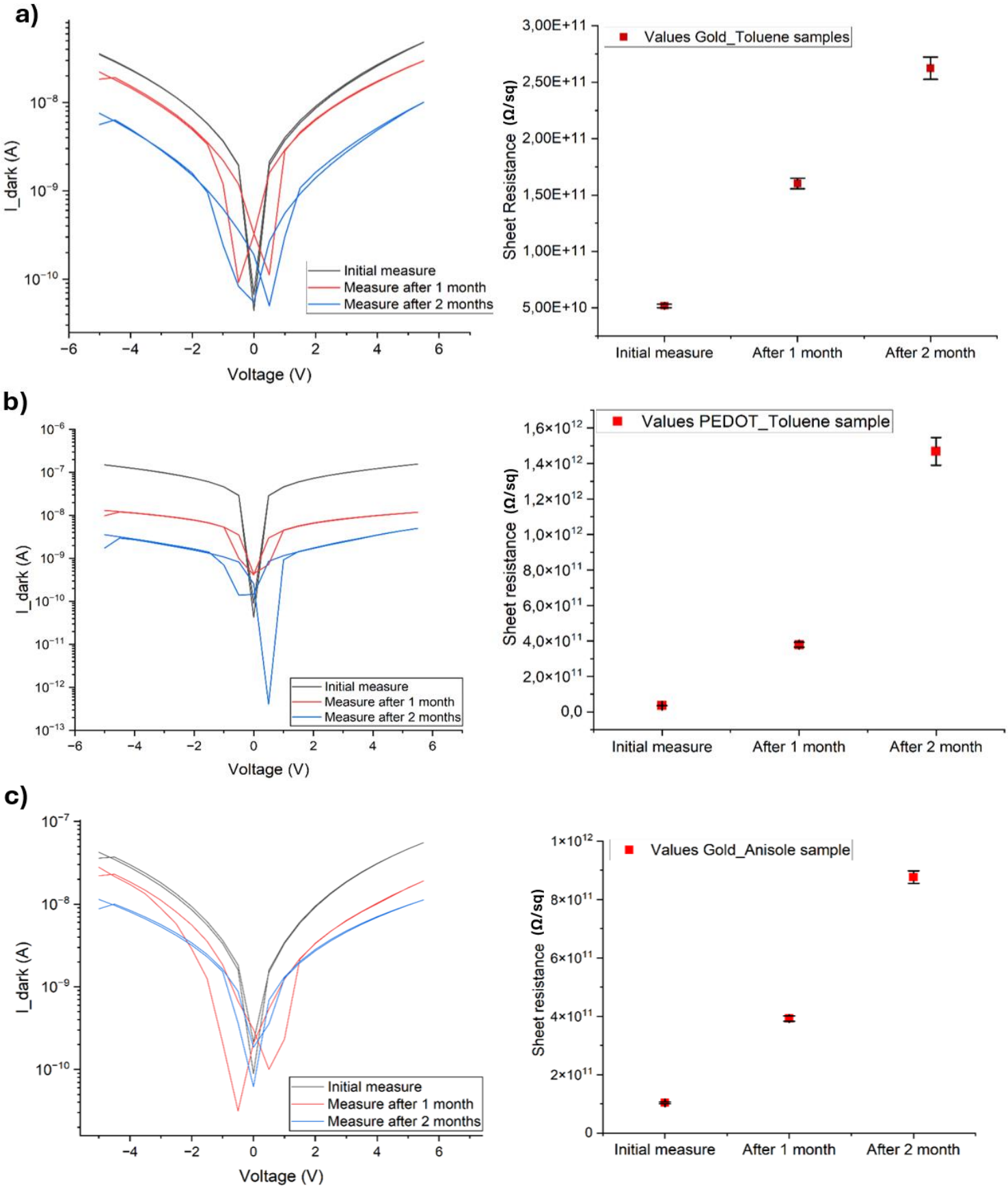

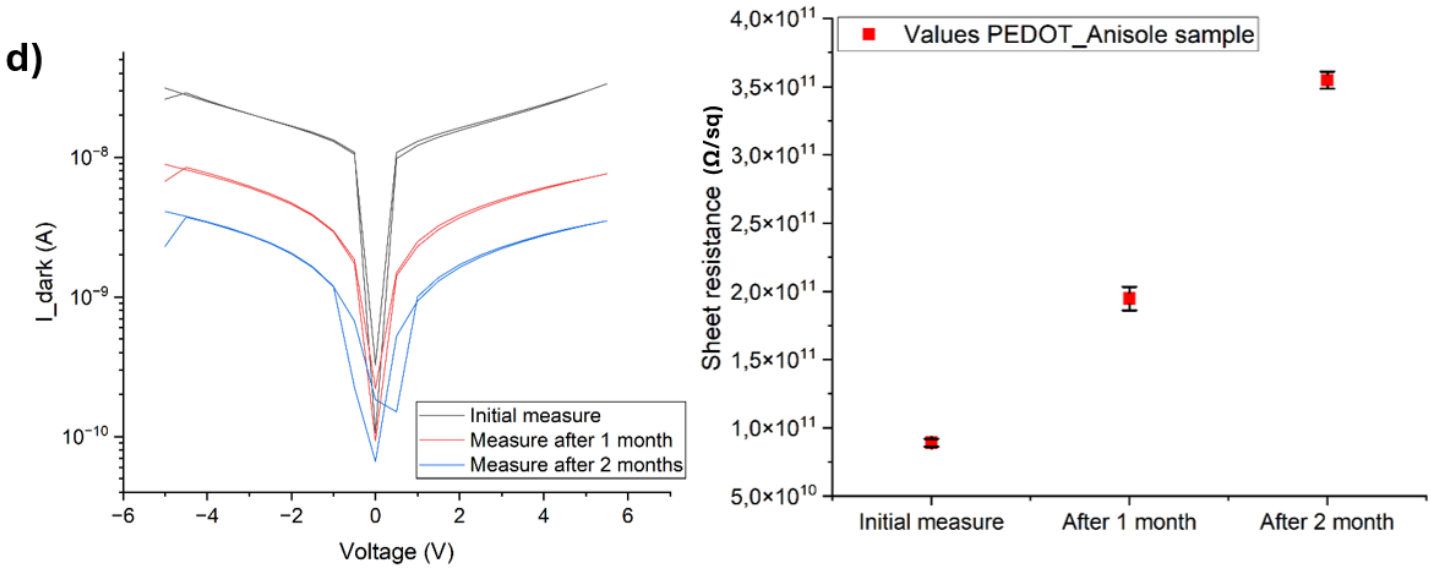


Fig. 35: IV (left) and sheet resistance (right) variation of samples over time, from top to bottom: a) gold fingers and Toluene solution, b) PEDOT:PSS fingers and Toluene solution, c) gold fingers and Anisole solution, d) PEDOT:PSS fingers and Anisole solution.

In section 4.1.3. the sheet resistance variation after X-ray irradiation for all types of samples studied has been presented through percentage variation's averages. In fig.36 and 37 a more detailed look at the variations of single samples is presented. In all the graphs reported below, the sheet resistance values before and after irradiation for each sample are displayed with the same colour and shape.

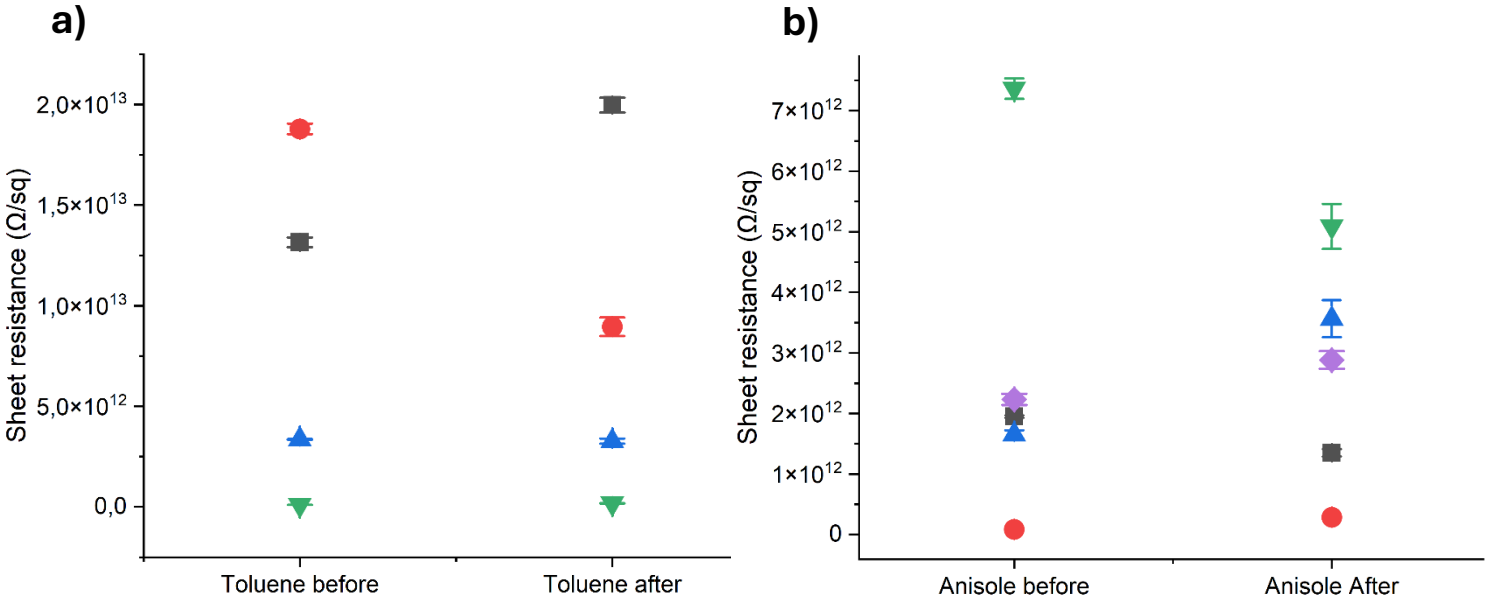


Fig. 36: Sheet resistance before and after irradiation of (a) Toluene processed devices with gold electrodes, (b) Anisole processed devices with gold electrodes.

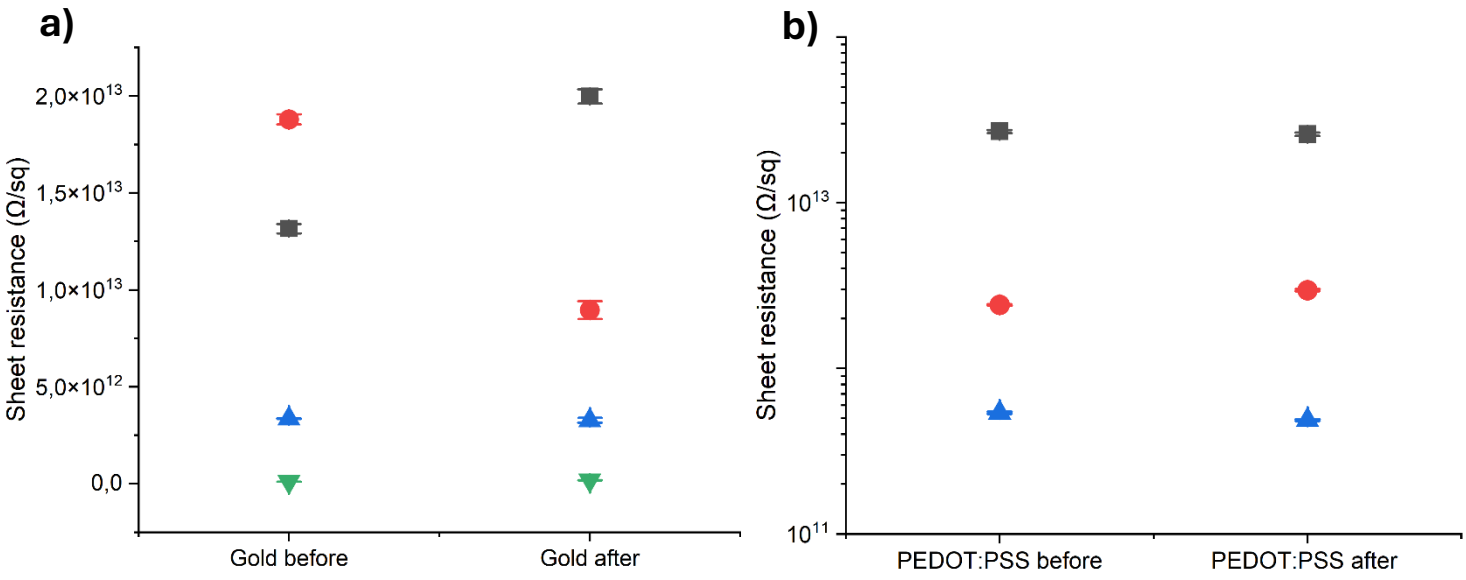


Fig. 37: Sheet resistance before and after irradiation of (a) Toluene processed devices with gold electrodes, (b) Toluene processed devices with PEDOT:PSS electrodes.

# *Appendix C*

The dynamic curves of samples from each type of device characterized in this study are displayed below for both the X-ray (Fig. 33) and UV (Fig. 34) measures.

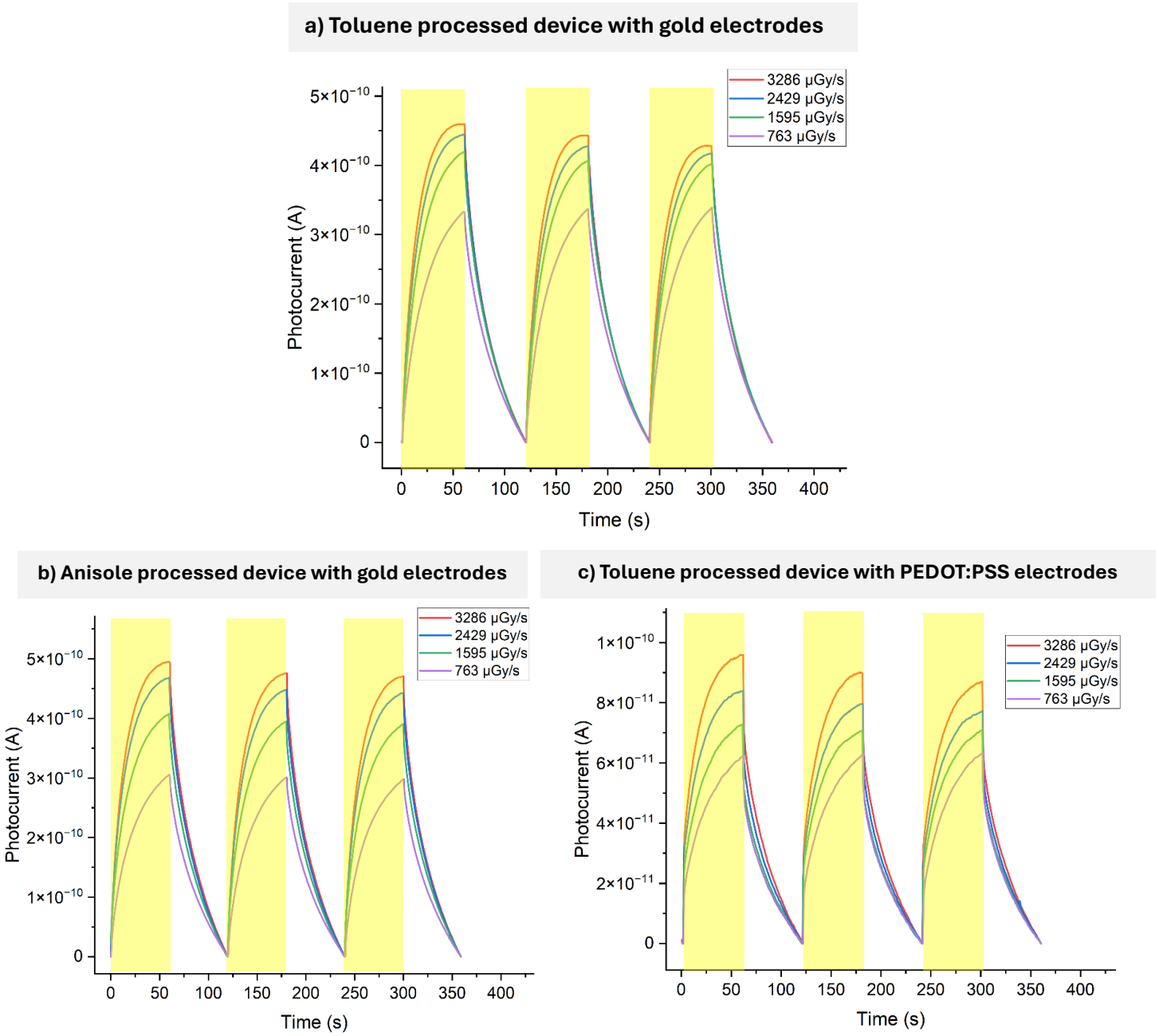


Fig. 32: Dynamic curves of a) Toluene processed device with gold electrodes, b) Anisole processed device with gold electrodes and c) Toluene processed device with PEDOT:PSS electrodes at four different dose rates. The areas in yellow correspond to periods of irradiation.

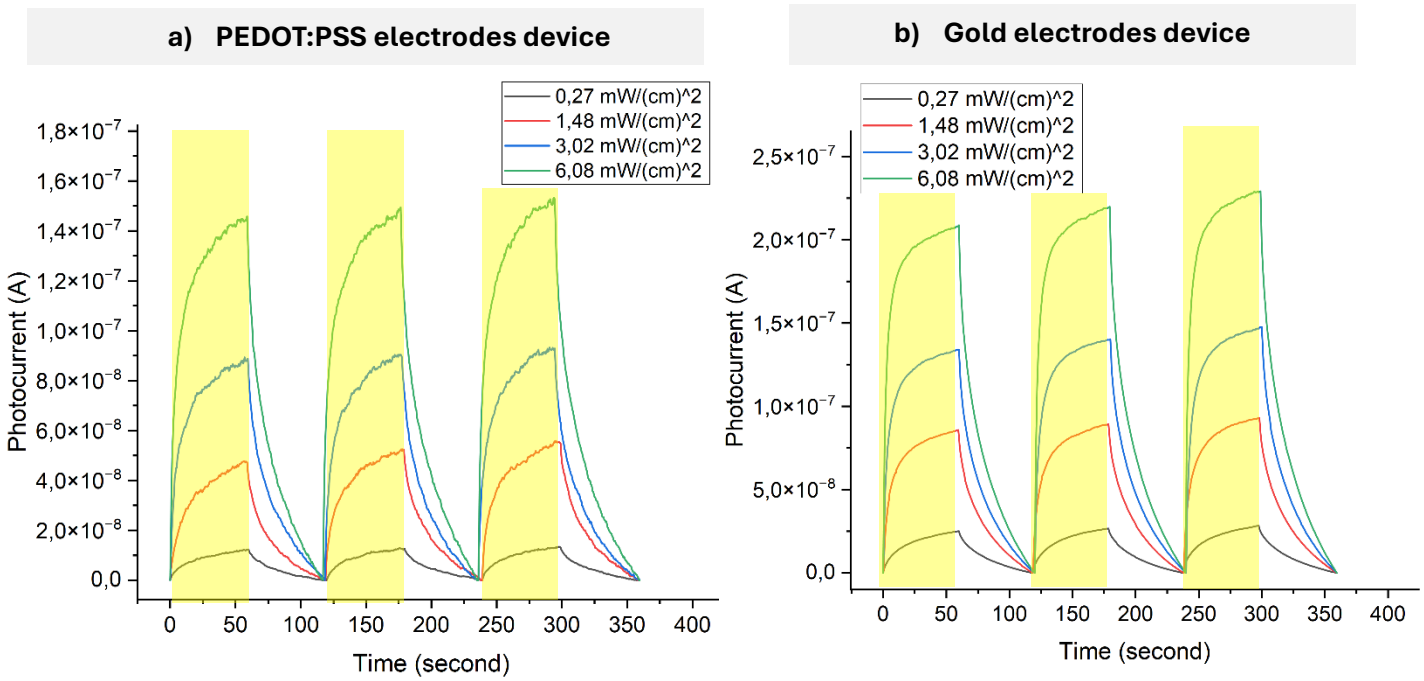


Fig. 33: Dynamic curves of an anisole processed device with a) PEDOT:PSS electrodes and b) gold electrodes, under UV light at 4 different irradiance values. The areas in yellow correspond to the intervals of irradiation.

# *References*


(1) Spahn, M. X-Ray Detectors in Medical Imaging. *Nucl. Instrum. Methods Phys. Res. Sect. Accel. Spectrometers Detect. Assoc. Equip.* **2013**, *731*, 57–63. https://doi.org/10.1016/j.nima.2013.05.174.

(2) Zeidell, A. M.; Ren, T.; Filston, D. S.; Iqbal, H. F.; Holland, E.; Bourland, J. D.; Anthony, J. E.; Jurchescu, O. D. Organic Field-Effect Transistors as Flexible, Tissue-Equivalent Radiation Dosimeters in Medical Applications. *Adv. Sci.* **2020**, *7* (18), 2001522. https://doi.org/10.1002/advs.202001522.

(3) Basiricò, L.; Ciavatti, A.; Fratelli, I.; Dreossi, D.; Tromba, G.; Lai, S.; Cosseddu, P.; Bonfiglio, A.; Mariotti, F.; Dalla Val, C.; Bellucci, V.; Anthony, J. E.; Fraboni, B. Medical Applications of Tissue-Equivalent, Organic-Based Flexible Direct X-Ray Detectors. *Front. Phys.* **2020**, *8*, 13. https://doi.org/10.3389/fphy.2020.00013.

(4) Michail, C.; Liaparinos, P.; Kalyvas, N.; Kandarakis, I.; Fountos, G.; Valais, I. Radiation Detectors and Sensors in Medical Imaging. *Sensors* **2024**, *24* (19), 6251. https://doi.org/10.3390/s24196251.

(5) Haff, R. P.; Toyofuku, N. X-Ray Detection of Defects and Contaminants in the Food Industry. *Sens. Instrum. Food Qual. Saf.* **2008**, *2* (4), 262–273. https://doi.org/10.1007/s11694-008-9059-8.

(6) Marguí, E.; Queralt, I.; De Almeida, E. X-Ray Fluorescence Spectrometry for Environmental Analysis: Basic Principles, Instrumentation, Applications and Recent Trends. *Chemosphere* **2022**, *303*, 135006. https://doi.org/10.1016/j.chemosphere.2022.135006.

(7) Ogino, N.; Arimoto, M.; Sawano, T.; Yonetoku, D.; Yu, P.; Watanabe, S.; Hiraga, J. S.; Yuhi, D.; Hatori, S.; Kume, K.; Hasegawa, T. Performance Verification of Next-Generation Si CMOS Soft X-Ray Detector for Space Applications. *Nucl. Instrum. Methods Phys. Res. Sect. Accel. Spectrometers Detect. Assoc. Equip.* **2021**, *987*, 164843. https://doi.org/10.1016/j.nima.2020.164843.

(8) Karmakar, A.; Wang, J.; Prinzie, J.; De Smedt, V.; Leroux, P. A Review of Semiconductor Based Ionising Radiation Sensors Used in Harsh Radiation Environments and Their Applications. *Radiation* **2021**, *1* (3), 194–217. https://doi.org/10.3390/radiation1030018.

(9) Sun, L.; Fukuda, K.; Someya, T. Recent Progress in Solution-Processed Flexible Organic Photovoltaics. *Npj Flex. Electron.* **2022**, *6* (1), 89. https://doi.org/10.1038/s41528-022-00222-3.

(10) Basiricò, L.; Ciavatti, A.; Fraboni, B. Solution-Grown Organic and Perovskite X-Ray Detectors: A New Paradigm for the Direct Detection of Ionizing Radiation. *Adv. Mater. Technol.* **2021**, *6* (1), 2000475. https://doi.org/10.1002/admt.202000475.

(11) Campana, F.; Kim, C.; Marrocchi, A.; Vaccaro, L. Green Solvent-Processed Organic Electronic Devices. *J. Mater. Chem. C* **2020**, *8* (43), 15027–15047. https://doi.org/10.1039/D0TC03610B.

(12) Fratelli, I.; Basiricò, L.; Ciavatti, A.; Lamport, Z. A.; Anthony, J. E.; Kymissis, I.; Fraboni, B. Trap States Ruling Photoconductive Gain in Tissue-Equivalent, Printed Organic X-Ray Detectors. *Adv. Mater. Technol.* **2023**, *8* (3), 2200769. https://doi.org/10.1002/admt.202200769.

(13) Chen, S.; Liang, L.; Zhang, Y.; Lin, K.; Yang, M.; Zhu, L.; Yang, X.; Zang, L.; Lu, B. PEDOT:PSS-Based Electronic Materials: Preparation, Performance Tuning, Processing, Applications, and Future Prospect. *Prog. Polym. Sci.* **2025**, *166*, 101990. https://doi.org/10.1016/j.progpolymsci.2025.101990.

(14) Nenoi, M. *Evolution of Ionizing Radiation Research*; IntechOpen, 2015.

(15) Knoll, G. F. *Radiation Detection and Measurement*, 4th ed.; Wiley: Hoboken, NJ, 2010.

(16) Owens, A.; Peacock, A. Compound Semiconductor Radiation Detectors. *Nucl. Instrum. Methods Phys. Res. Sect. Accel. Spectrometers Detect. Assoc. Equip.* **2004**, *531* (1–2), 18–37. https://doi.org/10.1016/j.nima.2004.05.071.

(17) Zou, S.-J.; Shen, Y.; Xie, F.-M.; Chen, J.-D.; Li, Y.-Q.; Tang, J.-X. Recent Advances in Organic Light-Emitting Diodes: Toward Smart Lighting and Displays. *Mater. Chem. Front.* **2020**, *4* (3), 788–820. https://doi.org/10.1039/C9QM00716D.

(18) *Organic Semiconductors in Sensor Applications*; Bernards, D. A., Malliaras, G. G., Owens, R. M., Eds.; Materials Science; Springer Berlin Heidelberg: Berlin, Heidelberg, 2008; Vol. 107. https://doi.org/10.1007/978-3-540-76314-7.
(19) Diao, Y.; Shaw, L.; Bao, Z.; Mannsfeld, S. C. B. Morphology Control Strategies for Solution-Processed Organic Semiconductor Thin Films. *Energy Env. Sci* **2014**, *7* (7), 2145–2159. https://doi.org/10.1039/C4EE00688G.
(20) Basiricò, L.; Ciavatti, A.; Cramer, T.; Cosseddu, P.; Bonfiglio, A.; Fraboni, B. Direct X-Ray Photoconversion in Flexible Organic Thin Film Devices Operated below 1 V. *Nat. Commun.* **2016**, *7* (1), 13063. https://doi.org/10.1038/ncomms13063.
(21) Zheng, W.; Xu, L.; Wang, Y.; Liu, C.; Liang, L.; Qin, Z.; Lian, L.; Lei, Y.; Hu, Q.; Jie, W. High-Performance Direct Detection of α-Particle and X-Ray with Centimeter-Sized Organic BPEA Single Crystals. *J. Alloys Compd.* **2025**, *1020*, 179490. https://doi.org/10.1016/j.jallcom.2025.179490.
(22) Ciavatti, A.; Capria, E.; Fraleoni-Morgera, A.; Tromba, G.; Dreossi, D.; Sellin, P. J.; Cosseddu, P.; Bonfiglio, A.; Fraboni, B. Toward Low-Voltage and Bendable X-Ray Direct Detectors Based on Organic Semiconducting Single Crystals. *Adv. Mater.* **2015**, *27* (44), 7213–7220. https://doi.org/10.1002/adma.201503090.
(23) Ciavatti, A.; Cramer, T.; Carroli, M.; Basiricò, L.; Fuhrer, R.; De Leeuw, D. M.; Fraboni, B. Dynamics of Direct X-Ray Detection Processes in High-Z Bi2O3 Nanoparticles-Loaded PFO Polymer-Based Diodes. *Appl. Phys. Lett.* **2017**, *111* (18), 183301. https://doi.org/10.1063/1.4986345.
(24) Ciavatti, A.; Basiricò, L.; Fratelli, I.; Lai, S.; Cosseddu, P.; Bonfiglio, A.; Anthony, J. E.; Fraboni, B. Boosting Direct X-Ray Detection in Organic Thin Films by Small Molecules Tailoring. *Adv. Funct. Mater.* **2019**, *29* (21), 1806119. https://doi.org/10.1002/adfm.201806119.
(25) Chua, L.-L.; Zaumseil, J.; Chang, J.-F.; Ou, E. C.-W.; Ho, P. K.-H.; Sirringhaus, H.; Friend, R. H. General Observation of N-Type Field-Effect Behaviour in Organic Semiconductors. *Nature* **2005**, *434* (7030), 194–199. https://doi.org/10.1038/nature03376.
(26) Nicolai, H. T.; Kuik, M.; Wetzelaer, G. A. H.; De Boer, B.; Campbell, C.; Risko, C.; Brédas, J. L.; Blom, P. W. M. Unification of Trap-Limited Electron Transport in Semiconducting Polymers. *Nat. Mater.* **2012**, *11* (10), 882–887. https://doi.org/10.1038/nmat3384.
(27) Abd Nasir, F. H.; Woon, K. L. Charge Carrier Trapping in Organic Semiconductors: Origins, Impact and Strategies for Mitigation. *Synth. Met.* **2024**, *307*, 117661. https://doi.org/10.1016/j.synthmet.2024.117661.
(28) Haneef, H. F.; Zeidell, A. M.; Jurchescu, O. D. Charge Carrier Traps in Organic Semiconductors: A Review on the Underlying Physics and Impact on Electronic Devices. *J. Mater. Chem. C* **2020**, *8* (3), 759–787. https://doi.org/10.1039/C9TC05695E.
(29) Temiño, I.; Basiricò, L.; Fratelli, I.; Tamayo, A.; Ciavatti, A.; Mas-Torrent, M.; Fraboni, B. Morphology and Mobility as Tools to Control and Unprecedentedly Enhance X-Ray Sensitivity in Organic Thin-Films. *Nat. Commun.* **2020**, *11* (1), 2136. https://doi.org/10.1038/s41467-020-15974-7.
(30) Zhu, M.; Lv, S.; Wang, Q.; Zhang, G.; Lu, H.; Qiu, L. Enhanced Near-Infrared Photoresponse of Organic Phototransistors Based on Single-Component Donor–Acceptor Conjugated Polymer Nanowires. *Nanoscale* **2016**, *8* (14), 7738–7748. https://doi.org/10.1039/C5NR09003B.
(31) Mescher, H.; Schackmar, F.; Eggers, H.; Abzieher, T.; Zuber, M.; Hamann, E.; Baumbach, T.; Richards, B. S.; Hernandez-Sosa, G.; Paetzold, U. W.; Lemmer, U. Flexible Inkjet-Printed Triple Cation Perovskite X-Ray Detectors. *ACS Appl. Mater. Interfaces* **2020**, *12* (13), 15774–15784. https://doi.org/10.1021/acsami.9b14649.
(32) Marouf, H.; Abdel-Salam, N.; El-Rabaie, E.-S. M.; Rashed, A. N. Z.; ElKhamisy, K. M. A Comprehensive Review Of Photodetectors: Materials, Enhancement Techniques, Perspectives, and Recent Directions. *J. Opt.* **2025**. https://doi.org/10.1007/s12596-025-02779-4.
(33) Allisy, A.; Jennings, W. A.; Kellerer, A. M.; Müller, J. W.; Rossi, H. H.; Seltzer, S. M. Fundamental Quantities and Units for Ionizing Radiation. *Rep. Int. Comm. Radiat. Units Meas.* **1998**, *os-31* (1), 1–1. https://doi.org/10.1093/jicru_os31.1.1.
(34) Yukihara, E. G.; McKeever, S. W. S. Optically Stimulated Luminescence (OSL) Dosimetry in Medicine. *Phys. Med. Biol.* **2008**, *53* (20), R351–R379. https://doi.org/10.1088/0031-9155/53/20/R01.

(35) Petringa, G.; Guarrera, M.; Kurmanova, A.; Tudisco, S.; Verona, C.; Cirrone, G. A. P. Silicon Carbide Sensors in Radiotherapy Dosimetry: Progress, Challenges, and Perspectives. *Front. Sens.* **2025**, *6*, 1622153. https://doi.org/10.3389/fsens.2025.1622153.
(36) Pettinato, S.; Salvatori, S. Diamond-Based Detection Systems for Tomorrow's Precision Dosimetry. *Nucl. Instrum. Methods Phys. Res. Sect. Accel. Spectrometers Detect. Assoc. Equip.* **2024**, *1059*, 168974. https://doi.org/10.1016/j.nima.2023.168974.
(37) Fratelli, I.; Carturan, S. M.; Tommasino, F.; Basiricò, L.; Pino, F.; Valletta, A.; Campajola, M.; Rapisarda, M.; Calvi, S.; Scagliotti, M.; Ciavatti, A.; Tortora, L.; Verroi, E.; Delgado, J. C.; Margotti, L.; Bordoni, C.; Napolitano, G.; Moretto, S.; Aloisio, A.; Sarnelli, E.; Branchini, P.; Mariucci, L.; Quaranta, A.; Fraboni, B. A Wearable Tool for Real-Time Dose Monitoring during Cancer Radiation Therapies. *Sci. Adv.* **2025**, *11* (17), eadt7633. https://doi.org/10.1126/sciadv.adt7633.
(38) McDowell, C.; Bazan, G. C. Organic Solar Cells Processed from Green Solvents. *Curr. Opin. Green Sustain. Chem.* **2017**, *5*, 49–54. https://doi.org/10.1016/j.cogsc.2017.03.007.
(39) Zhang, S.; Ye, L.; Zhang, H.; Hou, J. Green-Solvent-Processable Organic Solar Cells. *Mater. Today* **2016**, *19* (9), 533–543. https://doi.org/10.1016/j.mattod.2016.02.019.
(40) Cho, J.; Yu, S. H.; Chung, D. S. Environmentally Benign Fabrication Processes for High-Performance Polymeric Semiconductors. *J. Mater. Chem. C* **2017**, *5* (11), 2745–2757. https://doi.org/10.1039/C6TC05535D.
(41) He, Z.; Zhang, Z.; Asare-Yeboah, K.; Bi, S. Binary Solvent Engineering for Small-Molecular Organic Semiconductor Crystallization. *Mater. Adv.* **2023**, *4* (3), 769–786. https://doi.org/10.1039/D2MA00726F.
(42) Ho, D.; Lee, J.; Park, S.; Park, Y.; Cho, K.; Campana, F.; Lanari, D.; Facchetti, A.; Seo, S.; Kim, C.; Marrocchi, A.; Vaccaro, L. Green Solvents for Organic Thin-Film Transistor Processing. *J. Mater. Chem. C* **2020**, *8* (17), 5786–5794. https://doi.org/10.1039/D0TC00512F.
(43) Du, Z.; Luong, H. M.; Sabury, S.; Jones, A. L.; Zhu, Z.; Panoy, P.; Chae, S.; Yi, A.; Kim, H. J.; Xiao, S.; Brus, V. V.; Manjunatha Reddy, G. N.; Reynolds, J. R.; Nguyen, T. High-Performance Wearable Organic Photodetectors by Molecular Design and Green Solvent Processing for Pulse Oximetry and Photoplethysmography. *Adv. Mater.* **2024**, *36* (9), 2310478. https://doi.org/10.1002/adma.202310478.
(44) Huang, J.; Luong, H. M.; Lee, J.; Chae, S.; Yi, A.; Qu, Z.-Z.; Du, Z.; Choi, D. G.; Kim, H. J.; Nguyen, T.-Q. Green-Solvent-Processed High-Performance Broadband Organic Photodetectors. *ACS Appl. Mater. Interfaces* **2023**, *15* (31), 37748–37755. https://doi.org/10.1021/acsami.3c09391.
(45) Pang, S.; Chen, Z.; Li, J.; Chen, Y.; Liu, Z.; Wu, H.; Duan, C.; Huang, F.; Cao, Y. High-Efficiency Organic Solar Cells Processed from a Real Green Solvent. *Mater. Horiz.* **2023**, *10* (2), 473–482. https://doi.org/10.1039/D2MH01314B.
(46) Zhang, H.; Yao, H.; Zhao, W.; Ye, L.; Hou, J. High-Efficiency Polymer Solar Cells Enabled by Environment-Friendly Single-Solvent Processing. *Adv. Energy Mater.* **2016**, *6* (6), 1502177. https://doi.org/10.1002/aenm.201502177.
(47) Casula, G.; Lai, S.; Matino, L.; Santoro, F.; Bonfiglio, A.; Cosseddu, P. Printed, Low-Voltage, All-Organic Transistors and Complementary Circuits on Paper Substrate. *Adv. Electron. Mater.* **2020**, *6* (5), 1901027. https://doi.org/10.1002/aelm.201901027.
(48) Yun, S.; Marrocchi, A.; Vaccaro, L.; Kim, C. Effects of Solution-Shearing Process Parameters on Charge Carrier Mobility in Green Solvent-Processed Organic Field-Effect Transistors. *Synth. Met.* **2022**, *291*, 117209. https://doi.org/10.1016/j.synthmet.2022.117209.
(49) Oehzelt, M.; Koch, N.; Heimel, G. Organic Semiconductor Density of States Controls the Energy Level Alignment at Electrode Interfaces. *Nat. Commun.* **2014**, *5* (1), 4174. https://doi.org/10.1038/ncomms5174.
(50) Ishii, H.; Oji, H.; Ito, E.; Hayashi, N.; Yoshimura, D.; Seki, K. Energy Level Alignment and Band Bending at Model Interfaces of Organic Electroluminescent Devices. *J. Lumin.* **2000**, *87–89*, 61–65. https://doi.org/10.1016/S0022-2313(99)00230-6.
(51) Jeong, J. W.; Huh, J. W.; Lee, J. I.; Chu, H. Y.; Pak, J. J.; Ju, B. K. Interdigitated Electrode Geometry Effects on the Performance of Organic Photoconductors for Optical Sensor Applications. *Thin Solid Films* **2010**, *518* (22), 6343–6347. https://doi.org/10.1016/j.tsf.2010.01.056.

(52) Wen, Y.; Xu, J. Scientific Importance of Water-Processable PEDOT–PSS and Preparation, Challenge and New Application in Sensors of Its Film Electrode: A Review. *J. Polym. Sci. Part Polym. Chem.* **2017**, *55* (7), 1121–1150. https://doi.org/10.1002/pola.28482.
(53) Príncipe, C.; Jorge, S. M.; Matos, M.; Santos, L.; Morgado, J.; Charas, A. 3-Oxetanylmethanol as Additive to PEDOT:PSS for Improved Conductivity and Water-Resistance and Applications in Ink-Jet Printed Electrochemical Transistors. *Org. Electron.* **2024**, *125*, 106987. https://doi.org/10.1016/j.orgel.2023.106987.
(54) Carter, J. L.; Kelly, C. A.; Marshall, J. E.; Hammond, V.; Goodship, V.; Jenkins, M. J. PEDOT:PSS Conductivity Enhancement through Addition of the Surfactant Tween 80. *Polymers* **2022**, *14* (23), 5072. https://doi.org/10.3390/polym14235072.
(55) Alemu Mengistie, D.; Wang, P.-C.; Chu, C.-W. Effect of Molecular Weight of Additives on the Conductivity of PEDOT:PSS and Efficiency for ITO-Free Organic Solar Cells. *J. Mater. Chem. A* **2013**, *1* (34), 9907. https://doi.org/10.1039/c3ta11726j.
(56) Lang, U.; Naujoks, N.; Dual, J. Mechanical Characterization of PEDOT:PSS Thin Films. *Synth. Met.* **2009**, *159* (5–6), 473–479. https://doi.org/10.1016/j.synthmet.2008.11.005.
(57) Wang, Y.; Zhu, C.; Pfattner, R.; Yan, H.; Jin, L.; Chen, S.; Molina-Lopez, F.; Lissel, F.; Liu, J.; Rabiah, N. I.; Chen, Z.; Chung, J. W.; Linder, C.; Toney, M. F.; Murmann, B.; Bao, Z. A Highly Stretchable, Transparent, and Conductive Polymer. *Sci. Adv.* **2017**, *3* (3), e1602076. https://doi.org/10.1126/sciadv.1602076.
(58) Zhang, S.; Cicoira, F. Self-Healing: Water-Enabled Healing of Conducting Polymer Films (Adv. Mater. 40/2017). *Adv. Mater.* **2017**, *29* (40), adma.201770291. https://doi.org/10.1002/adma.201770291.
(59) Hu, L.; Song, J.; Yin, X.; Su, Z.; Li, Z. Research Progress on Polymer Solar Cells Based on PEDOT:PSS Electrodes. *Polymers* **2020**, *12* (1), 145. https://doi.org/10.3390/polym12010145.
(60) Saha, A.; Ohori, D.; Sasaki, T.; Itoh, K.; Oshima, R.; Samukawa, S. Effect of Film Morphology on Electrical Conductivity of PEDOT:PSS. *Nanomaterials* **2023**, *14* (1), 95. https://doi.org/10.3390/nano14010095.
(61) Håkansson, A.; Han, S.; Wang, S.; Lu, J.; Braun, S.; Fahlman, M.; Berggren, M.; Crispin, X.; Fabiano, S. Effect of (3-glycidyloxypropyl)Trimethoxysilane (GOPS) on the Electrical Properties of PEDOT:PSS Films. *J. Polym. Sci. Part B Polym. Phys.* **2017**, *55* (10), 814–820. https://doi.org/10.1002/polb.24331.
(62) Tumová, Š.; Malečková, R.; Kubáč, L.; Akrman, J.; Enev, V.; Kalina, L.; Vojtková, E.; Pešková, M.; Víteček, J.; Vala, M.; Weiter, M. Novel Highly Stable Conductive Polymer Composite PEDOT:DBSA for Bioelectronic Applications. *Polym. J.* **2023**, *55* (9), 983–995. https://doi.org/10.1038/s41428-023-00784-7.
(63) Liu, Y.; Liu, Y. Experimental Research on Uniaxial Tensile Mechanical Properties of Kapton Foils. *J. Polym. Res.* **2022**, *29* (7), 271. https://doi.org/10.1007/s10965-022-03123-1.
(64) Shi, H.; Liu, C.; Jiang, Q.; Xu, J. Effective Approaches to Improve the Electrical Conductivity of PEDOT:PSS: A Review. *Adv. Electron. Mater.* **2015**, *1* (4), 1500017. https://doi.org/10.1002/aelm.201500017.
(65) Michelbach, M.; Demyanenko, A.; Hartweg, S.; Otani, H.; Momose, T.; Stienkemeier, F. Laser-Induced Fluorescence Spectroscopy of TIPS-Pentacene. *Low Temp. Phys.* **2025**, *51* (4), 436–443. https://doi.org/10.1063/10.0036202.
(66) Lim, J. A.; Lee, H. S.; Lee, W. H.; Cho, K. Control of the Morphology and Structural Development of Solution-Processed Functionalized Acenes for High-Performance Organic Transistors. *Adv. Funct. Mater.* **2009**, *19* (10), 1515–1525. https://doi.org/10.1002/adfm.200801135.
(67) Venkatesan, S.; Chen, Q.; Ngo, E. C.; Adhikari, N.; Nelson, K.; Dubey, A.; Sun, J.; Bommisetty, V.; Zhang, C.; Galipeau, D.; Qiao, Q. Polymer Solar Cells Processed Using Anisole as a Relatively Nontoxic Solvent. *Energy Technol.* **2014**, *2* (3), 269–274. https://doi.org/10.1002/ente.201300174.
(68) Cohr, K.-H.; Stokholm, J. Toluene: A Toxicologic Review. *Scand. J. Work. Environ. Health* **1979**, *5* (2), 71–90.
(69) Win-Shwe, T.-T.; Fujimaki, H. Neurotoxicity of Toluene. *Toxicol. Lett.* **2010**, *198* (2), 93–99. https://doi.org/10.1016/j.toxlet.2010.06.022.

(70) Maliakal, A.; Raghavachari, K.; Katz, H.; Chandross, E.; Siegrist, T. Photochemical Stability of Pentacene and a Substituted Pentacene in Solution and in Thin Films. *Chem. Mater.* **2004**, *16* (24), 4980–4986. https://doi.org/10.1021/cm049060k.
(71) Akkerman, H. B.; Li, H.; Bao, Z. TIPS-Pentacene Crystalline Thin Film Growth. *Org. Electron.* **2012**, *13* (10), 2056–2062. https://doi.org/10.1016/j.orgel.2012.06.019.
(72) Rasmidi, R.; D. S., M.; Chee, F. P.; Juhim, F.; Rumaling, M. I.; Salleh, S.; Eswar, K. A.; Salleh, K. A. M.; Ibrahim, S. Structural and Optical Properties of TIPS Pentacene Thin Film Exposed to Gamma Radiation. *Mater. Res.* **2022**, *25*, e20220227. https://doi.org/10.1590/1980-5373-mr-2022-0227.
(73) Naftaly, M.; Das, S.; Gallop, J.; Pan, K.; Alkhalil, F.; Kariyapperuma, D.; Constant, S.; Ramsdale, C.; Hao, L. Sheet Resistance Measurements of Conductive Thin Films: A Comparison of Techniques. *Electronics* **2021**, *10* (8), 960. https://doi.org/10.3390/electronics10080960.
(74) Cipolloni, S.; Mariucci, L.; Valletta, A.; Simeone, D.; De Angelis, F.; Fortunato, G. Aging Effects and Electrical Stability in Pentacene Thin Film Transistors. *Thin Solid Films* **2007**, *515* (19), 7546–7550. https://doi.org/10.1016/j.tsf.2006.11.064.
(75) Bontapalle, S.; Varughese, S. Understanding the Mechanism of Ageing and a Method to Improve the Ageing Resistance of Conducting PEDOT:PSS Films. *Polym. Degrad. Stab.* **2020**, *171*, 109025. https://doi.org/10.1016/j.polymdegradstab.2019.109025.